Cell Reports

Article

The exit of naive pluripotency contains a metabolism-induced checkpoint for telomere homeostasis

Graphical abstract

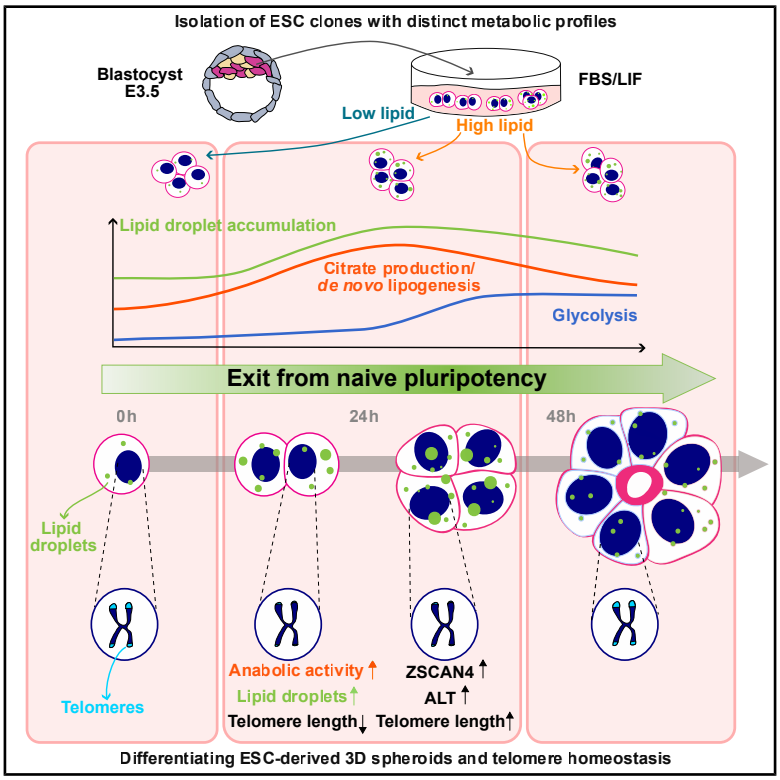

Highlights

- Intrinsic metabolic rewiring in mouse ESCs promotes lipid storage heterogeneity
- The exit of naive pluripotency is marked by a surge in respiration and lipogenesis
- Acute metabolic shifts trigger telomere shortening and ZSCAN4 activation
- ALT pathway supports telomere integrity during pluripotency maturation

Authors

Roshni A. de Souza, David Barneda, Donja Karimlou, ..., Mark Christian, Hendrik Marks, Véronique Azuara

Correspondence

v.azuara@imperial.ac.uk

In brief

de Souza et al. uncover a telomere length checkpoint triggered by metabolic remodeling during the transition from naive to formative pluripotency in mouse ESCs. Acute shifts in mitochondrial respiration and lipid biosynthesis induce transient telomere shortening and ZSCAN4 activation, linking metabolic state to telomere homeostasis in early development.

de Souza et al., 2025, Cell Reports *44*, 116654
December 23, 2025
https://doi.org/10.1016/j.celrep.2025.116654

CellPress

Cell Reports

CellPress
OPEN ACCESS

Article

The exit of naive pluripotency contains a metabolism-induced checkpoint for telomere homeostasis

Roshni A. de Souza,[1] David Barneda,[1,10] Donja Karimlou,[1,10] Nick G.P. Bovee,[2,10] Yuhan Zheng,[1,10] Eveline J.E.M. Kahlman,[2] Clara Lopes Novo,[1] James K. Ellis,[3] Bryony J. Leeke,[4,5] Songyang Li,[1] Megha Prakash Bangalore,[1] Zijing Liu,[6] Bebiana C. Sousa,[7] Andrea F. Lopez-Clavijo,[7] Joop H. Jansen,[8] Mauricio Barahona,[6] Michelle Percharde,[4,5] Hector C. Keun,[3] Mark Christian,[1,9] Hendrik Marks,[2] and Véronique Azuara[1,11,*]

[1]Department of Metabolism, Digestion, and Reproduction, Institute of Reproductive and Developmental Biology, Faculty of Medicine, Imperial College London, London W12 0NN, UK
[2]Department of Molecular Biology, Faculty of Science, Radboud Institute for Molecular Life Sciences (RIMLS), Radboud University Nijmegen, Nijmegen 6525 GA, the Netherlands
[3]Department of Surgery and Cancer, Faculty of Medicine, Imperial College London, London W12 0NN, UK
[4]MRC Laboratory of Medical Sciences (LMS), London W12 0HS, UK
[5]Institute of Clinical Sciences, Faculty of Medicine, Imperial College London, London W12 0NN, UK
[6]Department of Mathematics, Faculty of Natural Sciences, Imperial College London, London SW7 2AZ, UK
[7]Lipidomics Facility, Babraham Institute, Cambridge CB22 3AT, UK
[8]Department of Laboratory Medicine, Laboratory of Hematology, Radboud University Medical Center (Radboudumc), Nijmegen 6525 GA, the Netherlands
[9]School of Science and Technology, Nottingham Trent University, Clifton, Nottingham NG11 8NS, UK
[10]These authors contributed equally
[11]Lead contact
*Correspondence: v.azuara@imperial.ac.uk
https://doi.org/10.1016/j.celrep.2025.116654

SUMMARY

During peri-implantation development, the pluripotent tissue of the early embryo undergoes profound cellular and biochemical reprogramming. These transformations are essential for subsequent development, yet how they are coordinated with the preservation of genome integrity remains poorly understood. Here, we uncover a telomere length checkpoint that is elicited by metabolic remodeling as mouse embryonic stem cells (ESCs) transition from the naive to formative pluripotent state. We show that the exit of naive pluripotency is marked by accelerated mitochondrial respiration and *de novo* lipogenesis, fueling lipid droplet accumulation required for tissue remodeling. Unexpectedly, these acute metabolic shifts trigger transient telomere shortening and activate ZSCAN4, a pluripotency-associated regulator of telomeres, followed by telomere re-elongation as cells adopt a more glycolytic metabolic profile. Our findings reveal a feedback mechanism in which metabolism-induced telomere stress engages ZSCAN4 as a protective response, thereby linking metabolic state to telomere homeostasis during early developmental progression.

INTRODUCTION

Mammalian life begins with the fusion of an oocyte and a sperm to generate a single-cell zygote. As the embryo undergoes successive cleavage divisions, it experiences biochemical changes and cellular transformations, leading to the formation of a competent blastocyst for implantation.[1] Preserving genome integrity during the extensive reprogramming of the early embryo is critical, given its potential to form an adult organism.[2] Pluripotent progenitors, which first emerge within the inner cell mass of the blastocyst, provide a fundamental paradigm for understanding how cell state transitions are executed while safeguarding cellular fitness and developmental potential. At peri-implantation, these progenitors progress along the pluripotency continuum, transitioning from naive through formative to primed states in preparation for differentiation.[3,4] These transitions occur as cells polarize and form an epithelium layer, a structural prerequisite for all subsequent *in vivo* development.[5,6] Naive and primed progenitor states can be recapitulated *in vitro* as self-renewing mouse embryonic stem cells (ESCs) and epiblast stem cells (EpiSCs), respectively.[7–10] These models enabled the dissection of key features that distinguish the two pluripotency states.[9–16] Intermediate states can also be induced transiently in ESCs, adopting a formative epiblast-like cell (EpiLC) phenotype[17] or using three-dimensional (3D) ESC-derived spheroids forming rosette-like epithelial structures.[6,18]

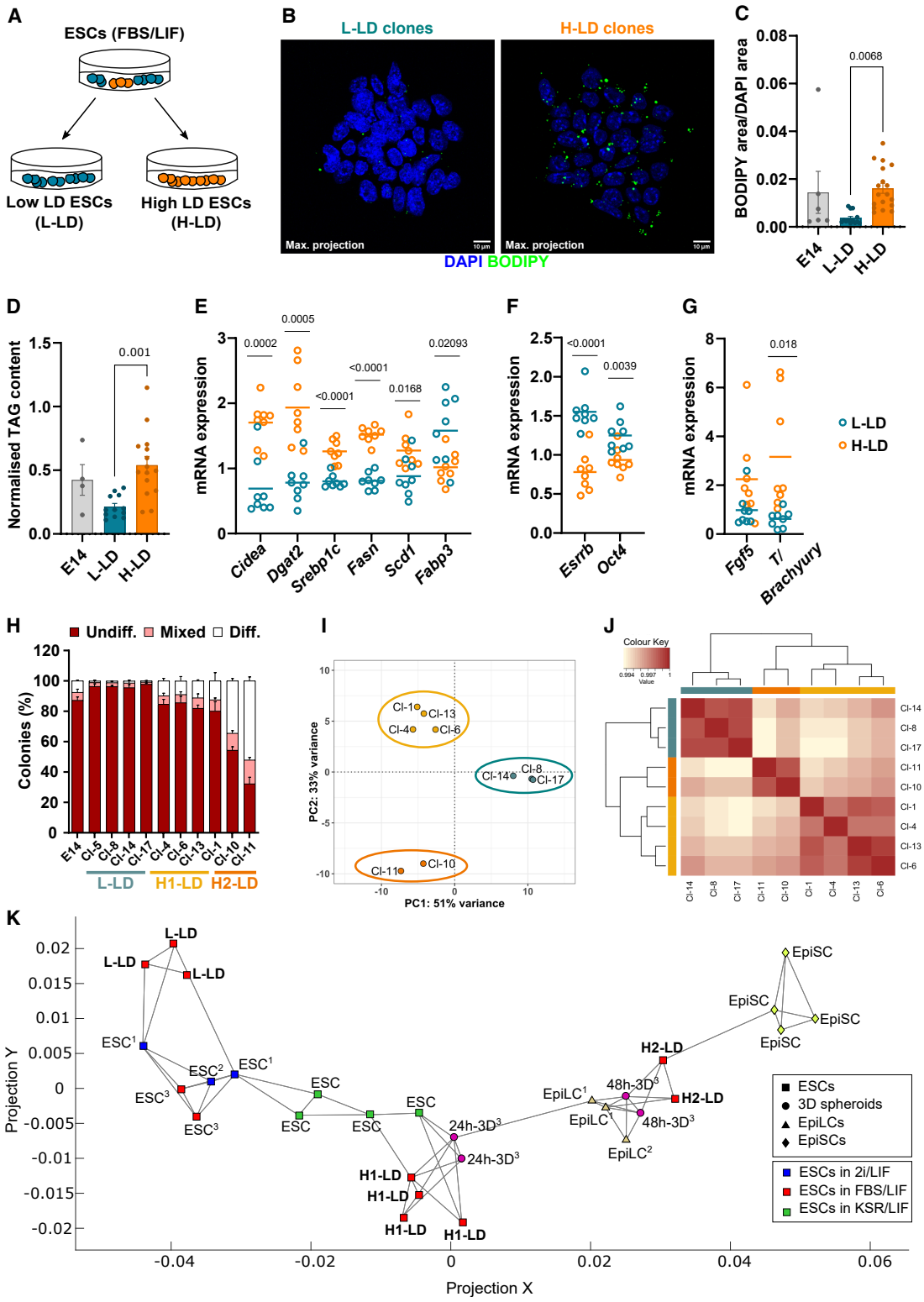

Figure 1. Lipid droplet heterogeneity delineates discrete pluripotency states in ESCs

(A) Isolation of ESC clones with "low" (L-LD) and "high" (H-LD) lipid droplet (LD) content from parental E14-ESCs cultured in FBS/LIF.

(B) Representative images of L-LD and H-LD clone phenotypes with BODIPY 493/503-stained LDs and DAPI-stained nuclei. Images are z stack maximum projections. Scale bars, 10 μm.

(legend continued on next page)

Despite these advances, our understanding of how distinct reprogramming events converge to support developmental progression post-implantation remains limited.

Metabolic remodeling is hardwired into early embryo development.[19–23] Previous studies indicated that the newly formed blastocyst accumulates a substantial amount of lipids stored in enlarged lipid droplets (LDs), which are then mobilized upon implantation.[20,24–28] Remarkably, this dynamic behavior of LDs contributes to the cellular remodeling of pluripotent progenitors, revealing an unexpected connection between lipid storage and morphogenesis.[28] Beyond their core of neutral lipids, LDs are encased in a phospholipid monolayer enriched with proteins that regulate their biology.[29–31] We demonstrated that the LD-associated protein CIDEA is indispensable for efficient lipid storage in ESCs, which, like the blastocyst, possesses the ability to form enlarged LDs. Depleting CIDEA expression leads to a loss of lipid storage and abnormal morphogenesis in both *in vivo* and ESC-derived 3D spheroids.[28] While LD accumulation is recognized as a hallmark of peri-implantation development, the mechanisms driving lipid accumulation and the interplay between metabolic and other regulatory pathways remain largely unexplored.

In this study, we leveraged the inherent heterogeneity of ESCs[12,16,32,33] to isolate clonal populations exhibiting variable levels of lipids stored in the LD. We found that clones with low versus high levels of LD-stored lipids segregate along a differentiation trajectory, consistent with LD accumulation marking the onset of pluripotency maturation.[28] Using these clonal systems, we revealed that the glycolytic shift characteristic of primed EpiSCs[14] is preceded by an acute acceleration of mitochondrial respiration and tricarboxylic acid (TCA) activity, coupled with enhanced fatty acid synthesis. This metabolic reprogramming likely fuels lipid storage and reflects a heightened anabolic capacity in cells exiting naive pluripotency. Unexpectedly, we observed that ZSCAN4, a key pluripotency-associated telomere regulator, is preferentially upregulated in lipid-rich clones, coinciding with reduced global DNA methylation and heterochromatin re-organization as indicators of ZSCAN4 activity.[34–37] Mechanistically, we established that ZSCAN4 induction occurs in cells undergoing transient telomere attrition, downstream of LD-associated metabolic remodeling. Targeted disruption of these metabolic events abolishes both *Zscan4* expression and telomere shortening/re-elongation by the alternative lengthening of telomeres (ALT) pathway, underscoring tight coordination between metabolism and telomere regulation. Our findings uncover a metabolism-induced telomere checkpoint in cells exiting from naive pluripotency and propose a mechanism by which telomere homeostasis is preserved in these key progenitor cells, protecting them from the risks posed by rapid, developmentally regulated metabolic changes.

RESULTS

Lipid storage heterogeneity is a hallmark of ESCs cultured in FBS/LIF

ESCs in fetal bovine serum (FBS)/leukemia inhibitory factor (LIF) co-exist in distinct pluripotency states from naive and self-renewing to more primed for differentiation, as reflected in heterogeneous transcriptional and epigenetic states.[12,16,32] We identified that ESC heterogeneity also manifests at the metabolic level, with a subset of cells exhibiting elevated lipid storage capacity (Figures S1A–S1C). To investigate whether this variation delineates discrete sub-populations, we isolated a panel of clones, which under uniform FBS/LIF conditions showed different content of enlarged LDs (Figure 1A). The co-existence of ESCs with ''low'' (L-LD) and ''high'' (H-LD) LD content was confirmed by quantifying neutral lipids using BODIPY 493/503 staining (Figures 1B and 1C) and liquid chromatography-mass spectrometry (LC-MS) analysis of triglycerides (TAGs) (Figure 1D). While L-LD clones exhibited consistently low levels of BODIPY fluorescence and TAG content, H-LD clones displayed elevated and more heterogeneous values, reflecting the dynamics of LD biology. Indeed, pharmacological inhibition of lipolysis induced a further accumulation of neutral lipids in H-LD cultures, exceeding the levels in similarly treated L-LD clones and controls (Figure S1D).

LD storage capacity in ESCs is enhanced by the LD-associated protein CIDEA, which promotes the fusion of pre-existing LDs, thereby facilitating their enlargement.[28,31] To assess whether CIDEA expression correlates with the observed variability in the LD-stored lipid content, we quantified the *Cidea* transcript across clones. The results revealed pronounced transcriptional heterogeneity, with the highest levels of *Cidea* expression consistently detected in H-LD clones (Figure 1E). Differential gene expression was also observed when analyzing additional lipid-related genes, including *Dgat2* and *Fabp3*, involved in storage and transport, respectively. Notably, these transcriptional differences persisted across serial passages of both L-LD and H-LD clones (Figure S1E), underscoring the stability of their distinct metabolic phenotypes.

Lowered expression of the pluripotency regulators *Esrrb* and *Oct4*/*Pou5f1* was also noted in H-LD clones, alongside

(C) Quantification of BODIPY signal, normalized to DAPI (area), in parental culture (E14) and L-LD (8, 14, and 17), H-LD (4, 6, 10, and 11) clones. For each culture, $n > 5$ colonies were imaged in independent experiments ($n = 3$ per clone).
(D) LC-MS quantification of TAG, normalized to total DNA content, in E14 and clones as above ($n = 4$ per clone).
(E–G) Reverse-transcription quantitative PCR (RT-qPCR) of genes associated with (E) lipid metabolism, (F) pluripotency, and (G) differentiation across all clones isolated (passage 1–2). Each circle represents a single clone, and lines represent mean expression per clone group.
(H) Percentage of newly formed colonies in FBS/LIF scored as undifferentiated, mixed, and differentiated based on alkaline phosphate staining ($n = 3$).
(I and J) PCA (I) and correlation heatmap (J) of RNA-seq data collected from the indicated clones.
(K) Pseudo-differentiation trajectory using dimensionality reduction of transcriptomic data from ESCs (square) in 2i/LIF (blue), FBS/LIF (red), and KSR/LIF (green); differentiating ESC-derived formative EpiLCs (triangles) and 3D spheroids (circles); and embryo-derived primed EpiSCs (diamond). Superscript denotes cell populations analyzed within the same study.
Data (C, D, and H) are represented as mean ± SEM. Statistics for (C) and (D) are ANOVA with Tukey's post hoc test, and for (E)–(G) are two-tailed *t* test with Welch's correction. See also Figure S1 and Tables S1 and S5.

upregulation of early differentiation markers *Fgf5* and *T/Brachyury* (Figures 1F and 1G). Concurring, we found that H-LD clones showed increased spontaneous differentiation, with two sub-groups—H1-LD and H2-LD—forming over 10% and 40% of fully differentiated colonies, respectively (Figure 1H). Moreover, H-LD clones, particularly H2-LD, demonstrated enhanced susceptibility to induced differentiation *in vitro* upon embryoid body formation (Figure S1F). Under ''ground state'' (2i/LIF) culture conditions,[38] however, H-LD clones reverted to an ''L-LD-like'' phenotype, characterized by robust self-renewal capacity and the presence of small LDs, as seen in standard 2i/LIF-cultured ESCs (Figures S1A, S1B, and S1G). Collectively, our findings uncover a high degree of lipid metabolic heterogeneity in FBS/LIF ESCs, potentially reflecting discrete pluripotent statuses.

L-LD and H-LD clones segregate along a differentiation trajectory

RNA sequencing was conducted on representative clones to further define their pluripotency status. Principal-component analysis (PCA) and correlation heatmap analysis revealed three distinct clusters of clones (Figures 1I and 1J). PC-1 separated L-LD and H-LD clones, showing the majority of transcriptomic variance between all samples (PC-1 = 51%). PC-2 further resolved the H-LD clones into two distinct clusters, corresponding to the H1-LD and H2-LD subgroups previously defined by functional differences in their self-renewal capacity (Figure 1H). Moreover, pathways analysis of differentially expressed genes revealed an enrichment of developmental terms in H2-LD compared to both H1-LD and L-LD clones (Figure S1H; Table S1). Conversely, pathways associated with self-renewal and pluripotency maintenance were predominantly enriched in the L-LD clones. Importantly, lipid metabolism and other metabolic processes emerged as key distinguishing features across clones, further suggesting the existence of metabolic heterogeneity within ESC cultures.

To establish whether these clonal populations capture distinct stages of pluripotency maturation, we developed a differentiation trajectory using dimensionality reduction clustering,[39] enabling the projection of our clone transcriptional profiles onto a continuum of pluripotency states (Figure 1K). We leveraged published RNA sequencing datasets generated from ESCs cultured under various conditions, EpiSCs, and *in vitro* ESC-induced differentiation models.[28,40,41] Notably, we included transcriptomic data from differentiating ESC-derived 3D spheroids, a model system we employed to uncover the role of lipid storage in the cellular remodeling of pluripotent progenitors[28] (Figure S1I). We confirmed that L-LD clones closely aligned with the naive/ground-state pluripotency of 2i/LIF-cultured ESCs (Figure 1K). H1-LD clones occupied an early transitional position, coinciding with peak LD accumulation in 3D spheroids at 24 h post-induction (Figures S1I and S1J) and with ESCs cultured in knockout serum replacement (KSR) known to promote LD enlargement[28] and developmental progression[41,42] (Figure 1K). In contrast, H2-LD clones mapped furthest along the trajectory, clustering with the formative state of EpiLC and 48-h spheroid samples; yet, they did not acquire the fully primed transcriptional profile of EpiSCs (Figure 1K), indicating an intermediate identity. These findings demonstrate that L-LD, H1-LD, and H2-LD clones represent discrete pluripotent and metabolic states, recapitulating early transitions from naive pluripotency in the absence of exogenous differentiation cues.

Enhanced mitochondrial oxidation signals the onset of metabolic rewiring in ESCs

To further resolve the metabolic profiles of L-LD and H-LD clones, we assessed key metabolic fluxes under standardized culture conditions, ensuring comparable growth rates across populations (Figure S2A). Using Seahorse assays, we monitored oxygen consumption (OCR) and extracellular acidification (ECAR) rates as indicators of mitochondrial respiration and glycolytic capacity, respectively (Figures 2A and 2B). H-LD clones exhibited elevated OCR values across all respiration-associated parameters (Figures 2A and S2B). Notably, H1-LD clones displayed a pronounced oxidative profile relative to L-LD clones, further supported by increased levels of total reactive oxygen species (ROS) (Figure 2C). Concurrently, H-LD clones exhibited enhanced glycolytic activity, with H2-LD clones showing the most pronounced acceleration (Figures 2B and S2C), underscoring their more developmentally advanced state (Figure 1K and Zhou et al.[14]). This was further supported by a differential dependence on glutamine for mitochondrial respiration exclusively observed in H-LD clones (Figures S2D and S2E), a hallmark of cells transitioning toward pluripotency exit.[43] These results define transitional metabolic phenotypes that emerge between naive-ESCs and primed-EpiSCs, at the earliest stages of exiting pluripotency.

We then performed untargeted gas chromatography-mass spectrometry (GC-MS) metabolomics (Table S2). Consistent with earlier findings, H-LD clones showed dynamic changes in redox status, as evidenced by the activation of antioxidant pathways with lowered detection of reduced methionine and glutathione (Figures S2F and S2G). In support of glycolysis acceleration, we observed an increase in glucose and glycolytic intermediates in H-LD compared to L-LD clones (Figures 2D and 2F). Notably, the concentrations of glycerol-3-phosphate (G3P), a key precursor for TAG synthesis, were elevated in H1-LD and, to a lesser extent, in H2-LD clones (Figure 2D), paralleling the TAG levels previously quantified in these populations (Figures 1D, S2H, and S2I). Given the enrichment of TCA cycle-associated pathways in H-LD clones (Table S1), we further surveyed the representation of TCA intermediates. We identified a selective elevation of citrate levels in H-LD clones, in contrast to α-ketoglutarate, which showed minimal variation (Figures 2E and 2F; Table S2). This suggests a metabolic shift favoring citrate accumulation, indicative of altered TCA cycle engagement in more developmentally advanced populations. Our integrated analyses reveal an acceleration in mitochondrial respiration and increased citrate production in ESCs at the exit of naive pluripotency, prior to transitioning toward a more glycolytic metabolic profile.

LD accumulation reflects higher TCA-fueled lipid synthesis in ESCs

Given the lipid-rich phenotype of H-LD clones, we asked whether the elevated levels of G3P and citrate we observed

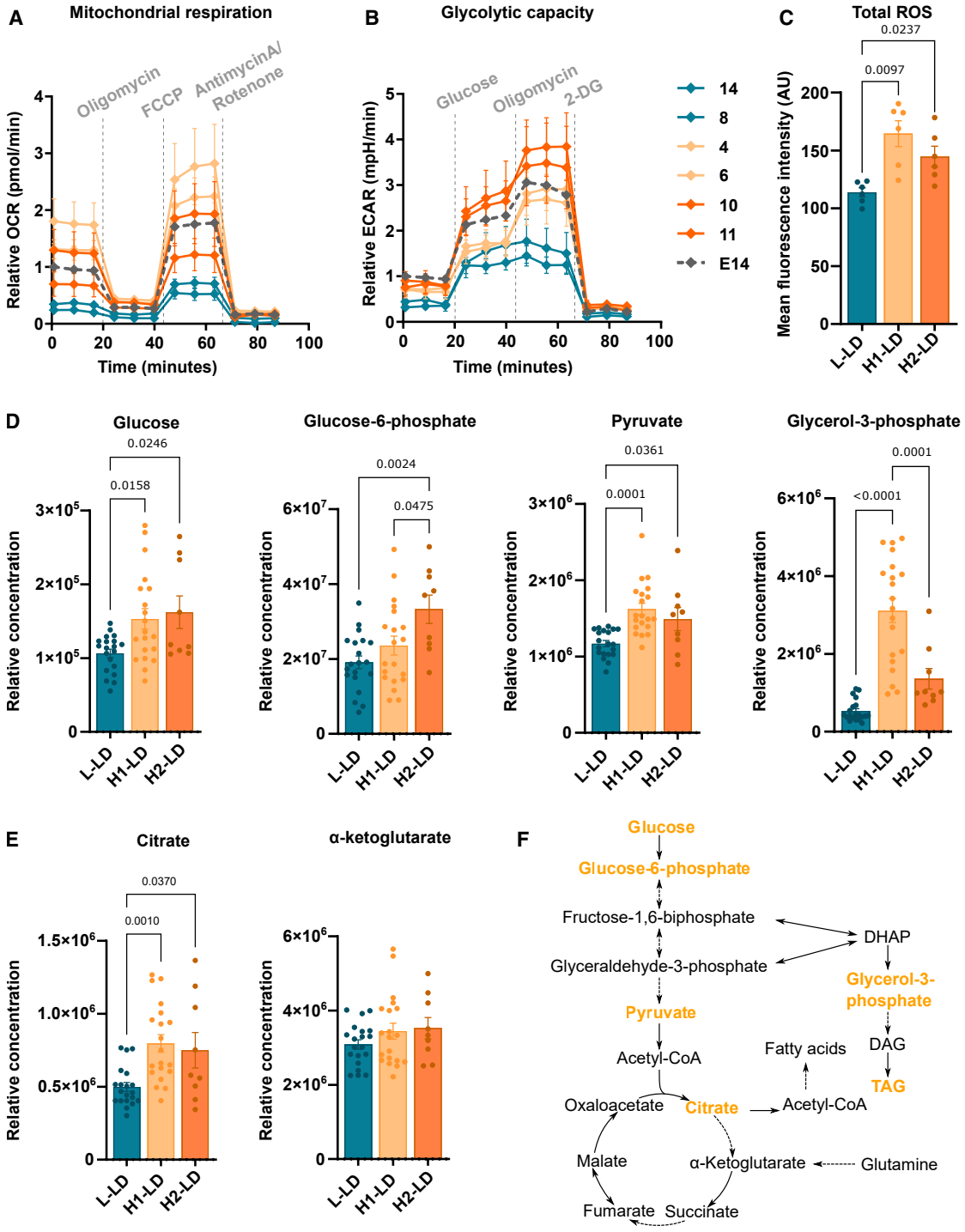

Figure 2. Enhanced oxidation signals the onset of metabolic rewiring in ESCs

(A and B) Seahorse analysis of (A) OCR and (B) ECAR as measures of mitochondrial respiration and glycolytic capacity in indicated clones (n = 3). Data are normalized to parental line (E14; dashed line) (see Figures S2B and S2C).

(C) Total ROS levels, indicated by DCFDA fluorescence, in L-LD (8), H1-LD (4), and H2-LD (11) clones (n = 6).

(D and E) Relative concentration of (D) glycolysis and (E) TCA cycle intermediate metabolites in L-LD (5, 8, 14, and 17), H1-LD (1, 4, 6, and 13), and H2-LD (10 and 11) measured by GC-MS (n = 4 per clone) (see Figures S2H and S2I).

(F) Schematic of metabolic pathways with metabolites enriched in H-LD clones shown in orange.

Data in (A)–(E) are represented as mean ± SEM. Statistics for (C)–(E) are ANOVA with Tukey's post hoc test. See also Figure S2 and Table S2.

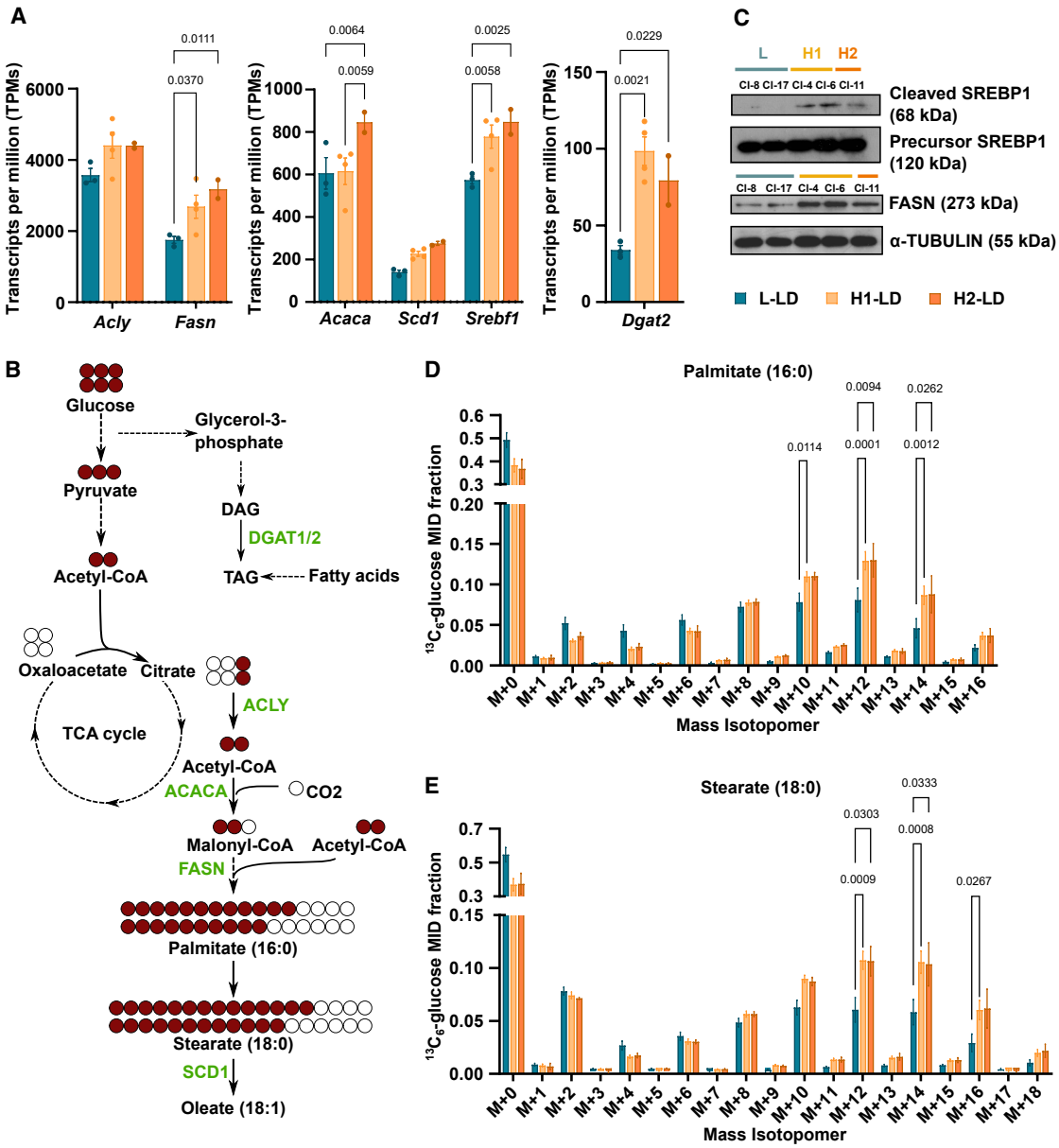

Figure 3. LD accumulation reflects higher TCA-fueled lipid synthesis in ESCs

(A) Expression of genes associated with lipid synthesis and storage, represented as transcripts per million (TPMs), in L-LD (8, 14, and 17), H1-LD (1, 4, 6, and 13), and H2-LD (10 and 11) clones.

(B) Schematic of $^{13}C_6$-glucose-derived carbon (red) incorporation in FA synthesis and elongation with key enzymes indicated.

(C) Representative western blot of cleaved and precursor SREBP1, FASN, and α-TUBULIN used as loading control (see Figures S2J and S2K).

(D and E) $^{13}C_6$-labeled FAs represented as a mass isotopomer distribution (MID) of (D) palmitate and (E) stearate in L-LD (8, 14, and 17), H1-LD (1, 4, 6, and 13), and H2-LD (11) clones (n = 3 per clone).

Data in (A), (D), and (E) are represented as mean ± SEM. Statistics for (A), (D), and (E) are Fisher's two-way ANOVA. See also Figure S2 and Table S3.

were linked to lipid biosynthesis. Leveraging transcriptomic data from clones, we surveyed the expression of key genes involved in *de novo* lipogenesis (Figures 3A and 3B). These included *Acly*, encoding ATP citrate lyase (ACLY) that bridges the TCA cycle with fatty acid (FA) synthesis by catalyzing the conversion of citrate to acetyl-CoA required for lipid synthesis. We further examined the expression of *Acaca* and *Fasn*, which encode the rate-limiting enzymes in FA synthesis. Additionally, we profiled *Scd1*, responsible for generating monounsaturated FAs essential for ESC survival,[44] and *Srebf1*, which encodes the transcription factor SREBP1 that drives the expression of *Acly*, *Fasn*, and *Scd1*. All genes examined were consistently upregulated in H-LD relative to L-LD populations, mirroring the expression pattern of *Dgat2*, a key enzyme in TAG synthesis

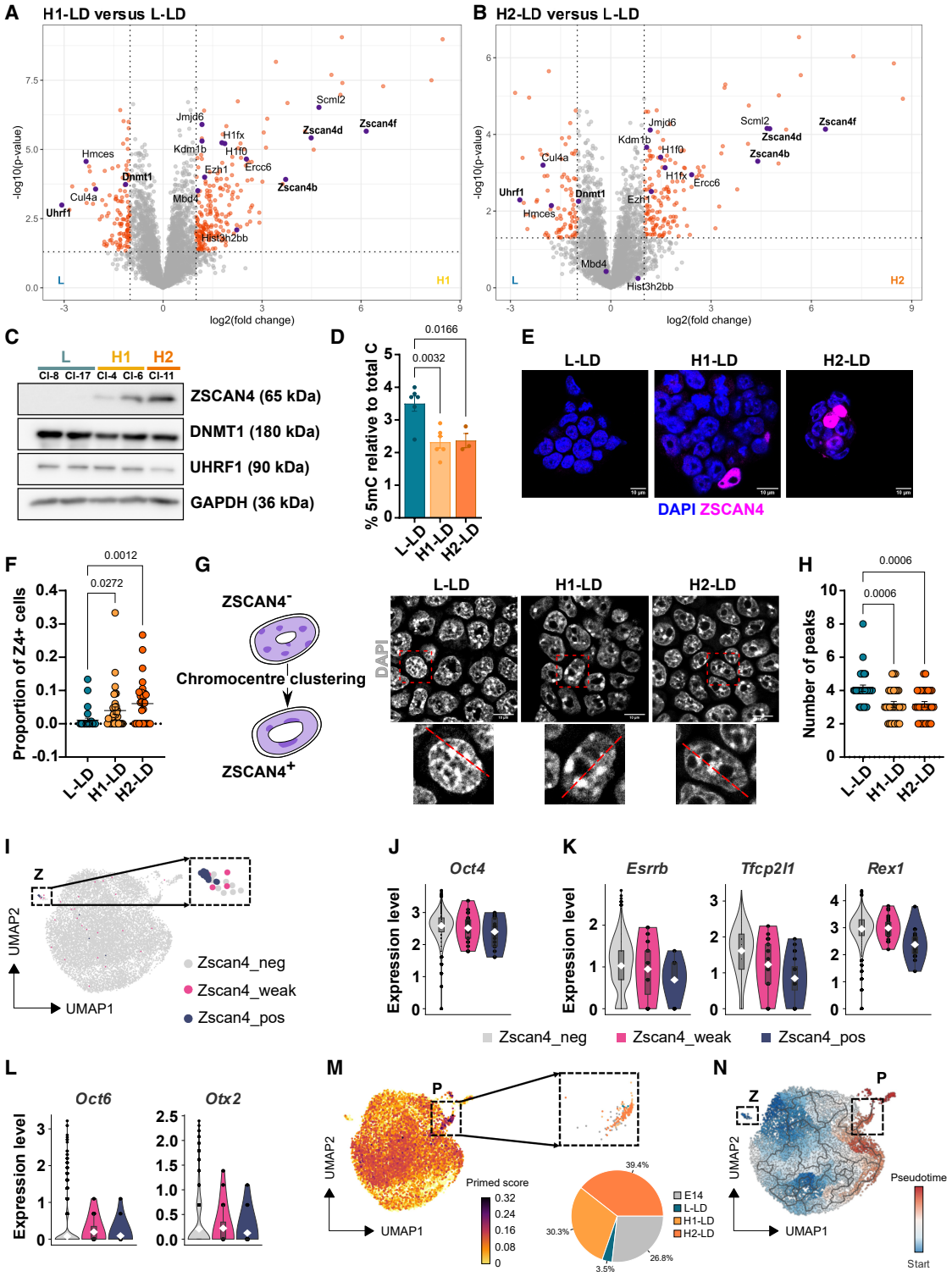

Figure 4. Lipid storage and *Zscan4* induction intersect during cell state transitions

(A and B) Differential enrichment of chromatin-bound proteins in L-LD (8 and 17), H1-LD (4 and 6), and H2-LD (11) clones as determined by ChEP. Data points in red indicate p value < 0.05, log2 fold change ± 1 cutoff.

(C) Representative western blot for ZSCAN4, DNMT1, UHRF1, and GAPDH used as loading control (n = 3).

(D) Percentage of 5-methylcytosine (5mC) to total cytosine (C) in L-LD (8 and 17), H1-LD (4 and 6) and H2-LD (11) clones as quantified by HPLC-MS (n = 3 per clone).

(legend continued on next page)

(Figures 3A and 3B). Higher transcriptional activity of SREBP1 was further validated by western blot, showing increased ratios of cleaved (active) to precursor SREBP1 (Figures 3C and S2J). This, together with increased FASN expression (Figures 3C and S2K), suggests that lipogenesis is enhanced in H-LD clones.

FA synthesis can be tracked using $^{13}C_6$-glucose, which generates acetyl-CoA (from cytosolic citrate) containing two labeled carbons that are incorporated into newly synthesized palmitate (16:0) and elongated stearate (18:0) (Figure 3B). GC-MS analysis of total FAs revealed no differences in the concentrations of palmitate or desaturated oleate (18:1) among clonal populations (Figure S2L; Table S3). Interestingly, stearate, a metabolic indicator of pluripotency states,[45] was selectively elevated in H1-LD clones, underscoring their transitional identity. To directly assess lipogenesis, we quantified the incorporation of labeled $^{13}C_6$ into palmitate and stearate (Figures 3D and 3E; Table S3). The results demonstrate elevated rates of *de novo* FA synthesis in both H1-LD and H2-LD clones, as evidenced by a reduced fraction of unlabeled species (M+0). Concomitantly, H-LD clones showed increased incorporation of labeled $^{13}C_6$ into palmitate (M+10, M+12, and M+14) and stearate (M+12, M+14, and M+16), suggesting enhanced utilization of glucose-derived acetyl-CoA for FA synthesis and elongation. Collectively, these findings reveal a metabolic redirection at the exit of naive pluripotency, characterized by increased engagement of glucose-derived TCA activity toward citrate production and *de novo* lipid synthesis. This shift likely fuels the accumulation of LDs required for cellular remodeling during peri-implantation development.[28]

ChEP-based profiling of chromatin-bound proteomes in LD clones

Remarkably, L-LD and H-LD clones maintain stable metabolic and transcriptional phenotypes upon propagation (Figure S1E), suggesting distinct epigenomic configurations. To investigate this, we profiled the chromatin-bound proteomes of representative clones using chromatin enrichment for proteomics (ChEP).[46] We confirmed that L-LD and H-LD clones could be segregated based on the data using PCA (Figure S3A). Among the differentially bound chromatin regulators, we identified a notable enrichment of DNA methylation-associated proteins, including DNMT1 and UHRF1, in L-LD relative to both H1-LD and H2-LD clones (Figures 4A and 4B; Table S4). Strikingly, this pattern was reflected in H-LD clones by an enrichment of ZSCAN4, known to promote the degradation of DNMT1 and UHRF1 in ESCs.[37] Western blot confirmed that H-LD clones express higher ZSCAN4 with reduced DNMT1 and UHRF1, compared to L-LD clones (Figure 4C). This corroborates with a reduction in global DNA methylation in H-LD clones, as quantified by high-performance liquid chromatography (HPLC)-MS (Figure 4D).

Originally identified as a marker of the 2-cell (2C) stage in mouse embryos,[34] ZSCAN4 is also sporadically expressed in ESCs.[35,36,47–50] Correspondingly, immunofluorescence analysis revealed nuclear ZSCAN4 in only a fraction of cells across clonal populations (Figure 4E). However, the frequency of these "ZSCAN4 events" was elevated in H-LD clones, most significantly in H2-LD, relative to L-LD clones (Figure 4F). This trend was also reflected at the transcriptional level with the upregulation of *Zscan4* paralogs in H-LD clones, alongside *Dppa3*, a gene implicated in DNA demethylation in ZSCAN4-expressing ESCs[51] (Figures S3B and S3C). ZSCAN4 activity is also associated with dynamic heterochromatin re-organization.[36,37] Therefore, we examined the number and spatial distribution of chromocenters in L-LD and H-LD clones using DAPI linescan analysis.[52,53] Indicative of chromatin decompaction,[36] we observed a reduction in chromocenter number in H-LD clones, which formed larger foci around nucleoli (Figures 4G and 4H). Collectively, these analyses reveal a higher incidence of ZSCAN4 events in H-LD clones, transiently promoting DNA demethylation and chromatin accessibility.[36,37] Such global chromatin changes may partially account for the stable propagation of clone phenotypes.

Lipid storage and *Zscan4* induction intersect at the onset of ESC differentiation

Unexpectedly, our results suggest that ZSCAN4 is expressed more frequently in ESCs undergoing metabolic and cell state transitions at the exit of naive pluripotency. To further characterize the phenotype of transiently expressed *Zscan4*-positive cells within our clonal systems, we performed single-cell transcriptomics. To verify that the data captured the defining characteristics of L-LD, H1-LD, and H2-LD clones, we computed gene expression signature scores corresponding to "naive" and "formative/primed" pluripotency and "lipid" metabolism. We confirmed that H1-LD and H2-LD populations exhibit elevated "lipid" scores that correlate with more developmentally advanced pluripotency signatures at single-cell resolution (Figures S3D–S3G).

As anticipated,[54] *Zscan4* transcripts were detected in only a small subset of cells across all populations (n = 4–27). However, total *Zscan4* counts varied among clones, with consistently lower detection in L-LD cells (Figure S3H). UMAP analysis of merged datasets identified a distinct cell cluster (Z) comprising *Zscan4*-positive, -negative, and -weakly expressing cells (Figure 4I). *Zscan4*-positive cells were enriched for known *Zscan4* activators and genes upregulated in ZSCAN4-expressing ESCs[49,51,55–57]

(E and F) Representative images of ZSCAN4 and DAPI staining (E) and proportion of ZSCAN4-positive (Z4+) to the total number of cells per colony (F) in L-LD (8), H1-LD (4), and H2-LD (11) clones. Each dot represents one colony (n > 30 colonies across 3 independent experiments). Scale bars, 10 μm.
(G) Schematic of chromocenter distribution in ZSCAN4− and ZSCAN4+ ESCs (left) and DAPI linescan analysis, as indicated in insets (right). Scale bars, 10 μm.
(H) Quantification of the number of chromocenters as shown in (G). Each dot represents one nucleus (n = 30 nuclei across 3 independent experiments).
(I) UMAP from scRNA-seq data showing *Zscan4*-negative, -weakly expressing, and -positive ESCs across L-LD (8 and 17), H1-LD (4 and 6), and H2-LD (11) clones and parental (E14) culture, highlighting "cluster Z" with a high proportion *Zscan4*-expressing cells.
(J–L) Expression levels of (J) core (*Oct4*/*Pou5f1*), (K) naive (*Esrrb*, *Tfc2pl1*, and *Zfp42*/*Rex1*), and (L) formative/primed (*Oct6*/*Pou3f1* and *Otx2*) pluripotency genes in *Zscan4*-negative, -weakly expressing, and -positive single cells.
(M) Formative/primed score mapped across UMAP plot with proportion of parental E14, L-LD, H1-LD, and H2-LD cells within "cluster P."
(N) Pseudo-time trajectory analysis initiated in "cluster Z."
Data in (D), (F), and (H) are represented as mean ± SEM. Statistics for (D), (F), and (H) are ANOVA with Tukey's post hoc test. See also Figure S3 and Table S4.

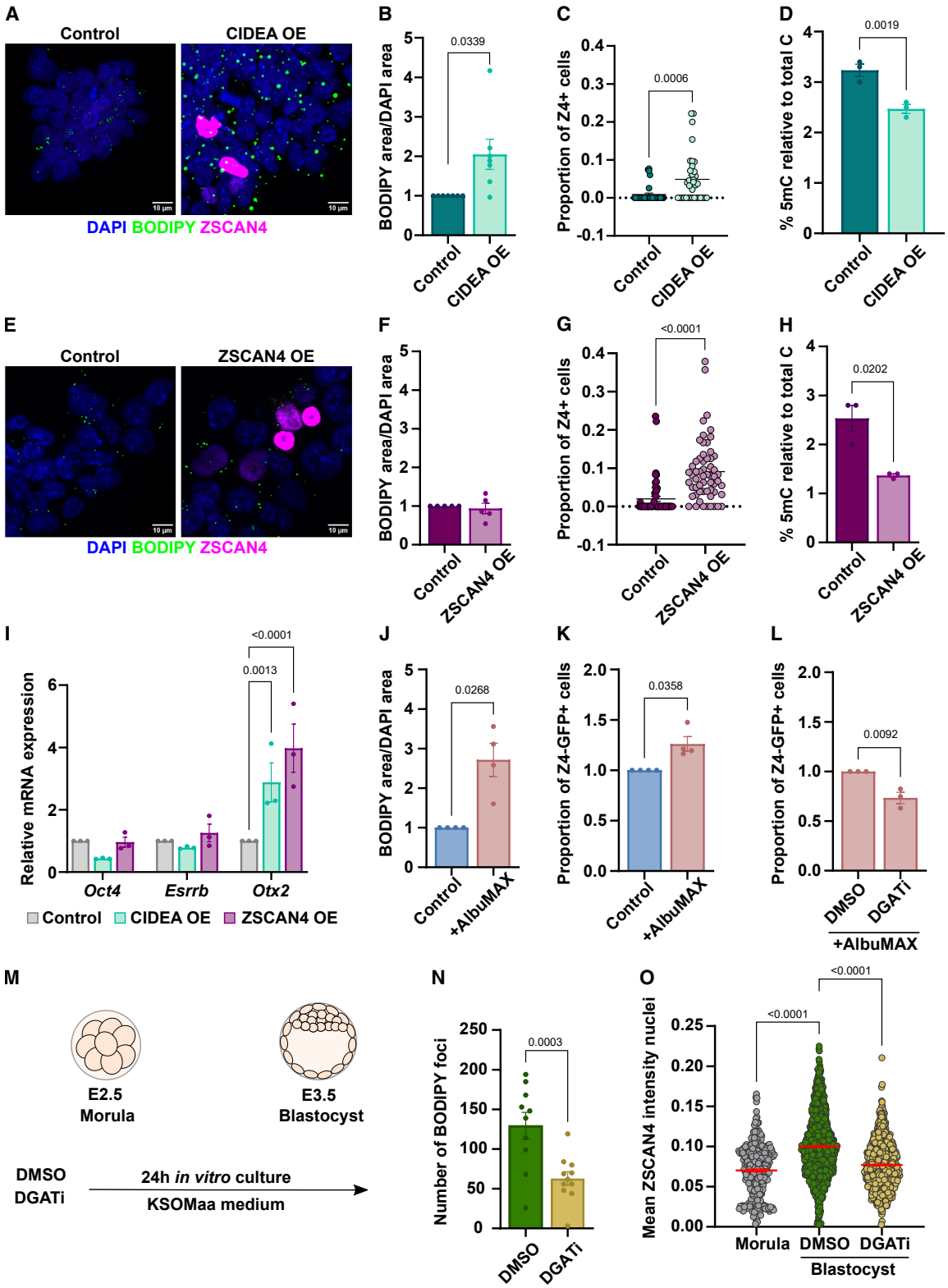

Figure 5. ZSCAN4 induction is driven by anabolic activity in ESCs and during the morula-to-blastocyst transition

(A) Representative images of ZSCAN4, BODIPY, and DAPI staining in empty vector (control) and *Cidea* overexpressing (CIDEA OE) E14-ESCs in FBS/LIF. Scale bars, 10 μm.

(legend continued on next page)

(Figure S3I), supporting a functional link. Conversely, *Zscan4*-weak and *Zscan4*-negative cells showed elevated expression of repressors *Chaf1a*[58] and *Rif1*,[59] underscoring the tightly regulated nature of *Zscan4* expression. Notably, *Zscan4*-positive cells within H-LD populations showed the highest "lipid" scores (Figure S3J) and were more frequently detected (Figure S3H), reinforcing the association between ZSCAN4 events and enhanced lipogenic activity.

Analysis of pluripotency status revealed that, unlike previously characterized 2C-like ESCs,[35,60,61] *Zscan4*-positive cells retained robust *Oct4* transcript expression (Figures 4J and S4N–S4P). Compared to *Zscan4*-weak and -negative cells, these cells expressed lowered levels of naive pluripotency transcripts (Figure 4K), alongside sporadic detection of formative markers (Figure 4L). This likely reflects an early transitional signature,[62,63] consistent with *Zscan4*-positive cells (cluster Z) occupying a trajectory toward primed pluripotency (cluster P), as supported by pseudo-time analysis (Figures 4I, 4M, and 4N). Collectively, these findings support the notion that ZSCAN4 events and lipid-rich cellular states are linked at the single-cell level and underscore that *Zscan4* induction, while enhanced during pluripotency transitions, is a transient and tightly regulated event.

ZSCAN4 induction is driven by metabolic remodeling and anabolic activity in ESCs

Experimental validation confirmed that individual ZSCAN4-positive ESCs contained a significantly higher number of LDs compared to ZSCAN4-negative counterparts in FBS/LIF (Figures S4A and S1A–S1C). To investigate whether the ZSCAN4 phenotype is driven by the lipid-rich state of ESCs, we used a *Cidea* overexpressing (CIDEA OE) model (Figure S4B),[28] whereby lipid storage can be enforced within ESC cultures (Figures 5A and 5B). Besides the accumulation of enlarged LDs, CIDEA OE ESCs recapitulate the key metabolic features of H1-LD clones, including elevated OCR (Figures S4C and S4D) and increased expression of phosphorylated (active) ACLY and FASN (Figure S4E). Crucially, these LD-associated metabolic changes were sufficient to increase the frequency of transient ZSCAN4 events, as evidenced by a higher proportion of ZSCAN4-positive cells and reduced global DNA methylation in CIDEA OE cultures (Figures 5C, 5D, and S4F). In contrast, ectopically expressing *Zscan4c* neither promoted mitochondrial respiration nor enforced a lipid-rich state in ESCs. While *Zscan4c* overexpression (ZSCAN4 OE) significantly reduced the expression and activity of DNMT1 and UHRF1 in ESCs, it had no impact on the number and morphology of LDs or metabolic fluxes running in these cells (Figures 5E–5H and S4G–S4J). These findings indicate that increased ZSCAN4 events are likely the consequence rather than the cause of metabolic rewiring. Enhanced *Zscan4* expression, however, was consistently associated with the upregulation of formative marker *Otx2* in both CIDEA and ZSCAN4 OE models (Figure 5I).

To further delineate the role of metabolic and cell state transitions in regulating ZSCAN4 events, we engineered *Zscan4c* promoter-driven EGFP fluorescent reporter ESCs.[35,48,64] In FBS/LIF, ~0.5%–3% of ESCs were Zscan4c::EGFP-positive (Z4-GFP+). This proportion dropped to ~0.1%–1% in 2i/LIF, where LD accumulation is also reduced (Figures S4K and S1B), consistent with previous observations.[61] However, when 2i/LIF ESCs were transiently induced to adopt a formative EpiLC phenotype,[17] Z4-GFP+ expression peaked at ~5%–6% within 24 h, and this event coincided with a lipid biosynthesis switch (Figures S4L and S4M). These findings align with the lipid-rich phenotype of H-LD clones and formally demonstrate that *Zscan4* activation occurs in ESCs transitioning out of naive pluripotency.

Supplementing cultures with KSR or its lipid-rich component AlbuMAX to promote lipid storage[28] led to a marked increase in OCT4-expressing Z4-GFP+ ESCs (Figures S4N–S4P, 5J, and 5K). This lipid-driven induction was abolished by pharmacological inhibition of DGAT1/2 (DGATi; Figure 5L), underscoring the importance of lipid biosynthesis in regulating ZSCAN4 activation. Given that both clonal and CIDEA OE models exhibit a lipid-rich phenotype driven by enhanced mitochondrial respiration and TCA-linked FA synthesis, we investigated whether these metabolic modulations alone could induce Z4-GFP+ expression in ESCs. Crucially, this was assessed without triggering the exit from naive pluripotency, as monitored in parallel using the Rex1/Zfp42-GFP reporter.[33] We treated both reporter lines with 2-deoxy-D-glucose (2-DG) and dichloroacetate, which promote mitochondrial respiration by inhibiting ATP production via glycolysis.[65,66] Additionally, we supplemented cultures with exogenous TCA intermediates, α-ketoglutarate (α-KG) and citrate, known to fuel TCA activity and lipogenesis, respectively.[67,68] All

(B) Quantification of BODIPY signal in control and CIDEA OE cultures (n = 7).
(C) Proportion of ZSCAN4-positive (Z4+) cells (n > 30 colonies across 3 independent experiments).
(D) Percentage of 5mC to total C (n = 3).
(E) Representative images of ZSCAN4, BODIPY, and DAPI in control and *Zscan4* overexpressing (ZSCAN4 OE) E14-ESCs in FBS/LIF. Scale bars, 10 μm.
(F) Quantification of BODIPY signal in control and ZSCAN4 OE cultures (n = 5).
(G) Proportion of Z4+ cells (n > 30 colonies across 3 independent experiments).
(H) Percentage of 5mC to total C (n = 3).
(I) RT-qPCR of pluripotency genes in CIDEA OE and ZSCAN4 OE ESCs, shown relative to control ESCs (n = 3).
(J) Quantification of BODIPY signal in FBS/LIF-cultured ESCs in the presence or absence of 1% AlbuMAX for 48 h (n = 4).
(K and L) Proportion of ZSCAN4::GFP-positive (Z4-GFP+) E14-ESCs in (K) control and AlbuMAX conditions (n = 3) and (L) AlbuMAX with DMSO or DGAT1/2i (25 μM each) for 48 h (n = 4).
(M) Schematic of mouse embryo *in vitro* culture experiments.
(N and O) Quantification of BODIPY-stained foci (N) and mean ZSCAN4 intensity per nuclei (O) in morula, control (DMSO), and DGATi-treated cultured blastocysts (n = 10–11 embryos).
Data in (B), (D), (F), (H)–(L), (N), and (O) are represented as mean ± SEM. Statistics are paired (B, D, F, H, and J–L) or unpaired (C, G, and N) two-tailed t tests with Welch's correction for (I) a Fisher's two-way ANOVA and for (O) ANOVA with Dunnett's post hoc test, relative to control. See also Figure S5.

four treatments increased the proportion of Z4-GFP+ cells under FBS/LIF conditions, without inducing differentiation, as noted by stable Rex1-GFP+ levels (Figures S4Q and S4R). These findings demonstrate that ZSCAN4 induction is a downstream consequence of acute metabolic reprogramming and heightened anabolic activity, processes that typically unfold as ESCs transition out of the naive pluripotent state.

Lipid biosynthetic activities correlate with sporadic *Zscan4* induction during the morula-to-blastocyst transition

In vivo, LDs undergo active enlargement during the morula-to-blastocyst transition.[25–28] This prompted us to investigate whether LD build-up during this developmental window also influences the expression dynamics of ZSCAN4. By mining the available single-cell RNA sequencing (scRNA-seq) datasets collected from embryos spanning pre-implantation development,[69] we confirmed that gene transcripts associated with lipid biosynthesis were upregulated during the morula-to-blastocyst transition (Figure S5A), consistent with lipid accumulation. As expected, *Zscan4* transcript levels peaked in the late 2C embryo (Figure S5B), as further validated at the protein level (Figure S5C). Notably, we also identified a distinct subpopulation of blastocyst-stage cells (~5%) co-expressing *Zscan4* along with its upstream regulators *Dux* and *Gm4981/Duxf4*[56] (Figure S5B).

To establish a functional link between the anabolic state of the developing blastocyst and *Zscan4* induction, we harvested morula-stage embryos (E2.5) and cultured them to the early blastocyst stage (E3.5) with DMSO or DAGT1/2 inhibitors (DGATi; Figure 5M). DGATi treatment led to a dose-dependent reduction in BODIPY signals, indicating suppressed lipid accumulation. However, the highest inhibitor concentration (50 μM) increased the incidence of arrested or morphologically abnormal embryos (Figures 5N and S5D–S5F) and was therefore excluded from subsequent analyses. Flushed morula and cultured blastocysts were stained for ZSCAN4, F-ACTIN, and DAPI (Figures S5G and S5H). This revealed a significant increase in ZSCAN4 fluorescence intensity per nucleus from the morula to the blastocyst stage, a pattern abrogated upon DGATi treatment (Figure 5O). Taken together, our data reveal that the emergence of a lipid-rich state coincides with ZSCAN4 induction in the developing blastocyst prior to implantation.

The exit from naive pluripotency is accompanied by a metabolism-induced telomere checkpoint

Given the established roles of ZSCAN4 in safeguarding fragile genomic regions[70–72] and maintaining telomere homeostasis,[35,36,47–50] we investigated whether the heightened anabolic activity of lipid-rich ESCs could elevate DNA damage, triggering ZSCAN4 induction. To test this, we quantified global γH2AX levels and assessed apoptosis in CIDEA OE ESCs. These cells showed no increase in double-strand breaks or cell death compared to controls (Figures S6A and S6B). Interestingly, however, CIDEA OE ESCs exhibited shortened telomeres, as revealed by quantitative telomere fluorescence in situ hybridization (Telo-FISH) (Figures 6A and 6B). This telomere shortening occurred independently of telomeric DNA damage (Figure S6C) and was further validated by qPCR-based measurements[73] (Figures 6C, S6D, and S6E). Telomere length analysis was extended to our clonal populations and parental E14-ESCs under metabolic treatments known to induce *Zscan4* (Figures S4Q and S4R). The data offered additional evidence that telomere attrition is metabolically regulated, as observed in KSR/2-DG-treated ESCs (Figures S6F and S6G) and H1-LD clones (Figure 6D). Moreover, in H2-LD clones, telomere length appeared to be further modulated as cells transitioned toward a formative state (Figure 6D). This suggests that a telomere maintenance mechanism is engaged as cells undergo metabolic remodeling at the exit from naive pluripotency.

To confirm that telomere length is safeguarded in a developmentally regulated manner, we measured telomere lengths upon 3D spheroid differentiation. At 24 h, coinciding with peak LD accumulation (Figure S1I), we identified a transient telomere shortening in spheroids formed by wild-type R1-ESCs (Figure 6E). This was accompanied by ZSCAN4 induction (Figures 6G and S6H), consistent with its established role as a sensor of telomere attrition.[47,50,74] Telomere lengths were subsequently restored by 48 h, mirroring the dynamic pattern previously observed in H1-LD and H2-LD clones (Figures 6D and 1K). Remarkably, 3D spheroids formed by *Cidea* knockout (CIDEA KO) ESCs, which fail to sustain lipid storage,[28] showed no significant change in telomere length during differentiation (Figure 6F). This was corroborated by a lack of *Zscan4* upregulation (Figure 6G), reinforcing the link between transient LD accumulation, telomere shortening, and ZSCAN4 induction. In contrast, enforced lipid storage (CIDEA OE) led to further telomere shortening during differentiation (Figure 6H), supporting the model of metabolism-induced telomere attrition. Notably, ESCs overexpressing *Zscan4* (ZSCAN4 OE) prior to spheroid induction were protected against telomere shortening, despite normal LD dynamics (Figures 6H and S6I). Altogether, our findings reinforce a mechanistic connection between lipid metabolism, *Zscan4* induction, and telomere homeostasis during the exit from naive pluripotency.

ZSCAN4 expression has been linked to telomere elongation via the ALT pathway,[37,50,61] which extends telomeres through homologous recombination.[75,76] To investigate whether ALT is activated during 3D spheroid differentiation, we monitored telomere clustering, a hallmark of ALT-associated recombination. We observed a significant increase in both the number and area of telomere foci, peaking in 24 h post-induction (Figures S6J and S6K). ALT activation was further validated in H-LD clones and 3D spheroids using two orthogonal assays: (1) the C-circle amplification (CCA) assay, a qPCR-based method for detecting extrachromosomal C-circles[77] (Figures 6I and 6J), and (2) immunofluorescence detection of ALT-associated PML bodies at telomeres[78] (Figures S6L–S6N). These analyses consistently demonstrated ALT-mediated telomere restoration in differentiating spheroids, except in CIDEA KO spheroids, where lipid accumulation and consequently telomere shortening and *Zscan4* induction were abrogated. Altogether, our findings reveal that telomere length is actively regulated in pluripotent progenitors as they exit from naive pluripotency and that the activation of a ZSCAN4-associated telomere safeguarding mechanism can mitigate the impact of metabolic remodeling during peri-implantation development.

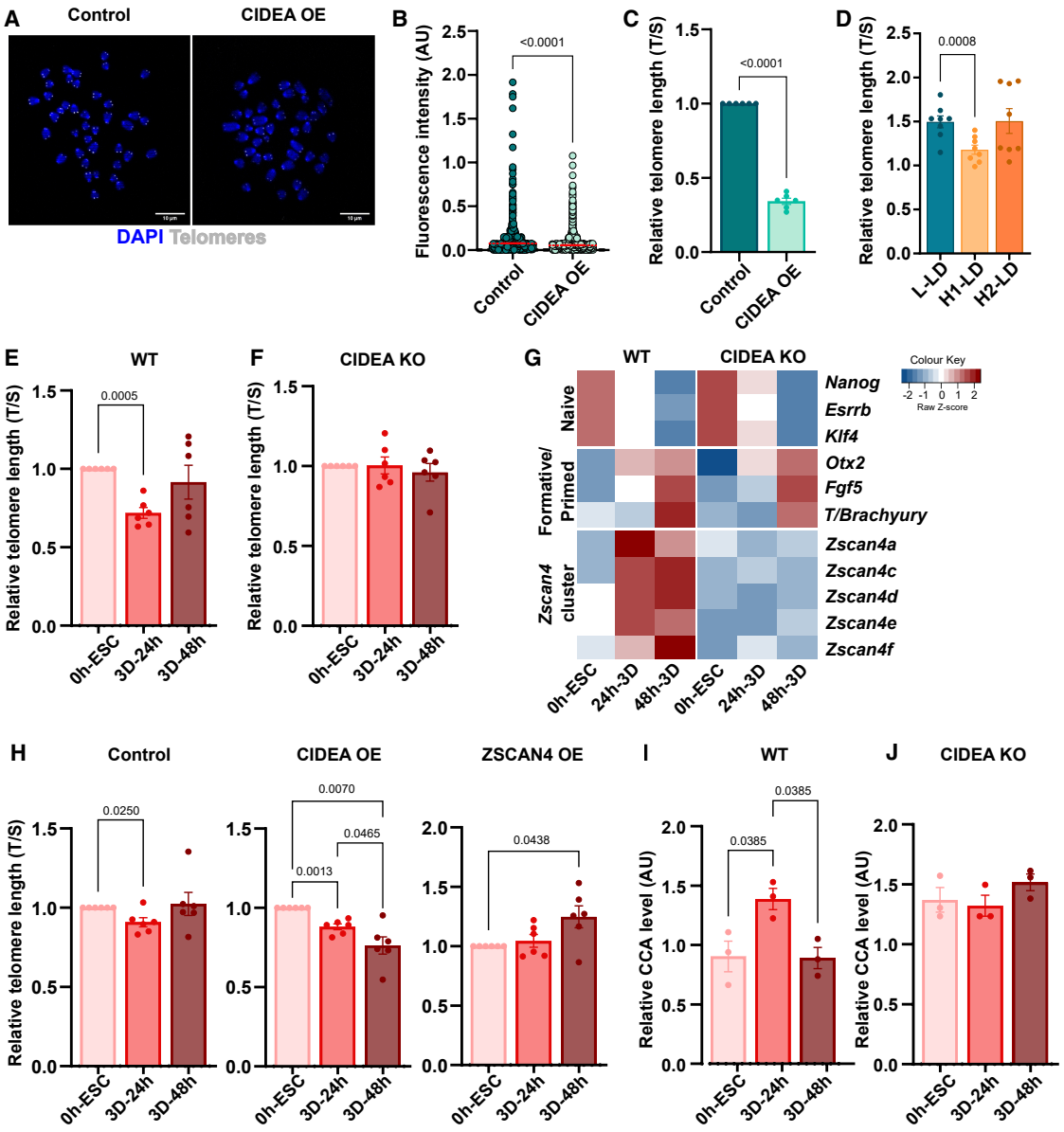

Figure 6. A metabolism-induced telomere checkpoint operates during the exit from naive pluripotency

(A) Representative images of Telo-FISH using TelC-Cy3 probe and DAPI on metaphase spreads prepared from control and CIDEA OE ESCs. Scale bars, 10 μm.

(B) Quantification of fluorescence intensity of TelC-Cy3 signal relative to DAPI signal for each telomeric foci; each dot represents one telomeric foci ($n > 100$ across 3 independent experiments).

(C and D) Relative telomere length as measured by telomere quantitative PCR (qPCR), shown as a ratio of telomere to single-copy gene (T/S) in (C) control and CIDEA OE ESCs ($n = 6$) and (D) representative L-LD (8), H1-LD (4), and H2-LD (11) clones ($n = 8$).

(E and F) Relative telomere length in ESCs (0 h) and differentiating 3D spheroids (24 and 48 h) formed by (E) wild-type (WT) and (F) *Cidea* knockout (CIDEA KO) R1-ESCs ($n = 6$).

(G) Heatmap showing relative transcript expression (bulk RNA-seq) of pluripotency genes and *Zscan4* paralogs upon 3D spheroid formation by WT and CIDEA KO ESCs.

(H) Relative telomere length as measured by telomere qPCR upon 3D spheroid formation by control, CIDEA OE, and ZSCAN4 OE ESCs ($n = 6$).

(I and J) Relative CCA levels as measured by ALT-specific qPCR upon 3D spheroid formation by (I) WT and (J) CIDEA KO ESCs ($n = 3$).

Data are represented as mean ± SEM (B–F and H–J). Statistics are unpaired (B) or paired (C) two-tailed *t* tests with Welch's correction and, for (D)–(F) and (H)–(J), are ANOVA with Tukey's post hoc test. See also Figure S6 and Table S5.

DISCUSSION

Transitions through the pluripotency continuum involve extensive cellular and biochemical remodeling.[6,14,16,28,41] In this study, we identify previously uncharacterized metabolic states that mark early steps during the exit of naive pluripotency. We show that as ESCs exit the naive state, they undergo accelerated mitochondrial respiration and increased citrate production, fueling FA synthesis and lipid storage. Notably, this lipid-synthesizing capacity emerges in a subset of cells within cultures maintained under uniform conditions, pointing to intrinsic metabolic reprogramming. Our findings are further supported by independent evidence that ACLY inactivation blocks the exit from naive pluripotency.[79] Lipid remodeling has also been identified as a prerequisite for adult progenitor function in neurogenesis and myogenesis,[80,81] underscoring the fundamental role of lipid metabolism in both embryonic and postnatal development.

Unexpectedly, our findings reveal that changes in lipid metabolism during pluripotency maturation are tightly coupled to ZSCAN4 activity and telomere homeostasis. ZSCAN4 induction coincides with heightened anabolic activity, independently of canonical double-strand break signaling at telomeric regions and across the genome. Supporting this, *Zscan4*-expressing cells within the H-LD clones showed no transcriptional evidence of DNA damage responses (Figure S3K). Notably, ZSCAN4 activation appears transient and is likely confined to cells in a transitional state experiencing metabolic stress and telomere dysregulation. Consistent with this, enforcing lipid storage via CIDEA expression or acutely stimulating mitochondrial respiration in ESCs leads to rapid telomere attrition, which itself can trigger sub-telomeric transcription and ZSCAN4 expression.[47,50,82] This suggests a feedback mechanism whereby metabolism-induced telomere stress, occurring during the exit from naive pluripotency, engages ZSCAN4 as a protective response.

Supporting this notion, we show that differentiating ESC-derived 3D spheroids undergo transient telomere shortening, which coincides with LD enlargement, *Zscan4* induction, and subsequent activation of the ALT pathway for telomere restoration—a relationship confirmed at the single-cell level (Figure S3I). Correspondingly, CIDEA depletion inhibits lipid storage and blocks telomere shortening, ZSCAN4 induction, and ALT activation, indicating that these processes are tightly coupled. Collectively, our findings uncover a previously unrecognized mechanism by which developmentally regulated metabolic remodeling is intricately coordinated with ZSCAN4-associated telomere safeguarding in pluripotent cells transitioning from the naive to formative state.

In vitro, ZSCAN4-associated telomere elongation has been observed in steady-state ESCs[35,37,47,50] during somatic cell reprogramming toward pluripotency[83,84] and in certain cancer cell types.[50,85] However, a role for ZSCAN4 during the naive-to-formative pluripotency transition has not been previously reported. *In vivo*, ZSCAN4 is highly and transiently expressed at the late 2C stage of mouse embryogenesis (this study and Yang et al.[86]), where it has been implicated in zygotic genome activation.[34] We show that *Zscan4* expression is also detected, albeit at lower levels, during the morula-to-blastocyst transition, coinciding with active lipid biosynthesis and storage previously reported.[25–28] Inhibition of DGAT enzyme activity during this transition reduced ZSCAN4 levels in *ex vivo* embryo cultures, suggesting that ZSCAN4 induction may be metabolically regulated in the cavitating blastocyst, as observed in ESCs. At this stage, the blastocyst has been reported to actively elongate its telomeres.[74,87] Notably, depletion of *Dcaf11*, a positive regulator of *Zscan4*, results in reduced telomere length in *Dcaf11*-KO blastocyst embryos,[74] further implicating ZSCAN4 in telomere regulation during early development. These findings, along with our own, indicate that telomere length is developmentally regulated. They also reinforce the emerging view that ZSCAN4 reactivation occurs during cell state transitions beyond the canonical 2C embryonic stage.[47,72,84]

An intriguing question is how telomere length becomes transiently shortened in the context of accelerated mitochondrial respiration and heightened anabolic activity in pluripotent progenitors. Mounting evidence points to a link between mitochondrial metabolism and telomere homeostasis across development and diseases.[88–92] In human ESCs, single-cell analyses correlated shorter telomeres with increased expression of oxidative metabolism regulators and lowered expression of telomerase components and shelterin complex recruiters.[93] Notably, telomerase reverse transcriptase (TERT) has been proposed to translocate from the nucleus to mitochondria under oxidative stress, where it may protect against mitochondrial DNA damage.[91,94] Similarly, the shelterin component TIN2 shuttles to mitochondria in response to elevated oxidation, modulating mitochondrial respiration in favor of glycolysis.[95] Future studies could track the localization and activity of TERT, TIN2, and other telomeric regulators to determine their roles in telomere maintenance and metabolic remodeling during pluripotency transitions.

In conclusion, our study reveals a tightly coordinated interplay between metabolic remodeling and ZSCAN4-associated telomere safeguarding in developing pluripotent progenitors. The fundamental importance of telomere protection is underscored by evidence that pluripotent and adult stem cell progenitors with short telomeres exhibit impaired developmental potential.[74,78,96,97] Whether metabolism-induced telomere shortening or direct inactivation of *Zscan4* alone leads to similar developmental defects remains an open question. Notably, the expression of ZSCAN4 in certain cancer cells, coupled with the central role of metabolic rewiring in tumorigenesis, raises the possibility that telomere regulation mechanisms identified here may be co-opted in pathological contexts. These insights highlight the value of studying metabolic switches and telomere biology as interdependent processes—an approach likely to yield important advances in both fundamental developmental biology and clinical research.

Limitations of the study

Our study uncovers a ZSCAN4-associated mechanism through which telomere homeostasis is maintained during essential metabolic reprogramming. However, it remains to be determined whether ZSCAN4 directly mediates ALT activation and telomere extension, or whether ALT pathway itself is subjected to metabolic regulation. Given the critical need to safeguard telomere integrity in pluripotent progenitors prior to differentiation, it is plausible that ALT and TERT-mediated pathways

operate redundantly to restore telomere length following attrition. Such redundancy may confer robustness and flexibility, hallmarks of early embryonic development, ensuring genome stability amid dynamic metabolic transitions.

RESOURCE AVAILABILITY

Lead contact

Requests for further information and material should be directed to the lead contact, Véronique Azuara (v.azuara@imperial.ac.uk).

Materials availability

Plasmids and genetically modified cell lines generated in this study are available upon request.

Data and code availability

- The bulk and scRNA-seq data reported in this study have been deposited into Gene Expression Omnibus under GEO: GSE271241. The accession numbers of public data used in this study are listed in Table S5.
- No original code is reported in this study.

ACKNOWLEDGMENTS

We thank Taiping Chen, Wolf Reik, and Austin Smith for providing the pCAG-3XFlag-Zscan4c plasmid, pCAG-Zscan4c:eGFP plasmid, and Rex1/Zfp42-GFP ESC line, respectively. Thanks to King Hang Tommy Mau for help with the initial characterization of LD clones; Danielle Admiraal, Dick W. Zijlmans, and Pascal W.T.C. Jansen for help with ChEP; Ruth Knops for help with LC-MS; Laura Wingens for help with scRNA-seq at the Sequencing Facility at the RIMLS; Chad Whilding and Dirk Dormann at the MRC LMS Microscopy Facility; and James Elliot at the LMS/NIHR Imperial Biomedical Research Centre Flow Cytometry Facility. This work was supported by Genesis Research Trust, UK, to V.A.; Biotechnology and Biological Sciences Research Council, UK, to V.A. (BB/P005179/1) and M.C. (BB/P005209/2 and BB/H020233/1); the Dutch research organization, the Netherlands, to H.M. (NWO XS - OCENW.XS22.3.119 and NWO XL - OCENW.XL21.XL21.100); Medical Research Council and UKRI Future Leaders Fellowship, UK, to M.P. (MRC, MC_UP_1605/4 and MC_EX_MR/S015930/1); Imperial College President PhD scholarships, UK (D.K. and R.A.d.S.); and Tommy's National Centre for Miscarriage Research, UK (C.L.N.).

AUTHOR CONTRIBUTIONS

R.A.d.S. performed most experiments and data analyses with contributions from D.B., D.K., N.G.P.B., Y.Z., E.J.E.M.K., C.L.N., J.K.E., B.J.L., S.L., M.P.B., Z.L., B.C.S., A.F.L.-C., and J.H.J.; M.B. supervised the mathematical analysis; M.P. supervised the embryo experiments; H.C.K. supervised the GC-MS experiments; M.C. supervised the generation and initial characterization of L-LD and H-LD clones; H.M. supervised scRNA-seq and ChEP experiments; V.A. conceptualized, designed, and supervised the study; and V.A. and R.A.d.S. wrote the manuscript with inputs from other authors.

DECLARATION OF INTERESTS

The authors declare no competing interests.

STAR★METHODS

Detailed methods are provided in the online version of this paper and include the following:

SUPPLEMENTAL INFORMATION

Supplemental information can be found online at https://doi.org/10.1016/j.celrep.2025.116654.

Received: July 15, 2024
Revised: July 3, 2025
Accepted: November 12, 2025

REFERENCES

1. Rossant, J., and Tam, P.P.L. (2009). Blastocyst lineage formation, early embryonic asymmetries and axis patterning in the mouse. Development *136*, 701–713. https://doi.org/10.1242/dev.017178.
2. Wang, N., Xu, S., and Egli, D. (2023). Replication stress in mammalian embryo development, differentiation, and reprogramming. Trends Cell Biol. *33*, 872–886. https://doi.org/10.1016/j.tcb.2023.03.015.
3. Nichols, J., and Smith, A. (2009). Naive and primed pluripotent states. Cell Stem Cell *4*, 487–492. https://doi.org/10.1016/j.stem.2009.05.015.
4. Smith, A. (2017). Formative pluripotency: the executive phase in a developmental continuum. Development *144*, 365–373. https://doi.org/10.1242/dev.142679.
5. Beddington, R.S., and Robertson, E.J. (1999). Axis development and early asymmetry in mammals. Cell *96*, 195–209.
6. Bedzhov, I., and Zernicka-Goetz, M. (2014). Self-organizing properties of mouse pluripotent cells initiate morphogenesis upon implantation. Cell *156*, 1032–1044. https://doi.org/10.1016/j.cell.2014.01.023.
7. Evans, M.J., and Kaufman, M.H. (1981). Establishment in culture of pluripotential cells from mouse embryos. Nature *292*, 154–156.
8. Martin, G.R. (1981). Isolation of a pluripotent cell line from early mouse embryos cultured in medium conditioned by teratocarcinoma stem cells. Proc. Natl. Acad. Sci. USA *78*, 7634–7638.
9. Tesar, P.J., Chenoweth, J.G., Brook, F.A., Davies, T.J., Evans, E.P., Mack, D.L., Gardner, R.L., and McKay, R.D.G. (2007). New cell lines

from mouse epiblast share defining features with human embryonic stem cells. Nature *448*, 196–199. https://doi.org/10.1038/nature05972.

10. Brons, I.G.M., Smithers, L.E., Trotter, M.W.B., Rugg-Gunn, P., Sun, B., Chuva de Sousa Lopes, S.M., Howlett, S.K., Clarkson, A., Ahrlund-Richter, L., Pedersen, R.A., and Vallier, L. (2007). Derivation of pluripotent epiblast stem cells from mammalian embryos. Nature *448*, 191–195. https://doi.org/10.1038/nature05950.
11. Kalkan, T., Olova, N., Roode, M., Mulas, C., Lee, H.J., Nett, I., Marks, H., Walker, R., Stunnenberg, H.G., Lilley, K.S., et al. (2017). Tracking the embryonic stem cell transition from ground state pluripotency. Development *144*, 1221–1234. https://doi.org/10.1242/dev.142711.
12. Marks, H., Kalkan, T., Menafra, R., Denissov, S., Jones, K., Hofemeister, H., Nichols, J., Kranz, A., Stewart, A.F., Smith, A., and Stunnenberg, H.G. (2012). The transcriptional and epigenomic foundations of ground state pluripotency. Cell *149*, 590–604. https://doi.org/10.1016/j.cell.2012.03.026.
13. Leitch, H.G., McEwen, K.R., Turp, A., Encheva, V., Carroll, T., Grabole, N., Mansfield, W., Nashun, B., Knezovich, J.G., Smith, A., et al. (2013). Naive pluripotency is associated with global DNA hypomethylation. Nat. Struct. Mol. Biol. *20*, 311–316. https://doi.org/10.1038/nsmb.2510.
14. Zhou, W., Choi, M., Margineantu, D., Margaretha, L., Hesson, J., Cavanaugh, C., Blau, C.A., Horwitz, M.S., Hockenbery, D., Ware, C., and Ruohola-Baker, H. (2012). HIF1alpha induced switch from bivalent to exclusively glycolytic metabolism during ESC-to-EpiSC/hESC transition. EMBO J. *31*, 2103–2116. https://doi.org/10.1038/emboj.2012.71.
15. Weinberger, L., Ayyash, M., Novershtern, N., and Hanna, J.H. (2016). Dynamic stem cell states: naive to primed pluripotency in rodents and humans. Nat. Rev. Mol. Cell Biol. *17*, 155–169. https://doi.org/10.1038/nrm.2015.28.
16. Bell, E., Curry, E.W., Megchelenbrink, W., Jouneau, L., Brochard, V., Tomaz, R.A., Mau, K.H.T., Atlasi, Y., de Souza, R.A., Marks, H., et al. (2020). Dynamic CpG methylation delineates subregions within super-enhancers selectively decommissioned at the exit from naive pluripotency. Nat. Commun. *11*, 1112. https://doi.org/10.1038/s41467-020-14916-7.
17. Hayashi, K., Ohta, H., Kurimoto, K., Aramaki, S., and Saitou, M. (2011). Reconstitution of the mouse germ cell specification pathway in culture by pluripotent stem cells. Cell *146*, 519–532. https://doi.org/10.1016/j.cell.2011.06.052.
18. Shahbazi, M.N., Scialdone, A., Skorupska, N., Weberling, A., Recher, G., Zhu, M., Jedrusik, A., Devito, L.G., Noli, L., Macaulay, I.C., et al. (2017). Pluripotent state transitions coordinate morphogenesis in mouse and human embryos. Nature *552*, 239–243. https://doi.org/10.1038/nature24675.
19. Houghton, F.D., Thompson, J.G., Kennedy, C.J., and Leese, H.J. (1996). Oxygen consumption and energy metabolism of the early mouse embryo. Mol. Reprod. Dev. *44*, 476–485. https://doi.org/10.1002/(SICI)1098-2795(199608)44:4<476::AID-MRD7>3.0.CO;2-I.
20. Hillman, N., and Flynn, T.J. (1980). The metabolism of exogenous fatty acids by preimplantation mouse embryos developing in vitro. J. Embryol. Exp. Morphol. *56*, 157–168.
21. Brinster, R.L. (1969). Incorporation of carbon from glucose and pyruvate into the preimplantation mouse embryo. Exp. Cell Res. *58*, 153–158. https://doi.org/10.1016/0014-4827(69)90125-6.
22. Martin, K.L., and Leese, H.J. (1995). Role of glucose in mouse preimplantation embryo development. Mol. Reprod. Dev. *40*, 436–443. https://doi.org/10.1002/mrd.1080400407.
23. Leese, H.J. (2012). Metabolism of the preimplantation embryo: 40 years on. Reproduction *143*, 417–427. https://doi.org/10.1530/REP-11-0484.
24. Wang, G., Tsujii, H., and Khandoker, M. (1998). Fatty acid compositions of mouse embryo, oviduct and uterine fluid. J. Anim. Sci. Technol. *69*, 923–928.
25. Watanabe, T., Thayil, A., Jesacher, A., Grieve, K., Debarre, D., Wilson, T., Booth, M., and Srinivas, S. (2010). Characterisation of the dynamic behaviour of lipid droplets in the early mouse embryo using adaptive harmonic generation microscopy. BMC Cell Biol. *11*, 38. https://doi.org/10.1186/1471-2121-11-38.
26. Bradley, J., Pope, I., Masia, F., Sanusi, R., Langbein, W., Swann, K., and Borri, P. (2016). Quantitative imaging of lipids in live mouse oocytes and early embryos using CARS microscopy. Development *143*, 2238–2247. https://doi.org/10.1242/dev.129908.
27. Aizawa, R., Ibayashi, M., Tatsumi, T., Yamamoto, A., Kokubo, T., Miyasaka, N., Sato, K., Ikeda, S., Minami, N., and Tsukamoto, S. (2019). Synthesis and maintenance of lipid droplets are essential for mouse preimplantation embryonic development. Development *146*, dev181925. https://doi.org/10.1242/dev.181925.
28. Mau, K.H.T., Karimlou, D., Barneda, D., Brochard, V., Royer, C., Leeke, B., de Souza, R.A., Pailles, M., Percharde, M., Srinivas, S., et al. (2022). Dynamic enlargement and mobilization of lipid droplets in pluripotent cells coordinate morphogenesis during mouse peri-implantation development. Nat. Commun. *13*, 3861. https://doi.org/10.1038/s41467-022-31323-2.
29. Olzmann, J.A., and Carvalho, P. (2019). Dynamics and functions of lipid droplets. Nat. Rev. Mol. Cell Biol. *20*, 137–155. https://doi.org/10.1038/s41580-018-0085-z.
30. Walther, T.C., and Farese, R.V., Jr. (2012). Lipid droplets and cellular lipid metabolism. Annu. Rev. Biochem. *81*, 687–714. https://doi.org/10.1146/annurev-biochem-061009-102430.
31. Barneda, D., Planas-Iglesias, J., Gaspar, M.L., Mohammadyani, D., Prasannan, S., Dormann, D., Han, G.S., Jesch, S.A., Carman, G.M., Kagan, V., et al. (2015). The brown adipocyte protein CIDEA promotes lipid droplet fusion via a phosphatidic acid-binding amphipathic helix. eLife *4*, e07485. https://doi.org/10.7554/eLife.07485.
32. Hayashi, K., de Sousa Lopes, S.M.C., Tang, F., Lao, K., and Surani, M.A. (2008). Dynamic equilibrium and heterogeneity of mouse pluripotent stem cells with distinct functional and epigenetic states. Cell Stem Cell *3*, 391–401. https://doi.org/10.1016/j.stem.2008.07.027.
33. Wray, J., Kalkan, T., Gomez-Lopez, S., Eckardt, D., Cook, A., Kemler, R., and Smith, A. (2011). Inhibition of glycogen synthase kinase-3 alleviates Tcf3 repression of the pluripotency network and increases embryonic stem cell resistance to differentiation. Nat. Cell Biol. *13*, 838–845. https://doi.org/10.1038/ncb2267.
34. Falco, G., Lee, S.L., Stanghellini, I., Bassey, U.C., Hamatani, T., and Ko, M.S.H. (2007). Zscan4: a novel gene expressed exclusively in late 2-cell embryos and embryonic stem cells. Dev. Biol. *307*, 539–550. https://doi.org/10.1016/j.ydbio.2007.05.003.
35. Zalzman, M., Falco, G., Sharova, L.V., Nishiyama, A., Thomas, M., Lee, S.L., Stagg, C.A., Hoang, H.G., Yang, H.T., Indig, F.E., et al. (2010). Zscan4 regulates telomere elongation and genomic stability in ES cells. Nature *464*, 858–863. https://doi.org/10.1038/nature08882.
36. Akiyama, T., Xin, L., Oda, M., Sharov, A.A., Amano, M., Piao, Y., Cadet, J.S., Dudekula, D.B., Qian, Y., Wang, W., et al. (2015). Transient bursts of Zscan4 expression are accompanied by the rapid derepression of heterochromatin in mouse embryonic stem cells. DNA Res. *22*, 307–318. https://doi.org/10.1093/dnares/dsv013.
37. Dan, J., Rousseau, P., Hardikar, S., Veland, N., Wong, J., Autexier, C., and Chen, T. (2017). Zscan4 Inhibits Maintenance DNA Methylation to Facilitate Telomere Elongation in Mouse Embryonic Stem Cells. Cell Rep. *20*, 1936–1949. https://doi.org/10.1016/j.celrep.2017.07.070.
38. Ying, Q.L., Wray, J., Nichols, J., Batlle-Morera, L., Doble, B., Woodgett, J., Cohen, P., and Smith, A. (2008). The ground state of embryonic stem cell self-renewal. Nature *453*, 519–523. https://doi.org/10.1038/nature06968.
39. Liu, Z. (2019). Unsupervised learning with graph theoretical algorithms and its applications to transcriptomic data analysis. https://doi.org/10.25560/70845.

40. Factor, D.C., Corradin, O., Zentner, G.E., Saiakhova, A., Song, L., Chenoweth, J.G., McKay, R.D., Crawford, G.E., Scacheri, P.C., and Tesar, P.J. (2014). Epigenomic comparison reveals activation of "seed" enhancers during transition from naive to primed pluripotency. Cell Stem Cell *14*, 854–863. https://doi.org/10.1016/j.stem.2014.05.005.

41. Buecker, C., Srinivasan, R., Wu, Z., Calo, E., Acampora, D., Faial, T., Simeone, A., Tan, M., Swigut, T., and Wysocka, J. (2014). Reorganization of enhancer patterns in transition from naive to primed pluripotency. Cell Stem Cell *14*, 838–853. https://doi.org/10.1016/j.stem.2014.04.003.

42. Zhong, L., Gordillo, M., Wang, X., Qin, Y., Huang, Y., Soshnev, A., Kumar, R., Nanjangud, G., James, D., David Allis, C., et al. (2023). Dual role of lipids for genome stability and pluripotency facilitates full potency of mouse embryonic stem cells. Protein Cell *14*, 591–602. https://doi.org/10.1093/procel/pwad008.

43. Vardhana, S.A., Arnold, P.K., Rosen, B.P., Chen, Y., Carey, B.W., Huangfu, D., Carmona Fontaine, C., Thompson, C.B., and Finley, L.W.S. (2019). Glutamine independence is a selectable feature of pluripotent stem cells. Nat. Metab. *1*, 676–687. https://doi.org/10.1038/s42255-019-0082-3.

44. Ben-David, U., Gan, Q.-F., Golan-Lev, T., Arora, P., Yanuka, O., Oren, Y.S., Leikin-Frenkel, A., Graf, M., Garippa, R., Boehringer, M., et al. (2013). Selective Elimination of Human Pluripotent Stem Cells by an Oleate Synthesis Inhibitor Discovered in a High-Throughput Screen. Cell Stem Cell *12*, 167–179. https://doi.org/10.1016/j.stem.2012.11.015.

45. Sperber, H., Mathieu, J., Wang, Y., Ferreccio, A., Hesson, J., Xu, Z., Fischer, K.A., Devi, A., Detraux, D., Gu, H., et al. (2015). The metabolome regulates the epigenetic landscape during naive-to-primed human embryonic stem cell transition. Nat. Cell Biol. *17*, 1523–1535. https://doi.org/10.1038/ncb3264.

46. Kustatscher, G., Wills, K.L.H., Furlan, C., and Rappsilber, J. (2014). Chromatin enrichment for proteomics. Nat. Protoc. *9*, 2090–2099. https://doi.org/10.1038/nprot.2014.142.

47. Nakai-Futatsugi, Y., and Niwa, H. (2016). Zscan4 Is Activated after Telomere Shortening in Mouse Embryonic Stem Cells. Stem Cell Rep. *6*, 483–495. https://doi.org/10.1016/j.stemcr.2016.02.010.

48. Eckersley-Maslin, M.A., Svensson, V., Krueger, C., Stubbs, T.M., Giehr, P., Krueger, F., Miragaia, R.J., Kyriakopoulos, C., Berrens, R.V., Milagre, I., et al. (2016). MERVL/Zscan4 Network Activation Results in Transient Genome-wide DNA Demethylation of mESCs. Cell Rep. *17*, 179–192. https://doi.org/10.1016/j.celrep.2016.08.087.

49. Macfarlan, T.S., Gifford, W.D., Driscoll, S., Lettieri, K., Rowe, H.M., Bonanomi, D., Firth, A., Singer, O., Trono, D., and Pfaff, S.L. (2012). Embryonic stem cell potency fluctuates with endogenous retrovirus activity. Nature *487*, 57–63. https://doi.org/10.1038/nature11244.

50. Dan, J., Zhou, Z., Wang, F., Wang, H., Guo, R., Keefe, D.L., and Liu, L. (2022). Zscan4 Contributes to Telomere Maintenance in Telomerase-Deficient Late Generation Mouse ESCs and Human ALT Cancer Cells. Cells *11*, 456. https://doi.org/10.3390/cells11030456.

51. Zhang, C., Wen, H., Liu, S., Fu, E., Yu, L., Chen, S., Han, Q., Li, Z., and Liu, N. (2022). Maternal Factor Dppa3 Activates 2C-Like Genes and Depresses DNA Methylation in Mouse Embryonic Stem Cells. Front. Cell Dev. Biol. *10*, 882671. https://doi.org/10.3389/fcell.2022.882671.

52. Fussner, E., Djuric, U., Strauss, M., Hotta, A., Perez-Iratxeta, C., Lanner, F., Dilworth, F.J., Ellis, J., and Bazett-Jones, D.P. (2011). Constitutive heterochromatin reorganization during somatic cell reprogramming. EMBO J. *30*, 1778–1789. https://doi.org/10.1038/emboj.2011.96.

53. Novo, C.L., Wong, E.V., Hockings, C., Poudel, C., Sheekey, E., Wiese, M., Okkenhaug, H., Boulton, S.J., Basu, S., Walker, S., et al. (2022). Satellite repeat transcripts modulate heterochromatin condensates and safeguard chromosome stability in mouse embryonic stem cells. Nat. Commun. *13*, 3525. https://doi.org/10.1038/s41467-022-31198-3.

54. Klein, A.M., Mazutis, L., Akartuna, I., Tallapragada, N., Veres, A., Li, V., Peshkin, L., Weitz, D.A., and Kirschner, M.W. (2015). Droplet barcoding for single-cell transcriptomics applied to embryonic stem cells. Cell *161*, 1187–1201. https://doi.org/10.1016/j.cell.2015.04.044.

55. Zhang, W., Chen, F., Chen, R., Xie, D., Yang, J., Zhao, X., Guo, R., Zhang, Y., Shen, Y., Göke, J., et al. (2019). Zscan4c activates endogenous retrovirus MERVL and cleavage embryo genes. Nucleic Acids Res. *47*, 8485–8501. https://doi.org/10.1093/nar/gkz594.

56. De Iaco, A., Planet, E., Coluccio, A., Verp, S., Duc, J., and Trono, D. (2017). DUX-family transcription factors regulate zygotic genome activation in placental mammals. Nat. Genet. *49*, 941–945. https://doi.org/10.1038/ng.3858.

57. Hu, Z., Tan, D.E.K., Chia, G., Tan, H., Leong, H.F., Chen, B.J., Lau, M.S., Tan, K.Y.S., Bi, X., Yang, D., et al. (2020). Maternal factor NELFA drives a 2C-like state in mouse embryonic stem cells. Nat. Cell Biol. *22*, 175–186. https://doi.org/10.1038/s41556-019-0453-8.

58. Ishiuchi, T., Enriquez-Gasca, R., Mizutani, E., Bošković, A., Ziegler-Birling, C., Rodriguez-Terrones, D., Wakayama, T., Vaquerizas, J.M., and Torres-Padilla, M.-E. (2015). Early embryonic-like cells are induced by downregulating replication-dependent chromatin assembly. Nat. Struct. Mol. Biol. *22*, 662–671. https://doi.org/10.1038/nsmb.3066.

59. Dan, J., Liu, Y., Liu, N., Chiourea, M., Okuka, M., Wu, T., Ye, X., Mou, C., Wang, L., Wang, L., et al. (2014). Rif1 maintains telomere length homeostasis of ESCs by mediating heterochromatin silencing. Dev. Cell *29*, 7–19. https://doi.org/10.1016/j.devcel.2014.03.004.

60. Guo, R., Ye, X., Yang, J., Zhou, Z., Tian, C., Wang, H., Wang, H., Fu, H., Liu, C., Zeng, M., et al. (2018). Feeders facilitate telomere maintenance and chromosomal stability of embryonic stem cells. Nat. Commun. *9*, 2620. https://doi.org/10.1038/s41467-018-05038-2.

61. Tian, C., Wang, J., Ye, X., Chen, J., Zheng, R., Yu, H., Li, J., Yin, G., Liu, L., Zhao, N., et al. (2023). Culture conditions of mouse ESCs impact the tumor appearance in vivo. Cell Rep. *42*, 112645. https://doi.org/10.1016/j.celrep.2023.112645.

62. Acampora, D., Di Giovannantonio, L.G., Garofalo, A., Nigro, V., Omodei, D., Lombardi, A., Zhang, J., Chambers, I., and Simeone, A. (2017). Functional Antagonism between OTX2 and NANOG Specifies a Spectrum of Heterogeneous Identities in Embryonic Stem Cells. Stem Cell Rep. *9*, 1642–1659. https://doi.org/10.1016/j.stemcr.2017.09.019.

63. Hackett, J.A., and Surani, M.A. (2014). Regulatory principles of pluripotency: from the ground state up. Cell Stem Cell *15*, 416–430. https://doi.org/10.1016/j.stem.2014.09.015.

64. Storm, M.P., Kumpfmueller, B., Bone, H.K., Buchholz, M., Sanchez Ripoll, Y., Chaudhuri, J.B., Niwa, H., Tosh, D., and Welham, M.J. (2014). Zscan4 is regulated by PI3-kinase and DNA-damaging agents and directly interacts with the transcriptional repressors LSD1 and CtBP2 in mouse embryonic stem cells. PLoS One *9*, e89821. https://doi.org/10.1371/journal.pone.0089821.

65. Sottnik, J.L., Lori, J.C., Rose, B.J., and Thamm, D.H. (2011). Glycolysis inhibition by 2-deoxy-D-glucose reverts the metastatic phenotype in vitro and in vivo. Clin. Exp. Metastasis *28*, 865–875. https://doi.org/10.1007/s10585-011-9417-5.

66. Schoenmann, N., Tannenbaum, N., Hodgeman, R.M., and Raju, R.P. (2023). Regulating mitochondrial metabolism by targeting pyruvate dehydrogenase with dichloroacetate, a metabolic messenger. Biochim. Biophys. Acta. Mol. Basis Dis. *1869*, 166769. https://doi.org/10.1016/j.bbadis.2023.166769.

67. Tischler, J., Gruhn, W.H., Reid, J., Allgeyer, E., Buettner, F., Marr, C., Theis, F., Simons, B.D., Wernisch, L., and Surani, M.A. (2019). Metabolic regulation of pluripotency and germ cell fate through alpha-ketoglutarate. EMBO J. *38*, e99518. https://doi.org/10.15252/embj.201899518.

68. Petillo, A., Abruzzese, V., Koshal, P., Ostuni, A., and Bisaccia, F. (2020). Extracellular Citrate Is a Trojan Horse for Cancer Cells. Front. Mol. Biosci. *7*, 593866. https://doi.org/10.3389/fmolb.2020.593866.

69. Deng, Q., Ramsköld, D., Reinius, B., and Sandberg, R. (2014). Single-cell RNA-seq reveals dynamic, random monoallelic gene expression

in mammalian cells. Science *343*, 193–196. https://doi.org/10.1126/science.1245316.

70. Srinivasan, R., Nady, N., Arora, N., Hsieh, L.J., Swigut, T., Narlikar, G.J., Wossidlo, M., and Wysocka, J. (2020). Zscan4 binds nucleosomal microsatellite DNA and protects mouse two-cell embryos from DNA damage. Sci. Adv. *6*, eaaz9115. https://doi.org/10.1126/sciadv.aaz9115.

71. Tsai, L.-K., Peng, M., Chang, C.-C., Wen, L., Liu, L., Liang, X., Chen, Y.E., Xu, J., and Sung, L.-Y. (2023). ZSCAN4 interacts with PARP1 to promote DNA repair in mouse embryonic stem cells. Cell Biosci. *13*, 193. https://doi.org/10.1186/s13578-023-01140-1.

72. Jiang, J., Lv, W., Ye, X., Wang, L., Zhang, M., Yang, H., Okuka, M., Zhou, C., Zhang, X., Liu, L., and Li, J. (2013). Zscan4 promotes genomic stability during reprogramming and dramatically improves the quality of iPS cells as demonstrated by tetraploid complementation. Cell Res. *23*, 92–106. https://doi.org/10.1038/cr.2012.157.

73. Callicott, R.J., and Womack, J.E. (2006). Real-time PCR assay for measurement of mouse telomeres. Comp. Med. *56*, 17–22.

74. Le, R., Huang, Y., Zhang, Y., Wang, H., Lin, J., Dong, Y., Li, Z., Guo, M., Kou, X., Zhao, Y., et al. (2021). Dcaf11 activates Zscan4-mediated alternative telomere lengthening in early embryos and embryonic stem cells. Cell Stem Cell *28*, 732–747.e9. https://doi.org/10.1016/j.stem.2020.11.018.

75. Bryan, T.M., Englezou, A., Gupta, J., Bacchetti, S., and Reddel, R.R. (1995). Telomere elongation in immortal human cells without detectable telomerase activity. EMBO J. *14*, 4240–4248. https://doi.org/10.1002/j.1460-2075.1995.tb00098.x.

76. Liu, L., Bailey, S.M., Okuka, M., Muñoz, P., Li, C., Zhou, L., Wu, C., Czerwiec, E., Sandler, L., Seyfang, A., et al. (2007). Telomere lengthening early in development. Nat. Cell Biol. *9*, 1436–1441. https://doi.org/10.1038/ncb1664.

77. Henson, J.D., Cao, Y., Huschtscha, L.I., Chang, A.C., Au, A.Y.M., Pickett, H.A., and Reddel, R.R. (2009). DNA C-circles are specific and quantifiable markers of alternative-lengthening-of-telomeres activity. Nat. Biotechnol. *27*, 1181–1185. https://doi.org/10.1038/nbt.1587.

78. Cesare, A.J., and Reddel, R.R. (2010). Alternative lengthening of telomeres: models, mechanisms and implications. Nat. Rev. Genet. *11*, 319–330. https://doi.org/10.1038/nrg2763.

79. Arnold, P.K., Jackson, B.T., Paras, K.I., Brunner, J.S., Hart, M.L., Newsom, O.J., Alibeckoff, S.P., Endress, J., Drill, E., Sullivan, L.B., and Finley, L.W.S. (2022). A non-canonical tricarboxylic acid cycle underlies cellular identity. Nature *603*, 477–481. https://doi.org/10.1038/s41586-022-04475-w.

80. Ramosaj, M., Madsen, S., Maillard, V., Scandella, V., Sudria-Lopez, D., Yuizumi, N., Telley, L., and Knobloch, M. (2021). Lipid droplet availability affects neural stem/progenitor cell metabolism and proliferation. Nat. Commun. *12*, 7362. https://doi.org/10.1038/s41467-021-27365-7.

81. Yue, F., Oprescu, S.N., Qiu, J., Gu, L., Zhang, L., Chen, J., Narayanan, N., Deng, M., and Kuang, S. (2022). Lipid droplet dynamics regulate adult muscle stem cell fate. Cell Rep. *38*, 110267. https://doi.org/10.1016/j.celrep.2021.110267.

82. Benetti, R., García-Cao, M., and Blasco, M.A. (2007). Telomere length regulates the epigenetic status of mammalian telomeres and subtelomeres. Nat. Genet. *39*, 243–250. https://doi.org/10.1038/ng1952.

83. Cheng, Z.L., Zhang, M.L., Lin, H.P., Gao, C., Song, J.B., Zheng, Z., Li, L., Zhang, Y., Shen, X., Zhang, H., et al. (2020). The Zscan4-Tet2 Transcription Nexus Regulates Metabolic Rewiring and Enhances Proteostasis to Promote Reprogramming. Cell Rep. *32*, 107877. https://doi.org/10.1016/j.celrep.2020.107877.

84. Hirata, T., Amano, T., Nakatake, Y., Amano, M., Piao, Y., Hoang, H.G., and Ko, M.S.H. (2012). Zscan4 transiently reactivates early embryonic genes during the generation of induced pluripotent stem cells. Sci. Rep. *2*, 208. https://doi.org/10.1038/srep00208.

85. Portney, B.A., Khatri, R., Meltzer, W.A., Mariano, J.M., and Zalzman, M. (2018). ZSCAN4 is negatively regulated by the ubiquitin-proteasome system and the E3 ubiquitin ligase RNF20. Biochem. Biophys. Res. Commun. *498*, 72–78. https://doi.org/10.1016/j.bbrc.2018.02.155.

86. Yang, J., Dan, J., Zhao, N., Liu, L., Wang, H., Liu, Q., Wang, L., Li, J., Wu, Y., Chen, F., et al. (2024). Zscan4 mediates ubiquitination and degradation of the corepressor complex to promote chromatin accessibility in 2C-like cells. Proc. Natl. Acad. Sci. USA *121*, e2407490121. https://doi.org/10.1073/pnas.2407490121.

87. Tardat, M., and Déjardin, J. (2018). Telomere chromatin establishment and its maintenance during mammalian development. Chromosoma *127*, 3–18. https://doi.org/10.1007/s00412-017-0656-3.

88. Cattan, V., Mercier, N., Gardner, J.P., Regnault, V., Labat, C., Mäki-Jouppila, J., Nzietchueng, R., Benetos, A., Kimura, M., Aviv, A., and Lacolley, P. (2008). Chronic oxidative stress induces a tissue-specific reduction in telomere length in CAST/Ei mice. Free Radic. Biol. Med. *44*, 1592–1598. https://doi.org/10.1016/j.freeradbiomed.2008.01.007.

89. Gavia-Garcia, G., Rosado-Perez, J., Arista-Ugalde, T.L., Aguiniga-Sanchez, I., Santiago-Osorio, E., and Mendoza-Nunez, V.M. (2021). Telomere Length and Oxidative Stress and Its Relation with Metabolic Syndrome Components in the Aging. Biol. Basel *10*, 253. https://doi.org/10.3390/biology10040253.

90. Ko, E., Seo, H.W., and Jung, G. (2018). Telomere length and reactive oxygen species levels are positively associated with a high risk of mortality and recurrence in hepatocellular carcinoma. Hepatology *67*, 1378–1391. https://doi.org/10.1002/hep.29604.

91. Haendeler, J., Drose, S., Buchner, N., Jakob, S., Altschmied, J., Goy, C., Spyridopoulos, I., Zeiher, A.M., Brandt, U., and Dimmeler, S. (2009). Mitochondrial telomerase reverse transcriptase binds to and protects mitochondrial DNA and function from damage. Arter. Thromb Vasc Biol *29*, 929–935. https://doi.org/10.1161/ATVBAHA.109.185546.

92. Opresko, P.L., Fan, J., Danzy, S., Wilson, D.M., 3rd, and Bohr, V.A. (2005). Oxidative damage in telomeric DNA disrupts recognition by TRF1 and TRF2. Nucleic Acids Res. *33*, 1230–1239. https://doi.org/10.1093/nar/gki273.

93. Wang, H., Zhang, K., Liu, Y., Fu, Y., Gao, S., Gong, P., Wang, H., Zhou, Z., Zeng, M., Wu, Z., et al. (2017). Telomere heterogeneity linked to metabolism and pluripotency state revealed by simultaneous analysis of telomere length and RNA-seq in the same human embryonic stem cell. BMC Biol. *15*, 114. https://doi.org/10.1186/s12915-017-0453-8.

94. Haendeler, J., Hoffmann, J., Diehl, J.F., Vasa, M., Spyridopoulos, I., Zeiher, A.M., and Dimmeler, S. (2004). Antioxidants inhibit nuclear export of telomerase reverse transcriptase and delay replicative senescence of endothelial cells. Circ. Res. *94*, 768–775. https://doi.org/10.1161/01.RES.0000121104.05977.F3.

95. Chen, L.Y., Zhang, Y., Zhang, Q., Li, H., Luo, Z., Fang, H., Kim, S.H., Qin, L., Yotnda, P., Xu, J., et al. (2012). Mitochondrial localization of telomeric protein TIN2 links telomere regulation to metabolic control. Mol. Cell *47*, 839–850. https://doi.org/10.1016/j.molcel.2012.07.002.

96. Pucci, F., Gardano, L., and Harrington, L. (2013). Short Telomeres in ESCs Lead to Unstable Differentiation. Cell Stem Cell *12*, 479–486. https://doi.org/10.1016/j.stem.2013.01.018.

97. Huang, J., Wang, F., Okuka, M., Liu, N., Ji, G., Ye, X., Zuo, B., Li, M., Liang, P., Ge, W.W., et al. (2011). Association of telomere length with authentic pluripotency of ES/iPS cells. Cell Res. *21*, 779–792. https://doi.org/10.1038/cr.2011.16.

98. Schindelin, J., Arganda-Carreras, I., Frise, E., Kaynig, V., Longair, M., Pietzsch, T., Preibisch, S., Rueden, C., Saalfeld, S., Schmid, B., et al. (2012). Fiji: an open-source platform for biological-image analysis. Nat. Methods *9*, 676–682. https://doi.org/10.1038/nmeth.2019.

99. Stirling, D.R., Swain-Bowden, M.J., Lucas, A.M., Carpenter, A.E., Cimini, B.A., and Goodman, A. (2021). CellProfiler 4: improvements in speed, utility and usability. BMC Bioinf. *22*, 433. https://doi.org/10.1186/s12859-021-04344-9.

100. Behrends, V., Tredwell, G.D., and Bundy, J.G. (2011). A software complement to AMDIS for processing GC-MS metabolomic data. Anal. Biochem. *415*, 206–208. https://doi.org/10.1016/j.ab.2011.04.009.

101. Hartler, J., Triebl, A., Ziegl, A., Trötzmüller, M., Rechberger, G.N., Zeleznik, O.A., Zierler, K.A., Torta, F., Cazenave-Gassiot, A., Wenk, M.R., et al. (2017). Deciphering lipid structures based on platform-independent decision rules. Nat. Methods *14*, 1171–1174. https://doi.org/10.1038/nmeth.4470.

102. Cox, J., and Mann, M. (2008). MaxQuant enables high peptide identification rates, individualized p.p.b.-range mass accuracies and proteome-wide protein quantification. Nat. Biotechnol. *26*, 1367–1372. https://doi.org/10.1038/nbt.1511.

103. Tyanova, S., Temu, T., Sinitcyn, P., Carlson, A., Hein, M.Y., Geiger, T., Mann, M., and Cox, J. (2016). The Perseus computational platform for comprehensive analysis of (prote)omics data. Nat. Methods *13*, 731–740. https://doi.org/10.1038/nmeth.3901.

104. Bolger, A.M., Lohse, M., and Usadel, B. (2014). Trimmomatic: a flexible trimmer for Illumina sequence data. Bioinformatics *30*, 2114–2120. https://doi.org/10.1093/bioinformatics/btu170.

105. Bray, N.L., Pimentel, H., Melsted, P., and Pachter, L. (2016). Near-optimal probabilistic RNA-seq quantification. Nat. Biotechnol. *34*, 525–527. https://doi.org/10.1038/nbt.3519.

106. Love, M.I., Huber, W., and Anders, S. (2014). Moderated estimation of fold change and dispersion for RNA-seq data with DESeq2. Genome Biol. *15*, 550. https://doi.org/10.1186/s13059-014-0550-8.

107. Liao, Y., Wang, J., Jaehnig, E.J., Shi, Z., and Zhang, B. (2019). WebGestalt 2019: gene set analysis toolkit with revamped UIs and APIs. Nucleic Acids Res. *47*, W199–W205. https://doi.org/10.1093/nar/gkz401.

108. Gillespie, M., Jassal, B., Stephan, R., Milacic, M., Rothfels, K., Senff-Ribeiro, A., Griss, J., Sevilla, C., Matthews, L., Gong, C., et al. (2022). The reactome pathway knowledgebase 2022. Nucleic Acids Res. *50*, D687–D692. https://doi.org/10.1093/nar/gkab1028.

109. Slenter, D.N., Kutmon, M., Hanspers, K., Riutta, A., Windsor, J., Nunes, N., Mélius, J., Cirillo, E., Coort, S.L., Digles, D., et al. (2018). WikiPathways: a multifaceted pathway database bridging metabolomics to other omics research. Nucleic Acids Res. *46*, D661–D667. https://doi.org/10.1093/nar/gkx1064.

110. Thomas, P.D., Ebert, D., Muruganujan, A., Mushayahama, T., Albou, L.P., and Mi, H. (2022). PANTHER: Making genome-scale phylogenetics accessible to all. Protein Sci. *31*, 8–22. https://doi.org/10.1002/pro.4218.

111. Griffiths, J.A., Richard, A.C., Bach, K., Lun, A.T.L., and Marioni, J.C. (2018). Detection and removal of barcode swapping in single-cell RNA-seq data. Nat. Commun. *9*, 2667. https://doi.org/10.1038/s41467-018-05083-x.

112. Satija, R., Farrell, J.A., Gennert, D., Schier, A.F., and Regev, A. (2015). Spatial reconstruction of single-cell gene expression data. Nat. Biotechnol. *33*, 495–502. https://doi.org/10.1038/nbt.3192.

113. Muskovic, W., and Powell, J.E. (2021). DropletQC: improved identification of empty droplets and damaged cells in single-cell RNA-seq data. Genome Biol. *22*, 329. https://doi.org/10.1186/s13059-021-02547-0.

114. Zappia, L., and Oshlack, A. (2018). Clustering trees: a visualization for evaluating clusterings at multiple resolutions. GigaScience *7*, giy083. https://doi.org/10.1093/gigascience/giy083.

115. Andreatta, M., and Carmona, S.J. (2021). UCell: Robust and scalable single-cell gene signature scoring. Comput. Struct. Biotechnol. J. *19*, 3796–3798. https://doi.org/10.1016/j.csbj.2021.06.043.

116. Trapnell, C., Cacchiarelli, D., Grimsby, J., Pokharel, P., Li, S., Morse, M., Lennon, N.J., Livak, K.J., Mikkelsen, T.S., and Rinn, J.L. (2014). The dynamics and regulators of cell fate decisions are revealed by pseudotemporal ordering of single cells. Nat. Biotechnol. *32*, 381–386. https://doi.org/10.1038/nbt.2859.

117. Johnson, W.E., Li, C., and Rabinovic, A. (2007). Adjusting batch effects in microarray expression data using empirical Bayes methods. Biostatistics *8*, 118–127. https://doi.org/10.1093/biostatistics/kxj037.

118. van der Sande, M., Frölich, S., Schäfers, T., Smits, J.G.A., Snabel, R.R., Rinzema, S., and van Heeringen, S.J. (2023). Seq2science: an end-to-end workflow for functional genomics analysis. PeerJ *11*, e16380. https://doi.org/10.7717/peerj.16380.

119. Millard, P., Letisse, F., Sokol, S., and Portais, J.-C. (2012). IsoCor: correcting MS data in isotope labeling experiments. Bioinformatics *28*, 1294–1296. https://doi.org/10.1093/bioinformatics/bts127.

120. Di Carlo, C., Sousa, B.C., Manfredi, M., Brandi, J., Dalla Pozza, E., Marengo, E., Palmieri, M., Dando, I., Wakelam, M.J.O., Lopez-Clavijo, A.F., and Cecconi, D. (2021). Integrated lipidomics and proteomics reveal cardiolipin alterations, upregulation of HADHA and long chain fatty acids in pancreatic cancer stem cells. Sci. Rep. *11*, 13297. https://doi.org/10.1038/s41598-021-92752-5.

121. Porreca, R.M., Herrera-Moyano, E., Skourti, E., Law, P.P., Gonzalez Franco, R., Montoya, A., Faull, P., Kramer, H., and Vannier, J.-B. (2020). TRF1 averts chromatin remodelling, recombination and replication dependent-break induced replication at mouse telomeres. eLife *9*, e49817. https://doi.org/10.7554/eLife.49817.

STAR★METHODS

KEY RESOURCES TABLE

REAGENT or RESOURCE	SOURCE	IDENTIFIER
Antibodies		
ACLY	Cell Signaling Technologies	Cat# 4332; RRID:AB_2223744
DNMT1	Abcam	Cat# ab87654; RRID:AB_2041077
FASN	Cell Signaling Technologies	Cat# 3180; Clone C20G5; RRID:AB_2100796
GFP	Aves Labs	Cat# GFP-1020; RRID:AB_10000240
GAPDH	Cell Signaling Technologies	Cat# 5174; RRID:AB_10622025
OCT4	Santa Cruz	Cat# sc-5279; RRID:AB_628051
p-ACLY(ser455)	Cell Signaling Technologies	Cat# 4331; RRID:AB_2257987
p-H2AX(ser139)	Cell Signaling Technologies	Cat# 9718; Clone 20E3; RRID:AB_2118009
PML	Millipore	Cat# 05-718; Clone 36.1-104; RRID:AB_11213854
SREBP-1	Santa Cruz	Cat# sc13551; Clone 2A4; RRID:AB_628282
TRF1	Abcam	Cat# ab192629; RRID:AB_3675954
UHRF1	Santa Cruz	Cat# sc373750; Clone M-8; RRID:AB_10947236
VINCULIN	Sigma-Aldrich	Cat# V9264; RRID:AB_10603627
ZSCAN4	Millipore	Cat# AB4340; RRID:AB_2827621
AF488 Anti-Chicken	Invitrogen	Cat# A-11039; RRID:AB_2534096
AF488 Anti-Rabbit	Invitrogen	Cat# A21206; RRID:AB_2535792
AF488 Anti-Rat	Invitrogen	Cat# A11006; RRID:AB_2534074
AF568 Anti-Mouse	Invitrogen	Cat# A21422; RRID:AB_2535844
AF568 Anti-Rabbit	Invitrogen	Cat# A11036; RRID:AB_10563566
AF633 Anti-Rabbit	Invitrogen	Cat# A21071; RRID:AB_141419
AF647 Anti-Rat	Invitrogen	Cat# A21247; RRID:AB_141778
Anti-Mouse IgG HRP-linked	Cell Signaling Technologies	Cat# 7076; RRID:AB_330924
Anti-Rabbit IgG HRP-linked	Cell Signaling Technologies	Cat# 7074; RRID:AB_2099233
Bacterial and virus strains		
pCAG-Zscan4c::eGFP	Wolf Reik's lab; Eckersley-Maslin et al.[48]	N/A
pCAG-3XFlag-Zscan4c	Taiping Chen's lab; Dan et al.[37]	N/A
Biological samples		
AlbuMAX™ I Lipid-Rich BSA	Gibco	11020021
Bovine gelatin solution	Sigma-Aldrich	G1393
Fetal bovine serum	Gibco	10270-106
Fibronectin	Merck	FC010
Knockout-serum replacement	Gibco	10828-028
Matrigel GFR Basement Membrane Matrix, LDEV-free	Corning	354230
Matrigel GFR Basement Membrane Matrix, LDEV-free	Corning	354231
Chemicals, peptides, and recombinant proteins		
B-27™ Supplement (50×), serum free	Gibco	17504044
D-Glucose-^{13}C-glucose	Sigma-Aldrich	389374
Human/Mouse/Rat Activin A Recombinant Protein	PeproTech	120-14
Human FGF-basic (FGF-2/bFGF)	PeproTech	100-18B

(*Continued on next page*)

Continued

REAGENT or RESOURCE	SOURCE	IDENTIFIER
KiCqStart SYBR Green qPCR ReadyMix	Sigma-Aldrich	KCQS02
Lipofectamine transfection reagent	Thermo Fisher Scientific	100014469
TelC-Cy3 probe	PNA Bio	F1002
Seahorse XF Assay Medium	Agilent	103575
Matrigel Cell Recovery solution	Corning	354253
N-2 Supplement (100×)	Gibco	17502048
Critical commercial assays		
Alkaline Phosphatase activity	Sigma-Aldrich	86R-1KT
Chromium Next GEM Single Cell 3′ GEM, Library & Gel Bead Kit v3.1	10× Genomics	PN-1000121
Clarity Western ECL Substrate	Bio-Rad	1705061
DNeasy Blood & Tissue Kit	Qiagen	69504
eBioscience AnnexinV-FITC Apoptosis Detection Kit	Thermo Fisher Scientific	BMS500Fi
NextSeq 500/550 High Output Kit v2.5	Illumina	20024906
MycoAlert Mycoplasma Detection Kit	Lonza	LT07-118
Pierce BCA Protein Assay Kit	Thermo Fisher Scientific	23225
QIAquick PCR Purification Kit	Qiagen	28106
Qubit Protein Assay Kit	Thermo Fisher Scientific	Q33211
Qubit 1× dsDNA HS assay kit	Thermo Fisher Scientific	Q33231
RNeasy Micro Kit	Qiagen	74004
RNeasy Mini Kit	Qiagen	74106
Seahorse Fluxpak	Agilent	102601-100
Deposited data		
ESC LD clones bulk RNA-seq data	This paper	GEO: GSE270063; SuperSeries GEO: GSE271241
ESC LD clones single-cell RNA-seq data	This paper	GEO: GSE253432; SuperSeries GEO: GSE271241
ESC-derived 3D spheroids bulk RNA-seq data	Mau et al.[28]	GEO: GSE165563
ESC and EpiLC bulk RNA-seq data	Buecker et al.[41]	GEO: GSE56138
ESC and EpiSC bulk RNA-seq data	Factor et al.[40]	GEO: GSE57409
Rex1-GFP ESC bulk RNA-seq data	Kalkan et al.[11]	ArrayExpress: E-MTAB-5305
Mouse embryo single-cell RNA-seq data	Deng et al.[69]	GEO: GSE45719
Experimental models: Cell lines		
E14 -Tg2a ESCs	ATCC	N/A
R1 ESCs	ATCC	N/A
CIDEA KO (R1) ESCs	Véronique Azuara's lab; Mau et al.[28]	N/A
CIDEA OE (E14) ESCs	Véronique Azuara's lab; Mau et al.[28]	N/A
ZSCAN4 OE (E14) ESCs	This study	N/A
Zscan4c:eGFP (E14) ESCs	This study	N/A
Rex1-GFP (E14) ESCs	Austin Smith's lab; Wray et al.[33]	N/A
Experimental models: Organisms/strains		
CD1 mouse	Charles River Laboratories, UK	N/A
Oligonucleotides		
RT qPCR primers; see Table S7		N/A
Telomere primers; see Table S7		N/A
Software and algorithms		
RStudio	https://posit.co/	N/A
GraphPad Prism	https://www.graphpad.com/	v10.0.2

(*Continued on next page*)

Continued

REAGENT or RESOURCE	SOURCE	IDENTIFIER
ImageJ/Fiji	Schindelin et al.[98]; https://imagej.net/software/fiji/	v1.53p
FlowJo	https://www.flowjo.com/	v10.7.1
Cell Profiler	Stirling et al.[99]	v4.2.1/v4.2.0
Gavin3	Behrends et al.[100]	beta 0.81
Lipid Data Analyzer	Hartler et al.[101]	v2.7.0_2019
MaxQuant software	Cox and Mann[102]; https://www.maxquant.org/	v1.5.1.0
Perseus	Tyanova et al.[103]; https://maxquant.net/perseus/	V1.5.0.15

EXPERIMENTAL MODEL AND STUDY PARTICIPANT DETAILS

Cell culture

Mouse ESCs were obtained from The Global Bioresource Center, ATCC (www.atcc.org). These cell lines were not further authenticated after purchase. They were maintained at 37°C, 5% CO_2 and routinely tested negative for mycoplasma contamination. For FBS/LIF conditions, ESCs were cultured on 0.1% gelatin-coated (Sigma Aldrich, G1393) culture plates in GMEM-BHK12 basal medium (Gibco, 21710-025) supplemented with 10% fetal bovine serum (FBS) (Gibco, 10270-106), Leukemia Inhibitory Factor (LIF) (made in-house), 0.1 mM β-mercaptoethanol (Gibco, 31350010), 0.25% (w/v) sodium bicarbonate (Gibco, 25080094), 1 mM sodium pyruvate (Gibco, 11360070), 0.1 mM non-essential amino acids (Gibco, 11140050), 2 mM L-glutamine (Gibco, 25030149), and 25 U/mL penicillin/streptomycin (Gibco, 11548876). For 2i/LIF conditions, ESCs were cultured on 0.2% gelatin-coated culture plates in DMEM F12:Neurobasal (vol. ratio 1:1) medium (Gibco, 11320033 and 21103049) supplemented with N2 (Gibco, 17502048), B27 (Gibco, 17504044), 0.1 mM β-mercaptoethanol, 2 mM L-glutamine, and 25 U/mL penicillin/streptomycin, with inhibitors CHIR99021 (3 μM) (Tocris, 4423), PD0325901 (1 μM) (Tocris, 4192) and LIF. For Knockout serum replacement (KSR) (Gibco, 10828-028) or AlbuMAX (Thermo Fisher, 11020021) treatment, the day after cells were seeded in FBS/LIF conditions, media was replenished with FBS replaced by either 15% KSR or 10% FBS supplemented with 1% AlbuMAX.

Mouse embryos *in vitro* culture

All animal experiments were conducted under a UK Home Office Project Licence in accordance with the Animals (Scientific Procedures) Act 1986. The study received ethical approval from the Animal Welfare and Ethical Review Body (AWERB) at Imperial College London, and all procedures complied with institutional and national guidelines for animal welfare. 4–6-week-old female and 2–6-month-old male CD1 mice (Charles River UK) were housed under 12-h light:dark cycle and provided with *ad libitum* food and water in individually ventilated cages. Female mice were super-ovulated by intraperitoneal injection of 5 IU pregnant mare serum gonadotropin (PMSG; Folligon, MSD Animal Health), followed 46–48 h later by 5 IU human chorionic gonadotropin (hCG; Chorulon, MSD Animal Health). Females were placed with males immediately following hCG injection and checked for copulatory plugs the following morning. Embryonic day (E) 0.5 embryos were collected from plugged females ~24–25 h post hCG by flushing of dissected oviducts with M2 medium (Sigma-Aldrich, M7167). Collected embryos were washed through successive drops of M2 and KSOMaa (Sigma-Aldrich, MR-106-D) pre-equilibrated at 37°C, 5% CO_2, then cultured in KSOMaa at 37°C, 5% CO_2 until collection for immunofluorescence (see immunofluorescence and LD staining) at early 2-cell (~30–31 h post hCG), late 2-cell (~48 h post hCG), and morula (~72–74 h post hCG). For DGAT inhibitor embryo experiments, E2.5 embryos were collected from plugged females ~72–74 h post hCG by flushing of dissected uteri with M2 medium (Sigma-Aldrich, M7167). Collected embryos were washed through successive drops of M2 and KSOMaa (Sigma-Aldrich, MR-106-D) pre-equilibrated at 37°C, 5% CO_2. Following collection, embryos were cultured for 1 h in KSOMaa at 37°C, 5% CO_2 before either fixation (see immunofluorescence and LD staining) or transfer to KSOMaa containing either DMSO (2% v/v as vehicle control) or DGAT1/2i (25 or 50 μM each of two inhibitors; T863 for DGAT1 (Sigma-Aldrich, SML0539) and PF06424439 for DGAT2 (Tocris, 6348) and cultured for a further 24 h, before fixation and processing for immunofluorescence and LD staining. The sex of embryos analyzed in this study was not determined and therefore not considered in the analysis.

METHOD DETAILS

Isolation of lipid droplet ESCs clones

E14 ESCs were plated at low density (1×10^4 cells in a 10 cm dish) in FBS/LIF medium. The presence of relatively large LDs (≥1 μm in diameter) in cultured ESCs could be visualized using phase-contrast microscopy, taking advantage of their spherical morphology

and distinct refractive index relative to the surrounding cytoplasm. Individual ESC colonies were isolated based on the abundance or absence of round, bright structures consistent with enlarged LDs. Selected clones were subsequently expanded in standard FBS/LIF medium and frozen at early passages. The LD phenotype of each clone was later confirmed by confocal microscopy using BODIPY 493/503 staining (see immunofluorescence and LD staining). Analysis over multiple passages demonstrated stable maintenance of the LD phenotype during prolonged culture.

Proliferation and self-renewal assays

To assess proliferation of ESC cultures, cells were seeded at 5×10^5 cells per well. After 48 h, cells were dissociated, counted and 5×10^5 cells were re-plated. This was repeated for 7 passages, and the growth curve was determined. To assess self-renewal capacity, alkaline phosphatase (AP) activity was measured using an AP staining kit (Sigma-Aldrich, 86R-1KT). ESCs were plated at 1×10^3 cells/mL, with medium replenished daily. Cells were grown for 7 days and stained according to the manufacturer's instructions. Stained colonies were counted and scored as undifferentiated, mixed, and differentiated. At least 30 colonies were counted per sample.

Embryoid bodies (EBs)

ESCs were counted and seeded in ultra-low suspension plates (Corning), at 2×10^5 cells/plate in 4 mL EB differentiation media (routine GMEM-BHK21 supplemented media with 5% FBS, and no LIF) per well; half the media was replenished every day. On indicated days (days 3, 6, and 9) post induction of differentiation, EBs were collected, lysed and RNA was extracted.

ESC-to-EpiLC conversion

For Epiblast-Like Cells (EpiLC) transient conversion, 2i/LIF ESCs were seeded on Fibronectin (Merck, FC010) coated plates in DMEM F12: Neurobasal (vol. ratio 1:1) medium supplemented with N2, B27, β-mercaptoethanol, L-glutamine, penicillin/streptomycin, 12 ng/mL FGF2 (PeproTech, 100-18B), 20 ng/mL Activin A (PeproTech, 120-14) and 1% KSR, and subsequently collected at 24 h, 48 h, and 72 h after seeding and EpiLC induction.

3D spheroid differentiation

In vitro differentiation of 3D spheroids was carried out as previously described for imaging and molecular analyses.[6,18] Prior to setting up the experiment, ESCs were grown in routine culture. At 60% confluency, cells were then counted, and the required cell volume was washed in ice-cold phosphate-buffered saline (PBS). For imaging experiments, cells were resuspended in ice-cold Matrigel (Corning, 354230) by pipetting to a single cell suspension, at a density of 1500 cells/μL. 25 μL of this cell suspension was plated into an 8-well chamber slide and allowed to set at 37°C for 10 min. Pre-warmed differentiation medium (routine GMEM-BHK21 supplemented media with 15% FBS, and no LIF) was then added to the wells. Cells were subsequently fixed 24 h or 48 h after plating. For molecular analyses, plates were coated with ice-cold Matrigel to completely cover the well and allowed to set for 20 min at 37°C. For these experiments, cells were plated at a density of 5×10^4 cells/cm^2 in differentiation medium, supplemented with 5% Matrigel. Cells were collected at 24 h or 48 h after plating using Cell Recovery Solution (Corning, 354253) and cold PBS.

Transfection

Cells were plated in a 6-well plate at a density of 2×10^5 cells/well in routine medium. The next day, transfection medium was prepared consisting of 100 μL OptiMEM, 1 μg of plasmid DNA, and 1 μL of Lipofectamine 2000 (Thermo Fisher, 100014469). This complex was left at room temperature for 10 min. The plate was replenished with fresh 1.5 mL routine medium, followed by the addition of 100 μL of the transfection medium and left overnight. The next day, medium was replaced with medium containing the appropriate antibiotic for selection. For stable cell lines, antibiotic treatment was carried out for 10 days.

Immunofluorescence and LD staining

Cells were plated on coverslips coated with 0.2% gelatin. For immunofluorescence, samples were washed and fixed in 4% paraformaldehyde (PFA; Sigma-Aldrich, P6148) for 10 min (self-renewal) or 20 min (ESC spheroids) at room temperature. Fixed samples were washed twice with PBS, followed by combined blocking and permeabilizing with 0.3% Triton X-100 (Sigma-Aldrich, ×100) in blocking buffer (3% bovine serum albumin (BSA; VWR, 422371×) in PBS) for 25 min at room temperature. The samples were then washed with PBS twice and incubated at 4°C overnight with the primary antibody in blocking buffer. The next day samples were washed twice and incubated with the secondary antibody, in blocking buffer, for 1 h at room temperature. For staining of F-ACTIN, phalloidin (0.5 mg/mL; Sigma-Aldrich, P1951) was added to the secondary antibody mix and the incubation was carried out overnight at 4°C. All antibodies and dilutions are listed in Table S6.

For LD staining, cells were plated at 2×10^5 cells/coverslip on 0.2% gelatin-coated coverslips. Treatments (DEUP 100 μM (Sigma Aldrich, D7692), ATGListatin 25 μM (Sigma Aldrich, SML1075)) were started 24 h after seeding for the indicated period, after which samples were fixed. Coverslips were washed and incubated with BODIPY 493/503 (5 μg/mL in PBS; Invitrogen, D3922) for 25 min at room temperature.

For nuclei staining, samples were washed and then incubated with DAPI (1 μg/mL in PBS; Sigma-Aldrich, D9542) for 10 min at room temperature. Samples were then mounted in ProLong Gold mounting agent (self-renewing ESCs) on slides or in 90% glycerol (ESC

spheroids) for confocal microscopy. Confocal images were acquired at 1 μm z sections, using a Leica SP5 microscope with a 63× oil immersion objective.

For single cell staining (e.g., Figure S1C), 30 min prior to fixation, samples were detached by trypsinization and re-seeded at a density of 1×10^5 cells per well onto Falcon 8-well chambered cell culture slides (Corning, 10364551), which had been pre-coated with 0.2% Matrigel. Cells were allowed to settle for 1 h to ensure proper adherence. Subsequent fixation and immunostaining were carried out as previously described.

DAPI linescan analysis was performed as previously described.[52,53] ESCs were plated on coverslips in routine FBS/LIF culture conditions and fixed at 50% confluency. Coverslips were stained for DAPI and mounted on slides. Images were collected on a Leica SP5 confocal microscope with a 63× oil immersion objective. Low laser power of the 405 nm laser was used to prevent saturation and ensure distinct heterochromatin foci could be identified.

For embryos, samples were fixed in 4% PFA in PBS for 20 min, washed 3 times for 10 min in PBS-PVA (0.1% PVA (Sigma-Aldrich, P8136-250G) in PBS). For staining of ZSCAN4 in 2-cell and morula embryos (Figure S5C), samples were permeabilized in 0.5% Triton X-100 in PBS for 30 min and blocked in 5% BSA in PBS for 1 h. Samples were incubated in primary antibody (1:100) in 5% BSA overnight at 4°C. The following day, samples were washed 3 times for 5 min in PBS-PVA and incubated with secondary antibody (1:200) in 5% BSA for 1 h. Samples were washed 3 times for 5 min in PBS-PVA and mounted in Vectashield with DAPI (2BScientific, H-1200). For staining of ZSCAN4, BODIPY 493/503, and F-ACTIN in morula and blastocyst embryos (Figures S5D and S5H), samples were permeabilized in saponin-BSA for 1 h and blocked in 0.3% BSA-PBS for 1 h. Samples were incubated in primary antibody (1:100) in saponin-BSA overnight at 4°C. The following day, samples were washed 3 times for 10 min in PBS-PVA and incubated with secondary antibody (1:200) in saponin-BSA for 2 h. Samples were washed once with PBS-PVA and incubated for 30 min in PBS-PVA containing BODIPY493/503 (5 mg/mL), DAPI (5 μg/mL) and Phalloidin-iFluor 647 (1:250; Abcam, ab176759). Samples were washed 3 times for 10 min in PBS-PVA, and mounted in Vectashield (2BScientific, H-1000). Confocal images were acquired at 1 μm z sections encompassing the entire embryo, using a Leica Stellaris microscope with a 40× oil immersion objective.

RNA extraction and RT-qPCR

RNA extraction was carried out using the RNeasy Mini kit (Qiagen, 74106) as per the manufacturer's instructions. For reverse transcription (RT), 0.5–1 μg of RNA was mixed with 1 μL of oligo-dT and 1 μL of dNTPs and then diluted with nuclease-free water up to 11 μL. Samples were incubated at 65°C for 5 min. Samples were then cooled on ice for 1 min. To each sample, 1 μL of the enzyme SuperScriptIII reverse transcriptase (Invitrogen, 18080044), 1 μL of RNase inhibitor RNaseOut (Invitrogen, 10777019), 1 μL of supplied DL-dithiothreitol (DTT) and 4 μL of the supplied reaction buffer was added. The mixture was incubated at 50°C for 60 min, followed by incubation at 70°C for 15 min. The resultant cDNA was then diluted to a concentration of 5 ng/μL. This cDNA was then used for quantitative real-time PCR (PCR) or RT-qPCR using the StepOnePlus Real-Time PCR System (Applied Biosystems). All reactions were run with technical replicates in the same plate. The PCR program was as follows: 95°C for 15 min, followed by 45 cycles at 94°C for 15 s, 60°C for 30 s and 72°C for 30 s. For analysis, Ct values of analyzed genes were normalized to the average of Ct values of the two housekeeping genes *L19/Rpl19* and *S17/Rps17* (see Table S7 for primers).

RNA sequencing

Library preparation and sequencing was carried out on extracted RNA samples by Source Bioscience (UK) using Illumina HiSeq (2×150 bp) to a depth of 30 million reads. Raw FASTQ data were provided, and an initial quality check was performed using FastQC (Simon Andrews, Babraham Institute, Cambridge). The raw data were trimmed using Trimmomatic-0.33[104] to remove Illumina adaptors and low quality bases (<15). Resulting trimmed sequences were mapped to the mouse reference transcriptome mm10 (obtained from Ensembl) and quantified simultaneously by Kallisto (v0.43.1).[105] Subsequent analysis was carried out in R/Bioconductor. Differential expression analysis was carried out using DESeq2 (v1.22.2),[106] with lowly expressed transcripts filtered out (counts per million <2 across more than 3 samples). Differentially expressed genes with a log2 fold-change > 1 and an adjusted p value < 0.05 (following FDR correction) were used for subsequent over-representation analysis (ORA). WebGestalt 2019[107] was used for the ORA, using Benjamini-Hochberg (BH) as a method to control for false discovery rate (FDR) with FDR < 0.05 as a cutoff. Three databases were used: Reactome,[108] WikiPathways,[109] and Panther.[110] Complete list of pathways from the ORA are listed in Table S1.

Single-cell RNA-sequencing

Cells were cultured in FBS/LIF conditions as previously described. All cultures were passaged simultaneously at similar seeding density and grown for 72 h before being processed on a 10× Genomics platform. For harvesting, cells were washed with DPBS and dissociated with 0.05% Trypsin-EDTA (Thermo Fisher, 25300054) for 5 min at 37°C in a humidified incubator. Dissociated cells were collected in 8 mL pre-warmed culture medium and centrifuged at $300 \times g$ for 5 min. Cells were resuspended in pre-warmed culture medium and filtered through a 70 μm cell strainer. Filtered cells were centrifuged at $300 \times g$ for 5 min and washed once with DPBS-BSA (DPBS with 0.04% BSA). Washed cells were resuspended in DPBS-BSA and filtered through a 40 μm cell strainer to obtain single cell suspensions. During further processing cells were kept on ice. The cell concentrations of the single cell suspensions were determined using a hemocytometer and adjusted to 1×10^6 cells/mL using DPBS-BSA. Single cell RNA-seq libraries were prepared from the single cell suspensions using a 10× Genomics Chromium Next GEM Single Cell 3′ Reagent Kit and 10× Chromium

single-cell platform according to the manufacturer's instructions (Doc. No. CG000204, revision B to C). DNA concentrations were assessed after cDNA amplification using a Qubit 1× dsDNA HS assay kit (Invitrogen, Q33231) and spectrophotometer (DeNovix ds-11). The DNA concentrations of the final libraries were determined in a similar fashion. The peak size distributions of the final libraries were measured before pooling using a 2100 Bioanalyzer (Agilent) in combination with high sensitivity DNA Chips and Reagents (Agilent, 5067-4626). The final library pools were sequenced on a NextSeq 500 (Illumina) sequencing instrument using a NextSeq 500/550 High Output 75-cycli kit (Illumina) with the following run type: 26bp read-1, 56bp read-2 and an 8bp index.

The sequencing data were processed and mapped against the 10× Genomics pre-built mouse reference transcriptome (mm10-2020-A) using 10× Genomics Cell Ranger (v6.1.2). The resulting raw count matrices were further analyzed in R. Briefly, the DropletUtils package (v1.16.0)[111] was used to perform barcode ranking (DropletUtils::barcodeRanks with 'lower = 2500' and 'fit.bounds = 8000 - ∞') and filter out barcodes of empty droplets (DropletUtils::emptyDrops with 'lower = 7000'). The retained barcodes were filtered using Seurat (v4.3.0.1)[112] (with 2100–3000 < detected genes <9000 and raw transcript counts >7500). Barcodes with more than 15% mitochondrial counts were removed. Additional filtering was performed with DropletQC (v0.0.0.9000)[113] that identifies (and removes) damaged cells based on total RNA content and fraction of unspliced nuclear RNA (DropletQC::identify_damaged_cells with 'nf_sep = 0.10' and 'umi_sep_perc = 50'). Following quality control and data filtering, between 2,465 and 3,796 single-cell transcriptomes were obtained per culture. The count matrices were normalized individually using Seurat::SCTransform while regressing for the percentage of nuclear RNA and percentage of ribosomal protein counts. The count matrices were then concatenated with Seurat::merge. Initial downstream analyses included graph-based cell clustering using Seurat::FindClusters and Seurat::RunUMAP after determining a suitable clustering resolution using Clustree (v0.4.4).[114] Normalized (and scaled) expression values computed with Seurat::SCTransform were used to generate violin and dot plots, unless stated otherwise. Gene signatures were calculated as module scores from Seurat::SCTransform-processed expression data using UCell (v2.0.1).[115] The gene panels for calculating signature scores were: Naive score - *Esrrb*, *Klf2*, *Klf4*, *Klf5*, *Nr0b1*, *Nr5a2*, *Tbx3*, *Tcl1*, *Tfcp2l1*, *Zfp42/Rex1*; Formative/Primed score - *Dnmt3a*, *Dnmt3b*, *Fgf5*, *Gata6*, *Krt18*, *Lef1*, *Lefty1*, *Lefty2*, *Oct6/Pou3f1*, *Otx2*, *Sox17*, *Wnt8a*, *Zfp281*; Lipid score - *Acaca*, *Acly*, *Acsl1*, *Agpat2*, *Agpat3*, *Agpat4*, *Dgat1*, *Dgat2*, *Fasn*, *Gpat4*, *Mgat1*, *Mogat2*, *Scd1*, *Scd2*, *Srebf1*, *Srebf2*; DNA damage response score - *Atm*, *Apex1*, *Atr*, *Brca1*, *Brca2*, *Chek1*, *Chek2*, *Dclre1c*, *Ercc1*, *Ercc4*, *Ercc5*, *Exo1*, *Gtf2h1*, *H2ax/H2afx*, *Lig1*, *Lig3*, *Lig4*, *Mre11a*, *Msh2*, *Msh3*, *Msh6*, *Nbn*, *Nhej1*, *Parp1*, *Pms1*, *Pms2*, *Polb*, *Poll*, *Polm*, *Prkdc*, *Rbbp8*, *Rad23b*, *Rad50*, *Rad51*, *Xpa*, *Xrcc1*, *Xrcc4*, *Xrcc5*, *Xrcc6*. Correlation heatmaps of gene signatures were generated using the ggcorplot package (v0.1.4.1). The pseudotime trajectory was calculated using Monocle3 (v1.3.4). Briefly, a CDS object was generated from the merged Seurat object as input for Monocle3.[116] The Seurat-based UMAP coordinates were extracted and Monocle3::plot_cells function was used to recreate the UMAP clustering. The trajectory was then learned and overlaid using Monocle3::learn_graph (with 'use_partitions = false'). After learning the trajectory, cells were ordered in pseudotime after setting the root point (i.e., pseudotime = 0) to cluster "Z", enriched with Zscan4-expressing cells, to follow their trajectory in pseudotime. For *in vivo* embryo single-cell RNA-seq data analysis, processed published data from GSE45719[69] (see Table S5) was used to examine the *Zscan4*-signature.

Dimensionality reduction and clustering analysis

Accession numbers of published datasets and newly generated datasets used in this analysis are listed in Table S5. Expression matrices containing raw count data were generated from FASTQ files, using Kallisto[105] (as described above). To minimize batch effects across the different studies, the count data from each of the datasets was processed using ComBat.[117] These were then log transformed and filtered to identify genes with a large variance across the samples, by setting thresholds for the minimum and maximum expression values of these genes. This resulted in a set of 6973 genes, which was further reduced to 2000 genes by iteratively optimizing the projection and feature (i.e., gene) selection using a Gaussian process regression model[39] in MATLAB. This low dimensionality clustering algorithm was used to generate the differentiation trajectory.

Signature scoring of Rex-1/Zfp42 GFP ESCs upon 2i/LIF withdrawal

Processed data from E-MTAB-5305 was used for this analysis, as listed in Table S5.[11] Briefly, count matrices (expression values as transcripts per million; TPM) were generated by mapping raw reads from the FASTQ files to the mm39 reference genome using Seq2Science[118] with default RNA-seq settings. Further data processing was conducted in R. Gene signature scores were computed using UCell (v2.0.1) from the TPM expression values, following a similar approach as UCell-based module scores derived from single cell RNA-seq data. The gene panels for naive, formative/primed, and lipid scores were identical to those previously described. Additionally, a "Zscan4 score" was derived from the expression values of genes linked to *Zscan4*-expression events; *Zscan4c*, *Zscan4d*, *Nelfa*, *Eif1ad8/Gm8300*, *Tmem92*, *Usp17le*, *Tcstv3*, matching the gene panel used for 'Z4 events' in the single cell RNA-seq dot plot. Scores were normalized from 0 to the maximum value and visualized as a heatmap.

Western blot

Samples were collected and lysed in in-house Radio-Immunoprecipitation Assay (RIPA) buffer, supplemented with protease and phosphatase inhibitors, for protein extraction. Protein concentration was determined by BCA assay (Thermo Fisher, 23225) as per the manufacturer's instruction. 10–20 μg protein was loaded with Laemmli buffer (Bio-Rad, 161–0747) into SDS-PAGE gels (8–13% running gel/4% stacking gel) with pre-stained protein ladder. After SDS-PAGE, proteins were transferred to a methanol-activated PVDF Immobilon-FL membrane (Millipore, IPL00010) by semi-dry or wet transfer protocol. Blocking was carried out in 5%

milk in Tris-buffered saline with 0.1% Tween 20 (TBST) for 1 h at room temperature and then incubated in primary antibody solution (in 5% milk or BSA) overnight at 4°C. The membrane was washed in TBST, followed by incubation with a horseradish peroxidase (HRP)-conjugated secondary antibody for 1 h at room temperature. The membrane was washed in TBST, developed with Immobilon Forte HRP substrate (Bio-Rad, 1705061) and imaged by ImageQuant LAS4000 imager or exposed to X-ray film. Quantification was done in Fiji/ImageJ. All antibodies and dilution factors used can be found in Table S6.

Flow cytometry

Cells were grown in the indicated culture conditions (15% KSR, 1% AlbuMAX, DGAT1/2i (25 μM each), 2-DG (10 mM; Sigma Aldrich, D6134), DCA (10 mM; Sigma Aldrich, 347795), citrate (4 mM; Sigma Aldrich, C8532), or α-KG (4 mM; Sigma Aldrich, 349631)) for 24–72 h, as specified. After treatments, cells were dissociated with trypsin and collected in media. For E14 ZE3-GFP reporter cells, cell pellets were directly resuspended in flow buffer (1 mM EDTA, 25 mM HEPES pH 7.0, 1% FBS). For ROS measurements, cells were stained with DCFDA (20 μM; Sigma-Aldrich, D8663) according to the manufacturer's instructions in PBS. After washing, cells were resuspended in flow buffer. All experiments were carried out with an unstained control. For apoptosis measurements, eBioscience AnnexinV-FITC Apoptosis Detection Kit (Thermo Fisher Scientific, BMS500Fi) was used as per the manufacturer's instructions. Flow cytometry experiments were carried out with BD FACSCalibur (Cell Quest software) or BD LSRII (FACSDiva software). Excitation lasers and emission filters were chosen as per manufacturer's specifications and available lasers. Results were analyzed in FlowJo (version 10.7.1).

Seahorse assays

Seahorse assays for OCR and ECAR measurements were performed on an Agilent XFe24 (LD clones) or XFe96 analyzer (CIDEA OE, ZSCAN4 OE). Cartridges were prepared as per the manufacturer's instructions. Optimal cell density was determined for each plate (24-well or 96-well). Growth curve was calculated for each cell line prior to all experiments to ensure similar growth rates. For initial normalization, cell number was calculated using DAPI fluorescence in the Seahorse plate. The cellular oxygen consumption rate (OCR) was measured via the Mitostress assay, with 3–5 cycles of measurement for each parameter. Basal respiration was measured first, prior to any treatment. To measure ATP-linked respiration, cells were treated acutely with oligomycin (1.5 μM; Sigma-Aldrich, O4876). This was followed by carbonyl cyanide 4-(trifluoromethoxy) phenylhydrazone (FCCP) (0.4 μM; Sigma-Aldrich, C2920) to measure maximum cellular respiration. Finally, antimycinA (2 μM; Sigma-Aldrich, A8674) and rotenone (2 μM, Sigma-Aldrich, R8875) were added in combination to determine non-mitochondrial respiration. The cellular extracellular acidification rate (ECAR) was measured via the Glycolysis stress assay, with cells starved of glucose prior to the assay. 3–5 cycles of measurement were performed for each parameter, starting with basal ECAR. Glucose (2.5 mM; Gibco, A2494001) was then added to the cells to determine glycolytic flux, followed by oligomycin (2.5 μM) to measure maximum glycolytic capacity. Finally, 2-DG (50 mM) was used to determine the non-glycolytic acidification rate. For substrate utilization assays, cells were treated with specified inhibitors including UK5099 (20 μM; Tocris, 4186), BPTES (10 μM; Tocris, 5301), or Etomoxir (40 μM, Sigma-Aldrich, E1905) for 1 h prior to the assay, with continued treatment during the assay. This was carried out in conjunction with the Mitostress assay. All assays were run with 3–5 technical replicates per plate.

Metabolomics profiling

ESCs were plated at a density of 5×10^5 cells/well in a 6-well plate, with two wells for each sample. After 16 h in culture, the routine medium was changed to DMEM supplemented with 10% dialyzed FBS for 24 h. The media was aspirated, and the cells washed with cold (4°C) Ringer's buffer, which was aspirated before addition of 750 μL of cold (−70°C) methanol. The methanol-quenched cells were then scraped from the well and the sample was transferred to a clean tube. To increase metabolite recovery, each well was washed with a further 750 μL of cold methanol and pooled with the first sample. The methanol-quenched samples were then dried in a rotary evaporator under reduced pressure. The dried cell pellets were frozen for subsequent metabolite extraction. Metabolites were extracted from the samples using a dual phase extraction method. To the frozen pellet, 300 μL of chloroform/methanol (2:1) was added and the samples vortexed for 30 s. An addition of 300 μL of HPLC-grade water was made and samples were vortexed for a further 30 s and centrifuged at 18,400 × g for 10 min. The upper aqueous and lower organic layers were transferred to separate silanized GC-MS vials. The extraction was repeated to maximize metabolite recovery. The organic fractions were dried under a stream of inert gas and stored at −80°C, while the aqueous fractions were freeze-dried and stored at −80°C. To each sample, 10 μL of myristic acid-d27 (1.5 mg/mL) was added as an internal standard, following which the samples were dried in a centrifugal evaporator. The dried aqueous samples were methoximated using 20 μL of methoxyamine (20 mg/mL) in anhydrous pyridine at 37°C for 90 min. This was followed by silylation with 80 μL of N-methyl-N-(trimethylsilyl) trifluoroacetamide (MSTFA) at 37°C for 30 min. Following derivatization, 2-fluorobiphenyl in anhydrous pyridine (10 μL, 1 mM) was added to the samples as an injection standard and the samples were vortexed, centrifuged for 5 min and transferred to clean silanized vials before GC-MS analysis. GC-MS analysis was performed as described below.

The dried apolar samples were reconstituted with a solution of anhydrous methanol/toluene (333 μL, 1:1 v/v), treated with 0.5 M sodium methoxide (167 μL) and incubated at room temperature for 1 h. The reaction was stopped by the addition of 1 M NaCl (500 μL) and concentrated HCl (25 μL). The apolar fraction was extracted with two volumes of hexane (500 μL), and the combined apolar layers were dried under inert gas. Samples were then silylated by reconstituting with 40 μL acetonitrile and treating with 40 μL

N-*tert*-butyldimethylsilyl-N-methyltrifluoroacetamide (with 1% tert-butyldimethyl-chlorosilane) (Sigma-Aldrich, 394882) and incubating at 70°C for 60 min. Following derivatization, 2-fluorobiphenyl in anhydrous pyridine (10 μL, 1 mM) was added to the samples as an injection standard and the samples were vortexed, centrifuged for 5 min and transferred to clean silanized vials before GC-MS analysis. GC-MS analysis was performed as described below.

$^{13}C_6$-glucose tracing experiment

ESCs were plated at a density of 2.5×10^5 cells/well in a 6-well plate. After 16 h in culture, the routine medium was changed to DMEM supplemented with 10% dialyzed FBS and 5.6 mM unlabeled $^{12}C_6$-glucose (Sigma-Aldrich, G8270) for 1 h for equilibration. The media was then changed to DMEM with 10% dialyzed FBS and 5.6 mM $^{13}C_6$-glucose (Sigma-Aldrich, 389374), and the culture was maintained for 72 h with no change of media. The cells were then washed, quenched and collected as described above for the unlabeled metabolomics study. Intracellular apolar metabolites (i.e., lipids) were extracted from six independent cultures of each clone analyzed. To each sample, 10 μL of myristic acid-d27 (1.5 mg/mL) was added as an internal standard, following which the samples were dried in a centrifugal evaporator. Fatty Acid Methyl Esters (FAME) were generated by derivatization with sodium methoxide (as above), which *trans*-esterifies all lipid bound fatty acids to a methyl ester. GC-MS was then performed as described below.

Gas chromatography-mass spectrometry (GC-MS)

The order of sample preparation and analysis on the GC-MS was randomized. The GC-MS analysis was performed using an Agilent Technology 7693 autosampler coupled to a 7980A GC system and a 5975 MSD mass spectrometer. 1 μl of prepared sample was introduced into an inert glass splitless liner by the 7693 autosampler injector and chromatographically separated on a 30 m DB-5MS capillary column in the 7980A GC oven using helium as the carrier gas. The metabolites were detected via the 5975 MSD mass spectrometer running in electron impact ionization mode. Metabolites were identified and assigned with in-house fragment/retention time databases or the Fiehn library in the deconvolution software AMDIS and individual peaks quantified using in-house MATLAB script based on the GAVIN3 software.[100] Mass isotopomers were quantified using in-house scripts (GAVIN) and the distributions were normalized so that the sum of the metabolite isotopomer abundances were equal to one and corrected for naturally occurring elemental isotopes based on previously described methods.[119]

Liquid chromatography-mass spectrometry (LC-MS)

LC-MS was performed as previously described.[120] Briefly, lipids were extracted from frozen cells pellets using the Folch extraction method with chloroform/methanol/water (2:1:1). Lipids were dried using a SpeedVac (Thermo Fisher Scientific) and resuspended in chloroform/methanol (1:1). This was then injected into a Shimadzu Prominence 20-AD system (Shimadzu) for chromatographic separation with Waters Acquity UPLC C4 (300 Å, 1.7 μm particle size) columns. Using a mobile phase of water (solvent A) and acetonitrile (ACN) (solvent B) with 0.025% formic acid, 7 μL of the samples were eluted from the columns at 45°C. The flow rate was maintained at 100 μL/min. Mass detection was carried out with an Orbitrap Elite mass spectrometer (Thermo Fisher Scientific), with an error cutoff of 5 parts per million (ppm). Source parameters for positive polarity: capillary temperature 275°C; source heater temperature 200°C; sheath gas 10 AU; aux gas 5 AU; sweep gas 5 AU. Source voltage was 3.8 kV. Full scan spectra in the range of m/z 340–1500 were acquired at a target resolution of 240,000 (FWHM at m/z 400). Xcalibur software (Thermo Fisher Scientific) was used for manual inspection of results, followed by data processing with Lipid Data Analyzer (LDA) 2.7.0_2019 software.[101]

DNA methylation via high-performance liquid chromatography-tandem mass spectrometry (HPLC-MS/MS)

DNA was isolated from cells using the PureLink Genomic DNA Mini Kit (Invitrogen, K182001) as per the manufacturer's instructions. The samples were diluted to a final DNA concentration of 100 ng/μL, in a minimum volume of 3 μL. The DNA was degraded into individual nucleosides using DNA Degradase Plus (Zymo Research, E2020). Individual nucleosides were measured using a high-performance liquid chromatography-tandem mass spectrometry (HPLC-MS/MS) system. Quantification was performed using a standard curve derived from calibration standards. The 5mC and 5hmC levels were calculated as a concentration percentage ratio of % 5-methyl-2′-deoxycytidine to 2′-deoxyguanosine (%mdC/dG) and % 5-hydroxymethyl-2′-deoxycytidine to 2′-deoxyguanosine (%5hmdC/dG) respectively.

Chromatin enrichment for proteomics (ChEP)

ChEP analysis was carried out as previously described.[46] Briefly, ESCs were grown in routine culture conditions, using T175 flasks. At least 3×10^6 cells were used per replicate. Cells in flasks were washed with PBS and incubated in 1% formaldehyde at 37°C for 10 min. Fixation was quenched using 0.25 M glycine at room temperature for 5 min. Cells were then washed with PBS twice and collected by scraping. Following centrifugation, cell pellets were frozen in liquid nitrogen. Cell pellets were lysed in lysis buffer, supplemented with protease inhibitors (Roche, 11697498001). The nuclei were pelleted via centrifugation and digested using lysis buffer containing 200 μg/mL RNase A (Thermo Fisher Scientific, EN0531). Centrifugation was repeated, and the nuclei were lysed in SDS buffer, with protease inhibitors, and urea buffer. The pellets were placed in storage buffer, supplemented with protease inhibitors, prior to sonication and centrifugation. The final supernatant, consisting of sonicated and cross-linked chromatin, was used to determine the protein yield via the Qubit Protein Assay kit (Invitrogen, Q33211). Cross-links were reversed with SDS-PAGE loading buffer. The protein mixtures were digested, desalted and LC-MS/MS was performed. MaxQuant software (v1.5.1.0)[102] was used for analysis

of MS data, with default settings to generate label-free quantification (LFQ) values for all samples. Perseus software (v1.5.0.15)[103] was used for downstream analysis. Proteins were omitted if flagged as 'potential contaminant', 'reverse hit', or 'only identified by site'. Proteins with less than two peptides were filtered out, and remaining LFQ values were log2 transformed. Proteins not detected in eight or more samples were excluded and remaining missing values were imputed from a normal distribution using Perseus' default settings (width = 0.3 and down-shift = 1.8). Fold changes and statistically different proteins were calculated for each comparison using a two-sample *t* test.

Telo-PCR

Genomic DNA was used to measure relative telomere length as previously described.[73] Briefly, genomic DNA was extracted from ESCs or spheroids using the DNeasy DNA extraction kit (Qiagen, 69504). qPCR was carried out using primers for either telomeric DNA or the single-copy acidic ribosomal phosphoprotein PO (*36B4/Rplp0*) gene (see Table S7). For each reaction 10 ng of DNA was used. Each PCR run also contained reactions, in triplicate, for a range of 3.75–60 ng of reference DNA (usually parental cell lines) for standard curve calculations. PCRs for telomeric DNA and single-copy genomic 36B4 were run separately, as described below. For telomeric DNA PCR, each reaction contained 12.5 μL of SYBR Green qPCR ReadyMix, 300 nM of each primer, and nuclease-free water to make a 25 μL reaction, with the required DNA volume. The PCR program was as follows: 95°C for 10 min, followed by 30 cycles of 95°C for 15 s and 56°C for 1 min. For 36B4 PCR, each reaction contained 12.5 μL of SYBR Green qPCR ReadyMix, 300 nM of the forward primer, 500 nM of the reverse primer, and nuclease-free water to make a 25 μL reaction with the required DNA volume. The PCR program was as follows: 95°C for 10 min, followed by 35 cycles of 95°C for 15 s, 52°C for 20 s and finally, 72°C for 30 s. To calculate relative telomere lengths, input amounts were determined using the standard curve. The ratio of relative input amount for telomeric DNA to 36B4 was then calculated and represented as average telomere length ratio across the samples.

C-circle amplification PCR

ALT-specific C-circles were measured as a readout of ALT activity as previously described.[77] Genomic DNA was extracted using the DNeasy DNA kit as per manufacturer's instructions. C-circle amplifications (CCA) were carried out for each sample using a thermocycler. For each reaction, 30 ng of DNA was used with ϕ29 DNA Polymerase (7.5 units; New England Biolabs, M0269), dNTPs (1 mM each), Tween 20 (0.1% v/v; Sigma Aldrich, P1379), DTT (1 mM), BSA (1 μg/mL; provided with enzyme), and ϕ29 buffer (provided with enzyme) in Tris buffer pH 7.6 (10 mM). A control reaction without ϕ29 DNA Polymerase was carried out for each sample. The amplification was performed as follows: 30°C for 4 h, followed by 70°C for 2 min, and stored at 4°C. CCA was then followed by a qPCR reaction using the primers (telomeric DNA and single-copy 36B4) for telomere length analysis in Table S7. Each reaction contained 5 μL of the CCA product, with 12.5 μL of SYBR Green qPCR ReadyMix, 500 nM of each primer, and nuclease-free water to make a 25 μL reaction. For telomeric DNA PCR, a standard curve was calculated using serial 3-fold dilutions to obtain the following concentrations (ng/μL) of parental cell line DNA: 3.2, 1.07, 0.36, 0.12, 0.04 and 0.013. The PCR program was as follows: 95°C for 15 min, followed by 30 cycles of 95°C for 7 s and 58°C for 10 s. For single-copy gene PCR a standard curve was calculated using serial 3-fold dilutions to obtain the following concentrations (ng/μL) of parental cell line DNA: 3.2, 1.6, 0.8, 0.4, 0.2 and 0.1. The PCR program was as follows: 95°C for 5 min, followed by 40 cycles of 95°C for 15 s and 58°C for 30 s. ALT-positive controls were always run in parallel (here an osteosarcoma cell line, U-2 OS, was used as recommended). For quantification, input DNA amounts were determined using the standard curve and normalized to 36B4 gene levels as described above. CCA levels were then determined by subtracting the amount of DNA of the respective control ϕ29-negative reactions and normalized to U-2 OS CCA levels. CCA-positive samples are those that show CCA level >1% of the CCA level for U-2 OS cells.

Metaphase preparation and quantitative FISH

ESCs were treated with colcemid (0.05 μg/mL; Roche, 10295892001) for 90 min under routine culture conditions. After this, cells were washed with PBS, and dissociated, and pelleted. Cell pellets were lysed with 8 mL of pre-warmed hypotonic solution (8 g/L sodium citrate; Sigma-Aldrich, C8532) added dropwise and then incubated at 37°C for 20 min. To this, 1 mL of cold fixative (ethanol:acetic acid/3:1) was added and centrifuged at 200 × g for 5 min. The supernatant was discarded, more fixative was added to the cell pellet dropwise, and tubes were centrifuged at 300 × g for 5 min; fixation was repeated. Lastly, 8 mL of fixative was added and left overnight at −20°C. The following day, slides were immersed in 100% ethanol. Cells were thawed at room temperature for at least 30 min prior to centrifugation at 300 × g for 5 min. Cell pellets were resuspended in 1 mL of fixative. A humid environment was created using wet paper towels under the slides. On each slide, 50 μL of cell suspension was dropped to allow for proper metaphase spreads. Slides were dried overnight at room temperature. To the pre-dried metaphase spreads, 35 μL of hybridization solution containing the TelC-probe (PNA Bio, USA, F1002) (1 nM probe in 70% w/v formamide, 20 mM Tris-Cl pH 7.4, 1% w/v BSA) was added per slide and denatured by incubation at 80°C for 3 min. This was followed by incubation at room temperature in the dark, for 2 h. Following incubation, the slides were washed successively with the two wash buffers. First, with wash buffer 1 (70% w/v formamide, 20 mM Tris-Cl pH 7.4), twice for 15 min each time, then with wash buffer 2 (70% w/v formamide, 150 mM NaCl, 0.05% v/v Tween 20), thrice for 5 min each time. The slides were then dehydrated with successive ethanol baths (70%, 80%, 90%, 100%) and then air dried in the dark. Coverslips were then mounted with DAPI (5 μg/mL), and the slides were sealed. Confocal images were acquired using a Leica SP5 microscope with a 63× glycerol immersion objective.

QUANTIFICATION AND STATISTICAL ANALYSIS

Image analysis

All image analysis was carried out using ImageJ/Fiji (v1.53p)[98] and CellProfiler (v4.2.1).[99] For BODIPY-based neutral lipid quantification in ESCs (Figures 1C, S1B, S1D, 5B, and 5F), custom macro scripts in ImageJ were used to quantify total area of BODIPY signal and total area of DAPI signal in a maximum z stack projection. For quantification of LDs per cell (Figures S1C and S4A), CellProfiler's 'propagation method' was used to determine cytoplasmic area around the nucleus. LDs were counted within this area using BODIPY signal within maximum z stack projections. For quantification of ZSCAN4-positive (Z4+) ESCs (Figures 4F, 5C, and 5G), wide-field images were taken and converted to grayscale using custom macros in ImageJ. Then number of cells were quantified in each channel using Fiji's 'Analyze Particles' plugin. For quantification of chromocenters using DAPI linescan analysis (Figures 4G and 4H), lines were drawn across an individual nucleus to intersect with the maximum number of DAPI foci (see Figure 4G insets). Intensity across the line was then measured using ImageJ/Fiji and the number of peaks was recorded. For quantification of OCT4 intensity (Figure S4P), GFP was used to identify ZSCAN4-positive or -negative status, and OCT4 intensity was quantified using custom CellProfiler pipelines. For telomere quantitative-FISH (Figures 6B and S6K), CellProfiler pipelines were created to split channels and convert to grayscale. TelC-Cy3 intensity (telomere foci) was quantified within DAPI regions at chromosomal ends, for signal normalization. For APB and DNA damage quantification, slices were extracted from 3D stacks and converted to grayscale using custom macros. These were then imported into CellProfiler to quantify foci signal within DAPI regions in each slice. Colocalized TRF1/PML (Figures S6L and S6M) or pH2AX/TRF1 (Figure S6C) foci were then counted within the nuclear regions in each. APBs were normalized to total number of PML foci.[121]

For embryo analysis (Figures 5N, 5O, and S5C–S5H), images were processed to single channel maximum projection or single-plane images using Fiji. Using DAPI and phalloidin staining, embryo morphology was manually scored as normal (morula or E3.5 blastocyst), abnormal, which included embryos with collapsed or multiple cavities, and embryos with apoptotic cells. Apoptotic cells had extremely high BODIPY signal therefore these embryos were excluded from further analyses. The number of BODIPY foci per embryo were identified in maximum projection images using CellProfiler (v4.2.0). ZSCAN4 staining intensity was quantified, using CellProfiler, in single z sections within segmented nuclei (see Figure S5G for overview of analysis pipeline). Several z sections $\geq$5 sections apart were analyzed per embryo to avoid double-sampling the same nucleus in different focal planes.

STATISTICAL ANALYSIS

Statistical analyses were performed using GraphPad Prism (v10.0.2) except for bulk/single-cell RNA-sequencing and ChEP data. Data are presented as mean ± standard error of mean (SEM), unless otherwise specified in the figure legends. Number of independent replicates are stated in the figure legends. Statistical tests used for each set of experiments are specified in the figure legends; in this study, data were compared using either a two-tailed paired or unpaired Welch's *t* test, or one- or two-way ANOVA with a post hoc test as specified in text. For quantitative analyses, including quantification of Z4+ ESCs, APB formation, and embryo analysis, normality was tested using D'Agostino and Pearson's normality test. For non-normally distributed data, the Kruskal-Wallis test with Dunn's multiple correction test was used. No statistical method was used to predetermine sample size of embryos.

Cell Reports, Volume *44*

Supplemental information

The exit of naive pluripotency contains a metabolism-induced checkpoint for telomere homeostasis

Roshni A. de Souza, David Barneda, Donja Karimlou, Nick G.P. Bovee, Yuhan Zheng, Eveline J.E.M. Kahlman, Clara Lopes Novo, James K. Ellis, Bryony J. Leeke, Songyang Li, Megha Prakash Bangalore, Zijing Liu, Bebiana C. Sousa, Andrea F. Lopez-Clavijo, Joop H. Jansen, Mauricio Barahona, Michelle Percharde, Hector C. Keun, Mark Christian, Hendrik Marks, and Véronique Azuara

FIGURE S1

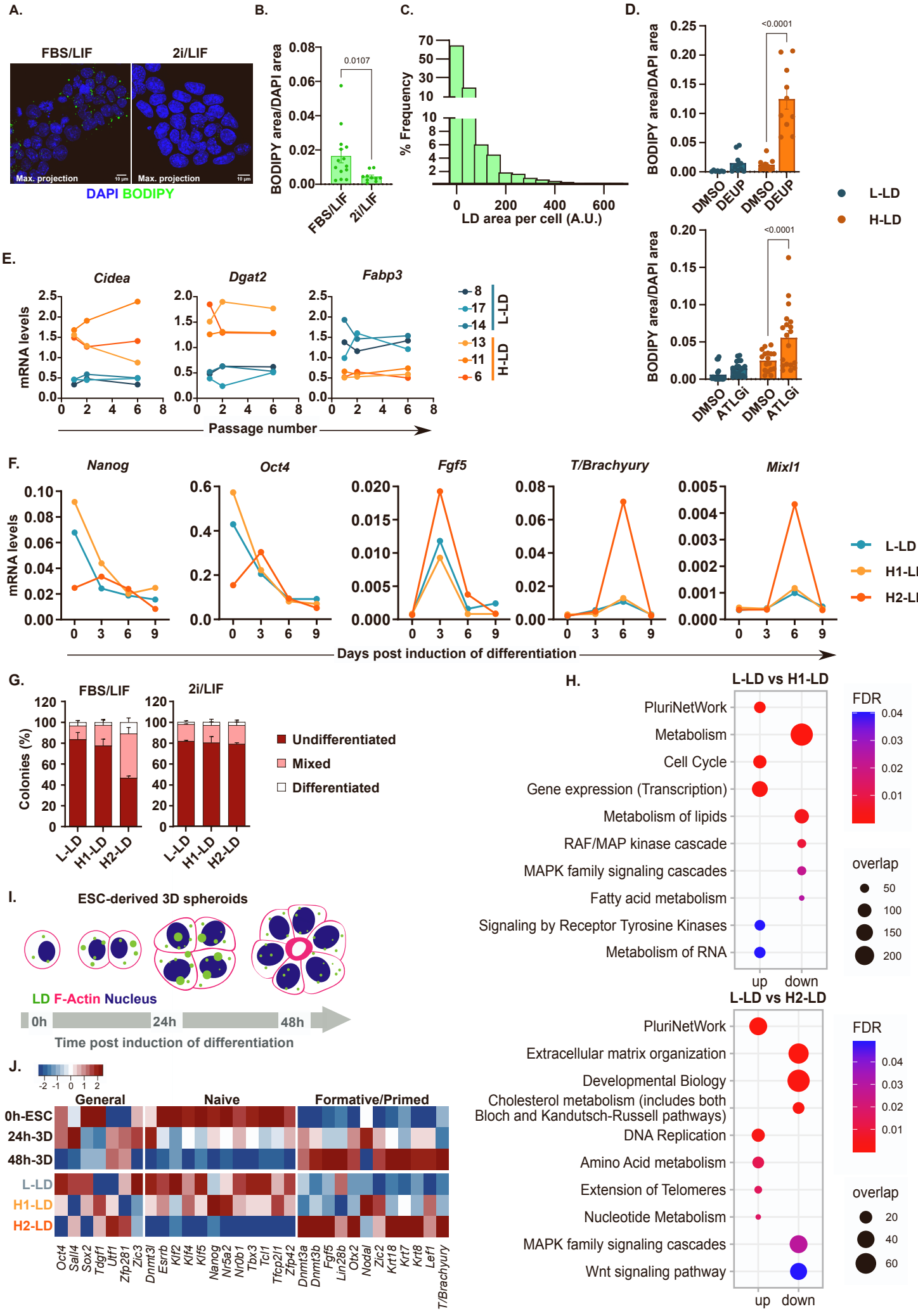
A.
FBS/LIF
2i/LIF
Max. projection
Max. projection
DAPI BODIPY
B.
BODIPY area/DAPI area
0.0107
FBS/LIF
2i/LIF
C.
% Frequency
LD area per cell (A.U.)
D.
BODIPY area/DAPI area
<0.0001
DMSO
DEUP
DMSO
DEUP
L-LD
H-LD
<0.0001
DMSO
ATLGi
DMSO
ATLGi
E.
Cidea
Dgat2
Fabp3
mRNA levels
Passage number
8
17
14
13
11
6
L-LD
H-LD
F.
Nanog
Oct4
Fgf5
T/Brachyury
Mixl1
mRNA levels
Days post induction of differentiation
L-LD
H1-LD
H2-LD
G.
FBS/LIF
2i/LIF
Colonies (%)
Undifferentiated
Mixed
Differentiated
L-LD
H1-LD
H2-LD
H.
L-LD vs H1-LD
PluriNetWork
Metabolism
Cell Cycle
Gene expression (Transcription)
Metabolism of lipids
RAF/MAP kinase cascade
MAPK family signaling cascades
Fatty acid metabolism
Signaling by Receptor Tyrosine Kinases
Metabolism of RNA
up
down
FDR
overlap
L-LD vs H2-LD
PluriNetWork
Extracellular matrix organization
Developmental Biology
Cholesterol metabolism (includes both Bloch and Kandutsch-Russell pathways)
DNA Replication
Amino Acid metabolism
Extension of Telomeres
Nucleotide Metabolism
MAPK family signaling cascades
Wnt signaling pathway
up
down
FDR
overlap
I.
ESC-derived 3D spheroids
LD F-Actin Nucleus
0h
24h
48h
Time post induction of differentiation
J.
General
Naive
Formative/Primed
0h-ESC
24h-3D
48h-3D
L-LD
H1-LD
H2-LD
Oct4
Sall4
Sox2
Tdgf1
Utf1
Zfp281
Zic3
Dnmt3l
Esrrb
Klf2
Klf4
Klf5
Nanog
Nr5a2
Nr0b1
Tbx3
Tcl1
Tfcp2l1
Zfp42
Dnmt3a
Dnmt3b
Fgf5
Lin28b
Otx2
Nodal
Zic2
Krt18
Krt7
Krt8
Lef1
T/Brachyury

Figure S1: L-LD and H-LD phenotypes correspond to distinct metabolic and pluripotent states in ESCs, related to Figure 1.

(A) Representative images of BODIPY 493/503-stained LDs (green) and DAPI-stained nuclei (blue) in E14-ESCs cultured in FBS/LIF or 2i/LIF. Images shown are z-stack maximum projections, scale bars, 10 μm.
(B) Quantification of BODIPY signal, normalized to DAPI (area). For each culture, n≥5 colonies were imaged in independent experiments (n=2). Error bars, mean ± SEM; two-tailed t-test with Welch's correction.
(C) Frequency distribution of LD area per cell in ESCs grown in FBS/LIF (n=1318 cells across 5 independent experiments).
(D) Quantification of BODIPY signal, normalized to DAPI (area), in L-LD (8) and H-LD (11) clones, upon 24-hour treatment with inhibitors suppressing LD decay by lipolysis (DEUP, 100 μM; ATGListatin, 25 μM). Error bars, mean ± SEM; Fisher's two-way ANOVA (n>10 colonies across 3 independent experiments).
(E) Reverse transcription quantitative PCR (RT-qPCR) for lipid metabolism genes in L-LD (8, 14, 17) and H-LD (6, 11, 13) clones at passages 1, 2 and 6 post isolation from bulk E14-ESC culture, normalized to housekeeping genes (*Rpl19, Rsl17*).
(F) RT-qPCR of pluripotency (*Nanog*, *Oct4/Pou5f1*) and early differentiation (*Fgf5*, *T/Brachyury*, *Mixl1*) genes in embryoid bodies (EBs), derived from L-LD (8), H1-LD (4), and H2-LD (11) clones, collected at day 0, 3, 6, and 9, post induction of EB differentiation. Data are normalized to housekeeping genes (*Rpl19, Rsl17*). Data are shown from a representative experiment (n=3).
(G) Percentage of colonies, in L-LD (8), H1-LD (4) and H2-LD (11), formed from cells seeded at low density and grown for 7 days in FBS/LIF (left) and 2i/LIF (right). Colonies were counted and scored as undifferentiated, mixed, and differentiated based on alkaline phosphatase staining. Error bars, mean ± SEM (n=3).
(H) Dot plots showing selected over-represented pathways identified using differentially expressed genes between L-LD and H1-LD (top panel) and L-LD and H2-LD (bottom panel). Each dot represents a specific pathway, where the size of the dot corresponds to the number of differentially expressed genes associated with that pathway, and the color of the dot corresponds to the false discovery rate (FDR) value following Benjamini-Hochberg (BH) correction for multiple testing (FDR < 0.05) (see also Table S1).
(I) Schematic representation of ESC-derived 3D spheroids and lipid storage trafficking prior to (0 hour), and post induction (24 and 48 hours) of differentiation.
(J) Heatmap showing relative expression of pluripotency-associated genes in ESC-derived 3D-spheroids upon differentiation (top) and LD clones (bottom) (see also Table S5).

FIGURE S2

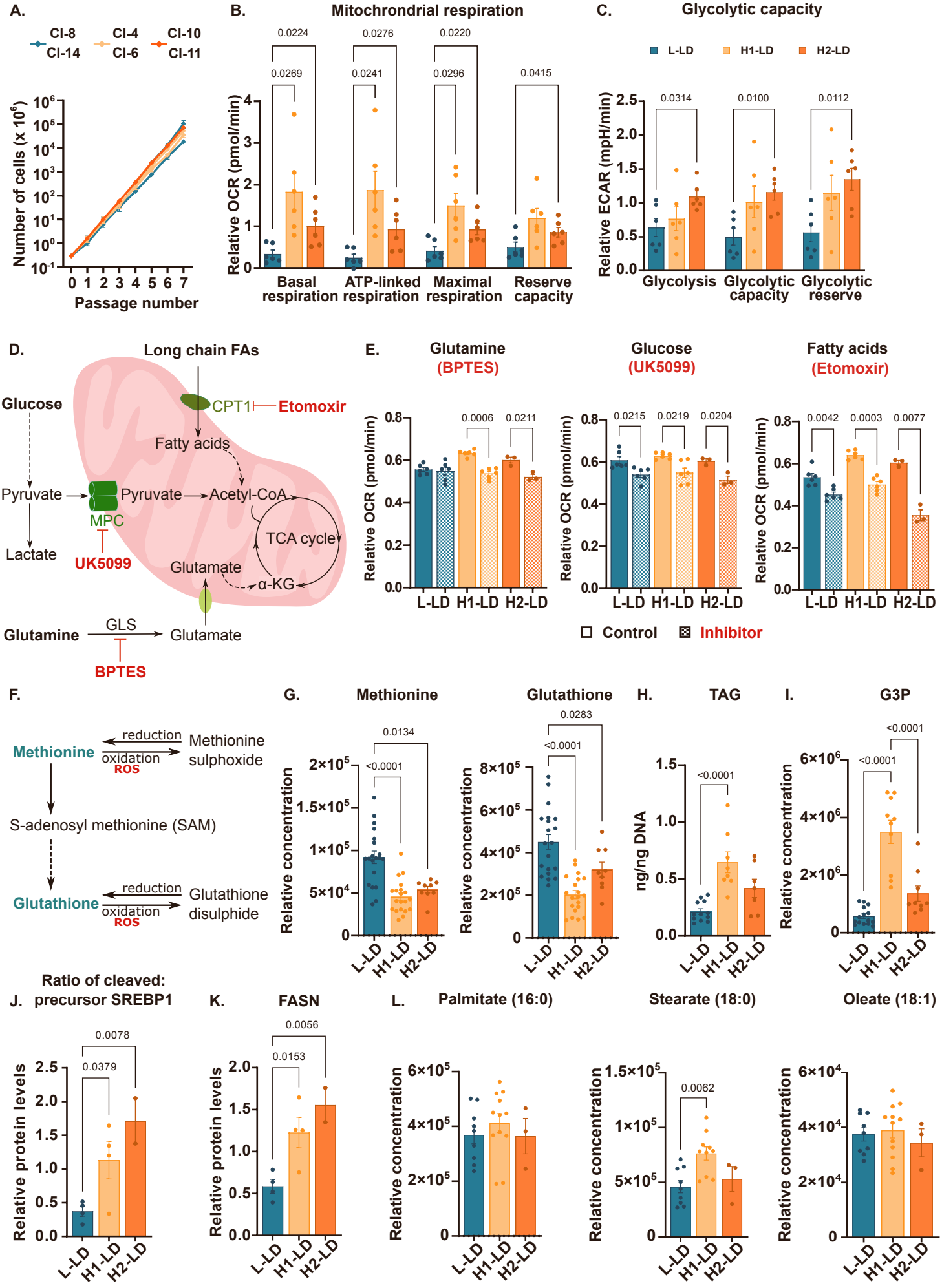
A.
Cl-8
Cl-14
Cl-4
Cl-6
Cl-10
Cl-11
Number of cells (x 10^6)
Passage number
B.
Mitochrondrial respiration
Relative OCR (pmol/min)
0.0224
0.0269
0.0276
0.0241
0.0220
0.0296
0.0415
Basal respiration
ATP-linked respiration
Maximal respiration
Reserve capacity
C.
Glycolytic capacity
L-LD
H1-LD
H2-LD
Relative ECAR (mpH/min)
0.0314
0.0100
0.0112
Glycolysis
Glycolytic capacity
Glycolytic reserve
D.
Long chain FAs
Glucose
CPT1
Etomoxir
Fatty acids
Pyruvate
Pyruvate
Acetyl-CoA
MPC
TCA cycle
Lactate
UK5099
Glutamate
α-KG
Glutamine
GLS
Glutamate
BPTES
E.
Glutamine (BPTES)
Glucose (UK5099)
Fatty acids (Etomoxir)
Relative OCR (pmol/min)
0.0006
0.0211
0.0215
0.0219
0.0204
0.0042
0.0003
0.0077
L-LD H1-LD H2-LD
Control
Inhibitor
F.
Methionine
reduction
oxidation
ROS
Methionine sulphoxide
S-adenosyl methionine (SAM)
Glutathione
reduction
oxidation
ROS
Glutathione disulphide
G.
Methionine
Glutathione
Relative concentration
0.0134
<0.0001
0.0283
<0.0001
H.
TAG
ng/ng DNA
<0.0001
I.
G3P
Relative concentration
<0.0001
<0.0001
J.
Ratio of cleaved: precursor SREBP1
Relative protein levels
0.0078
0.0379
K.
FASN
Relative protein levels
0.0056
0.0153
L.
Palmitate (16:0)
Stearate (18:0)
Oleate (18:1)
Relative concentration
0.0062

Figure S2: Metabolic characteristics of L-LD and H-LD clones along a differentiation trajectory, related to Figure 2 and Figure 3.

(A) Growth curves of indicated LD clones in FBS/LIF conditions over 7 passages (14 days). Error bars, mean ± SEM (n=3).
(B) Assessment of mitochondrial respiration from OCR measurements following the serial addition of ETC-complex inhibitors in LD clones (see also Figure 2A). Data are shown relative to parental E14 ESCs. Error bars, mean ± SEM; ANOVA with Tukey's post-hoc (n=3 per clone).
(C) Assessment of glycolytic capacity from ECAR measurements following addition of indicated drugs (see also Figure 2B). Data are shown relative to parental E14 ESCs. Error bars, mean ± SEM; ANOVA with Tukey's post-hoc (n=3 per clone).
(D) Schematic representation of mitochondrial metabolic pathways with indication of inhibitors (red) used in (E).
(E) ATP-linked respiration to assess substrate utilization in L-LD (8, 17), H1-LD (4, 6) and H2-LD (11) clones treated with glutaminase inhibitor (BPTES, 10 μM), MPC1 inhibitor (UK5099, 20 μM), and CPT1 inhibitor (Etomoxir, 40 μM), respectively. Data are normalized to DMSO-treated control. Error bars, mean ± SEM; paired two-tailed t-test (n=3).
(F) Schematic of methionine and glutathione redox metabolism.
(G) Relative concentration of methionine and glutathione in L-LD (5, 8, 14, 17), H1-LD (1, 4, 6, 13) and H2-LD (10, 11) clones measured by GC-MS. Error bars, mean ± SEM; ANOVA with Tukey's post-hoc (n=4 per clone).
(H) LC-MS quantification of TAG in L-LD (8,14,17), H1-LD (4, 6) and H2-LD (10, 11) (see also Figure 1D).
(I) Relative concentration of glycerol-3-phosphate (G3P) in L-LD (8, 14, 17), H1-LD (4, 6) and H2-LD (10, 11) measured by GC-MS (also shown in Figure 2D) (see also Table S2).
(J,K) Western blot quantification of (J) cleaved to precursor SREBP1 and (K) FASN to a-TUBULIN loading control in L-LD (8, 17), H1-LD (4, 6), and H2-LD (11) clones (see also Figure 3C). Error bars, mean ± SEM; ANOVA with Tukey's post-hoc test (n=2 per clone).
(L) Relative concentration of intracellular methylated fatty acids (palmitate, stearate, oleate) in L-LD (8, 14, 17), H1-LD (1, 4, 6, 13), and H2-LD (11) clones. Error bars, mean ± SEM; ANOVA with Tukey's post-hoc test (n=3 per clone) (see also Table S3).

FIGURE S3

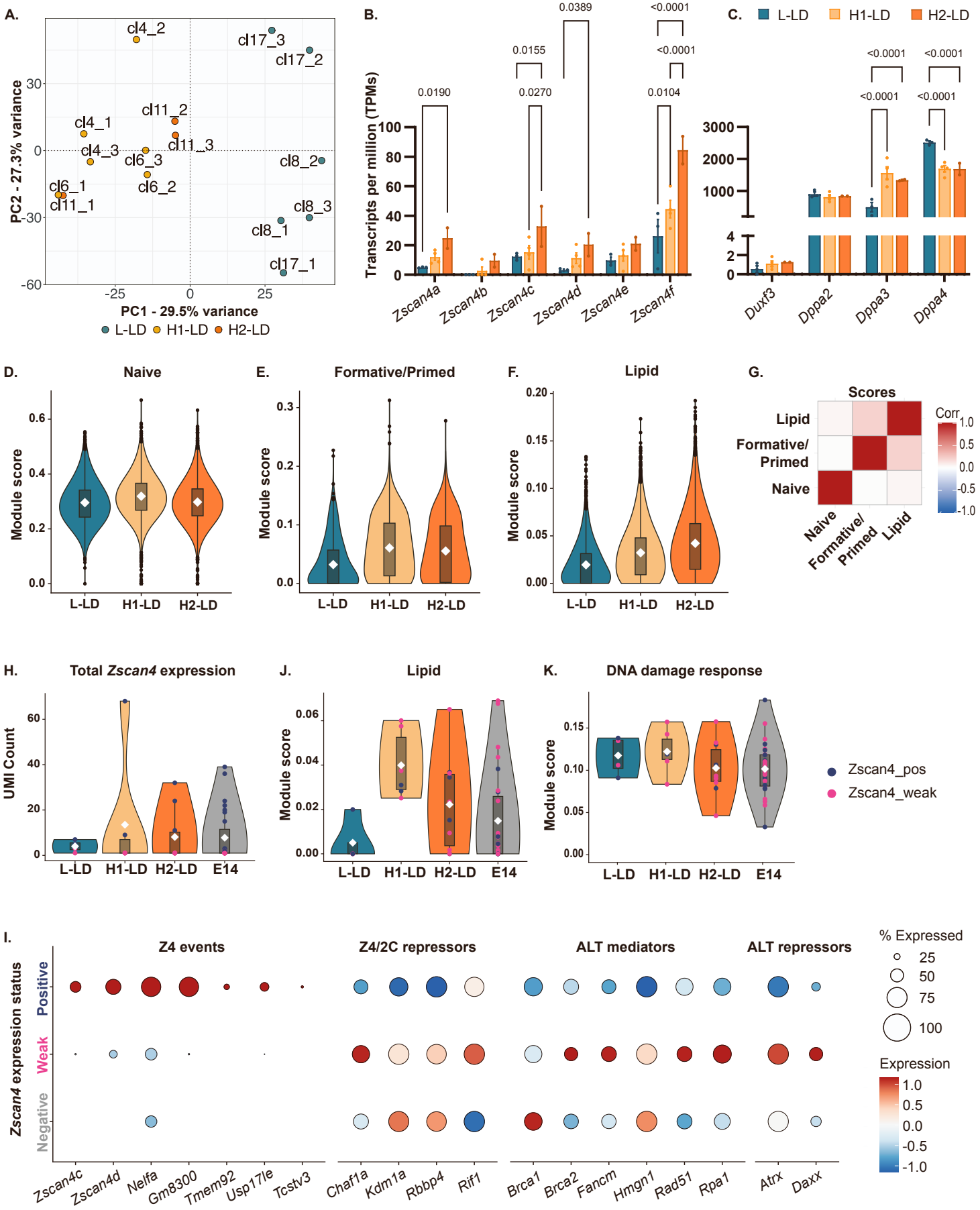
A.
PC2 - 27.3% variance
PC1 - 29.5% variance
L-LD H1-LD H2-LD
B.
Transcripts per million (TPMs)
Zscan4a
Zscan4b
Zscan4c
Zscan4d
Zscan4e
Zscan4f
C.
L-LD H1-LD H2-LD
Duxf3
Dppa2
Dppa3
Dppa4
D.
Naive
Module score
E.
Formative/Primed
F.
Lipid
G.
Scores
Corr
Naive
Formative/ Primed
Lipid
H.
Total Zscan4 expression
UMI Count
J.
K.
DNA damage response
Zscan4_pos
Zscan4_weak
I.
Z4 events
Z4/2C repressors
ALT mediators
ALT repressors
Zscan4 expression status
Positive
Weak
Negative
% Expressed
Expression
Zscan4c
Zscan4d
Nelfa
Gm8300
Tmem92
Usp17le
Tcstv3
Chaf1a
Kdm1a
Rbbp4
Rif1
Brca1
Brca2
Fancm
Hmgn1
Rad51
Rpa1
Atrx
Daxx

Figure S3: Multi-omics analysis reveals differential ZSCAN4 activity in L-LD and H-LD clones, related to Figure 4.

(A) PCA performed on chromatin-enriched proteomics (ChEP) data collected from L-LD (8, 17), H1-LD (4,6) and H2-LD (11) clones (see also Table S4).
(B,C) Gene expression profiling (bulk RNA-seq) of (B) *Zscan4* paralogues and (C) 2 cell-like *Duxf3*, *Dppa2*, *Dppa3* and *Dppa4* genes, in L-LD (8, 14, 17), H1-LD (1, 4, 6, 13) and H2-LD (10,11) clones represented as TPMs. Error bars, mean ± SEM; Fisher's two-way ANOVA.
(D-F) Pseudo-bulk analysis of single-cell RNA-seq data collected from representative L-LD (8), H1-LD (4) and H2-LD (11) clones to confirm distinct (D) naive, (E) formative/primed, and (F) lipid transcriptional signatures computed as scores (see STAR Methods).
(G) Correlation heatmap representing computed transcriptional scores from panels D-F.
(H) Expression of all *Zscan4* paralogues in each clone group and parental E14-ESCs (E14) plotted as UMI counts.
(I) Expression of known genes associated with ZSCAN4 (Z4) events (*Zscan4c, Zscan4d, Nelfa, Eif1ad8*/*Gm8300, Tmem92, Usp17le, Tcstv3*), repressors of Z4 events (*Chaf1a, Kdm1a, Rbbp4, Rif1*), mediators of alternative lengthening telomere (ALT) mechanism (*Brca1, Brca2, Fancm, Hmgn1, Rad51, Rpa1*) and repressors of ALT (*Atrx, Daxx*) in *Zscan4*-negative, weakly expressing, and positive single cells shown as dot plots.
(J) Transcriptional score computed for *Zscan4*-expressing cells in each clone group and parental E14-ESCs for lipid metabolic genes (see STAR Methods).
(K) Transcriptional score computed for *Zscan4*-expressing cells in each clone group and parental E14-ESCs for DNA damage response genes (see STAR Methods).

FIGURE S4

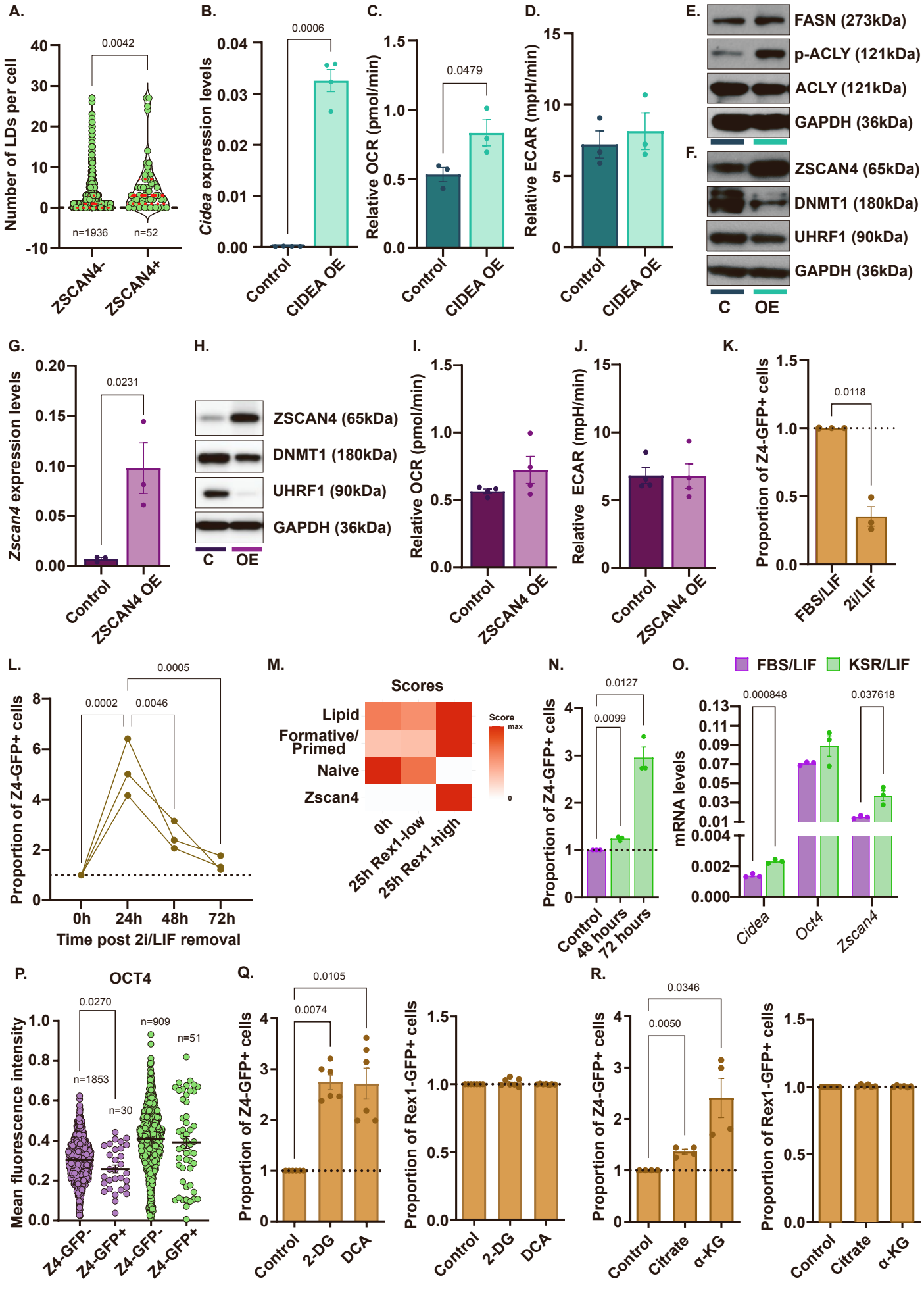
A.
Number of LDs per cell
0.0042
n=1936
n=52
ZSCAN4-
ZSCAN4+
B.
Cidea expression levels
0.0006
Control
CIDEA OE
C.
Relative OCR (pmol/min)
0.0479
Control
CIDEA OE
D.
Relative ECAR (mpH/min)
Control
CIDEA OE
E.
FASN (273kDa)
p-ACLY (121kDa)
ACLY (121kDa)
GAPDH (36kDa)
F.
ZSCAN4 (65kDa)
DNMT1 (180kDa)
UHRF1 (90kDa)
GAPDH (36kDa)
C
OE
G.
Zscan4 expression levels
0.0231
Control
ZSCAN4 OE
H.
ZSCAN4 (65kDa)
DNMT1 (180kDa)
UHRF1 (90kDa)
GAPDH (36kDa)
C
OE
I.
Relative OCR (pmol/min)
Control
ZSCAN4 OE
J.
Relative ECAR (mpH/min)
Control
ZSCAN4 OE
K.
Proportion of Z4-GFP+ cells
0.0118
FBS/LIF
2i/LIF
L.
Proportion of Z4-GFP+ cells
0.0005
0.0002
0.0046
0h
24h
48h
72h
Time post 2i/LIF removal
M.
Scores
Lipid
Formative/ Primed
Naive
Zscan4
Score
max
0
0h
25h Rex1-low
25h Rex1-high
N.
Proportion of Z4-GFP+ cells
0.0127
0.0099
Control
48 hours
72 hours
O.
FBS/LIF
KSR/LIF
mRNA levels
0.000848
0.037618
Cidea
Oct4
Zscan4
P.
OCT4
Mean fluorescence intensity
0.0270
n=1853
n=30
n=909
n=51
Z4-GFP-
Z4-GFP+
Z4-GFP-
Z4-GFP+
Q.
Proportion of Z4-GFP+ cells
0.0105
0.0074
Control
2-DG
DCA
Proportion of Rex1-GFP+ cells
Control
2-DG
DCA
R.
Proportion of Z4-GFP+ cells
0.0346
0.0050
Control
Citrate
α-KG
Proportion of Rex1-GFP+ cells
Control
Citrate
α-KG

Figure S4: *Zscan4* induction is downstream of lipid-droplet associated metabolic shifts in ESCs, related to Figure 5.

(A) Number of LDs per cell in ZSCAN4-negative (ZSCAN4-) and ZSCAN4-positive (ZSCAN4+) ESCs co-stained for BODIPY 493/503, ZSCAN4, and DAPI. Red lines indicate median ± quartiles; unpaired two-tailed t-test with Welch's correction (n=1988 cells across four independent experiments).
(B) RT-qPCR of *Cidea* transcript, normalized to housekeeping genes (*Rpl19, Rps17*), in control and CIDEA OE ESCs. Error bars, mean ± SEM; paired two-tailed t-test with Welch's correction (n=4).
(C) ATP-linked OCR and (D) glycolysis-associated ECAR, measured by Seahorse assays in control and CIDEA OE ESCs. Error bars, mean ± SEM; paired two-tailed t-test with Welch's correction (n=3).
(E,F) Representative western blots of (E) FASN, p-ACLY (Ser455) and total ACLY, with GAPDH loading control, and (F) ZSCAN4, DNMT1, UHRF1, with GAPDH loading control in control (labelled C) and CIDEA OE (labelled OE) ESCs (n=3).
(G) RT-qPCR of total *Zscan4* transcripts, normalized to housekeeping genes (*Rpl19, Rps17*), in control and ZSCAN4 OE ESCs. Error bars, mean ± SEM; paired two-tailed t-test with Welch's correction (n=3).
(H) Representative western blots of ZSCAN4, DNMT1, UHRF1, with GAPDH loading control in control (labelled C) and ZSCAN4 OE (labelled OE) ESCs (n=3).
(I) ATP-linked OCR and (J) glycolysis-associated ECAR, measured by Seahorse assays in control and ZSCAN4 OE ESCs. Error bars, mean ± SEM; paired two-tailed t-test with Welch's correction (n=4).
(K) Proportion of ZSCAN4::GFP positive (Z4-GFP+) ESCs in FBS/LIF or 2i/LIF culture conditions. Error bars, mean ± SEM; paired two-tailed t-test with Welch's correction (n=3).
(L) Proportion of Z4-GFP+ ESCs measured at 0, 24, 48, and 72 hours post removal of 2i/LIF conditions and transient conversion into EpiLCs, relative to 2i/L cultures at 0 hour. ANOVA with Tukey's post-hoc (n=3).
(M) Correlation heatmap depicting lipid metabolism, formative/primed pluripotency, naive pluripotency, and Zscan4 scores in Rex1-GFP reporter ESCs at 0 hour, and at 25 hours post removal of 2i/LIF, sorted into Rex1-high and Rex1-low populations. Rex1-GFP downregulation delineates the exit of naive pluripotency (see also Table S5, STAR Methods).
(N) Proportion of Z4-GFP+ ESCs in FBS/LIF (control) or KSR/LIF conditions for 48 hours and 72 hours. Error bars, mean ± SEM; paired two-tailed t-test (to control) with Welch's correction (n=3).
(O) RT-qPCR of *Cidea, Oct4,* and total *Zscan4*, normalized to housekeeping genes (*Rpl19, Rps17*) in ESCs cultured in FBS/LIF or KSR/LIF conditions for 48 hours. Error bars, mean ± SEM; paired two-tailed t-test with Welch's correction (n=3).
(P) Mean fluorescence intensity of OCT4 in Z4-GFP+ or Z4-GFP- nuclei, grown in FBS/LIF (purple) or KSR/LIF (green) culture conditions for 48 hours. Error bars, mean ± SEM; unpaired t-test with Welch's correction (n=3 independent experiments).
(Q) Proportion of Z4-GFP+ ESCs (left panel) or Rex1-GFP+ ESCs (right panel) upon 2-DG (10 mM) or DCA (10 mM) treatment for 48 hours in routine FBS/LIF medium. Error bars, mean ± SEM; paired two-tailed t-test (to control) with Welch's correction (n=6).
(R) Proportion of Z4-GFP+ ESCs (left panel) or Rex1-GFP+ ESCs (right panel) upon citrate (4 mM) or α-KG (4 mM) treatment for 48 hours in routine FBS/LIF. Error bars, mean ± SEM; paired two-tailed t-test (to control) with Welch's correction (n=4).

FIGURE S5

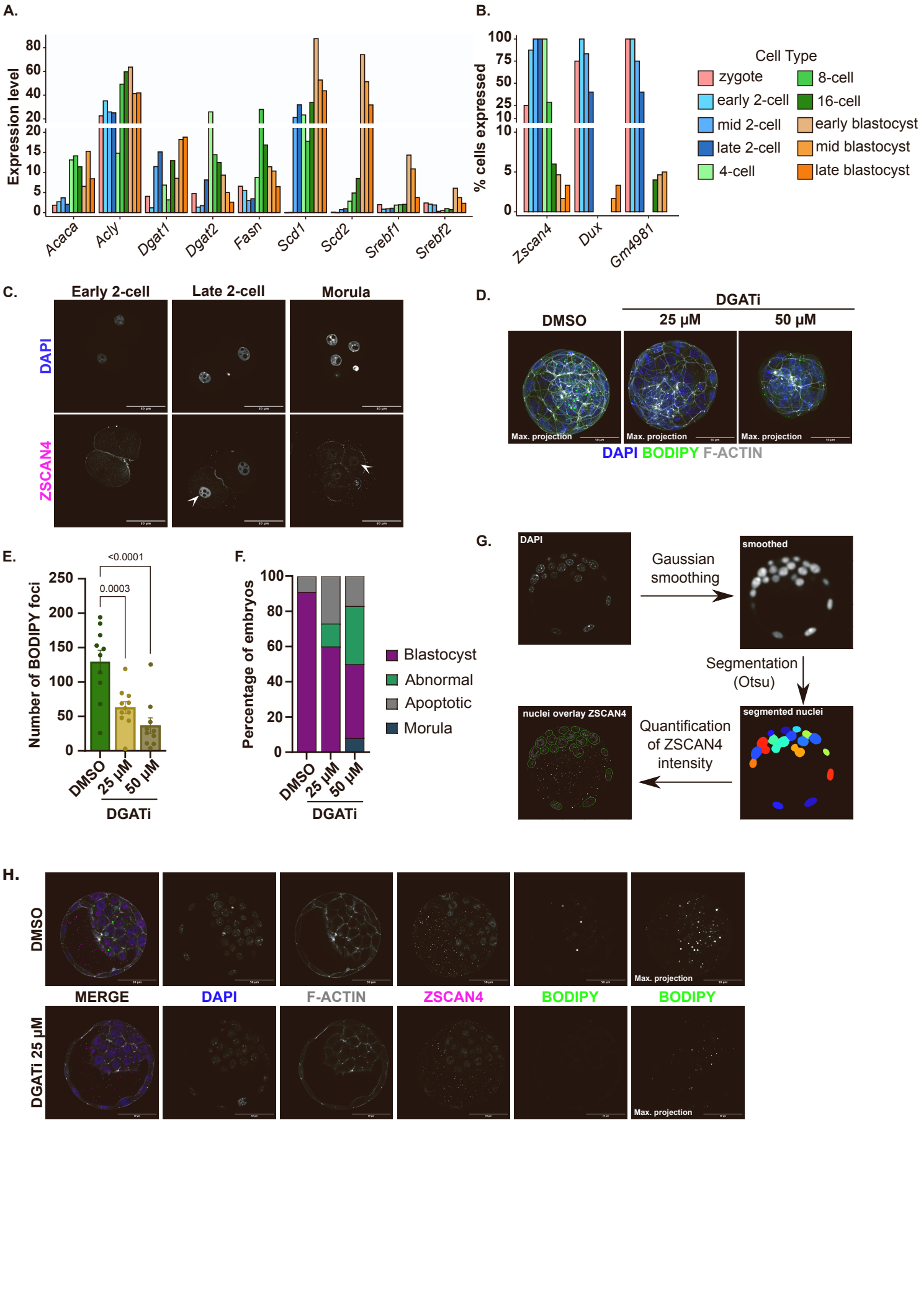
A.
Expression level
Acaca
Acly
Dgat1
Dgat2
Fasn
Scd1
Scd2
Srebf1
Srebf2
B.
% cells expressed
Zscan4
Dux
Gm4981
Cell Type
zygote
early 2-cell
mid 2-cell
late 2-cell
4-cell
8-cell
16-cell
early blastocyst
mid blastocyst
late blastocyst
C.
Early 2-cell
Late 2-cell
Morula
DAPI
ZSCAN4
D.
DGATi
DMSO
25 µM
50 µM
Max. projection
DAPI BODIPY F-ACTIN
E.
Number of BODIPY foci
<0.0001
0.0003
DMSO
25 µM
50 µM
DGATi
F.
Percentage of embryos
Blastocyst
Abnormal
Apoptotic
Morula
G.
DAPI
Gaussian smoothing
smoothed
Segmentation (Otsu)
segmented nuclei
Quantification of ZSCAN4 intensity
nuclei overlay ZSCAN4
H.
DMSO
DGATi 25 µM
MERGE
DAPI
F-ACTIN
ZSCAN4
BODIPY
BODIPY
Max. projection

Figure S5: Interfering with lipid storage during the morula-to-blastocyst transition reduces ZSCAN4 expression, related to Figure 5.

(A) Expression level of lipid metabolism genes in single-cell RNA-seq data from mouse embryos at specified stages of development (see also Table S5).
(B) Percentage of cells expressing *Zscan4, Dux,* and *Gm4981/Duxf4* in mouse embryos at specified stages of development.
(C) Representative images of early 2-cell, late 2-cell, and pre-compacted morula embryos stained with DAPI and ZSCAN4. Scale bars, 50 μm.
(D) Representative maximum projection images of morula embryos (E2.5) cultured up to the early blastocyst stage (E3.5) with DMSO or inhibitors against DGAT1 and DGAT2 (DGATi; 25 μM and 50 μM) stained with BODIPY 493/503 (green), F-ACTIN (grey) and DAPI (blue). Scale bars, 50 μm.
(E) Number of BODIPY foci detected per embryo. Error bars, mean ± SEM; one-way ANOVA with post-hoc Dunnett's test (n=10-11) (see also Figure 5N).
(F) Scoring of the morphology of morula embryos cultured with DMSO or DGATi (25 μM and 50 μM) up to the early blastocyst stage.
(G) Schematic of image analysis pipeline using CellProfiler. DAPI-positive nuclei were segmented in Gaussian-smoothed single z-sections. ZSCAN4 signal intensity was quantified within segmented nuclei (see also Figure 5O).
(H) Representative images of blastocysts with DMSO or DGATi (25 μM) stained with ZSCAN4 (pink), BODIPY 493/503 (green), F-ACTIN (grey) and DAPI (blue). Scale bars, 50 μm.

FIGURE S6

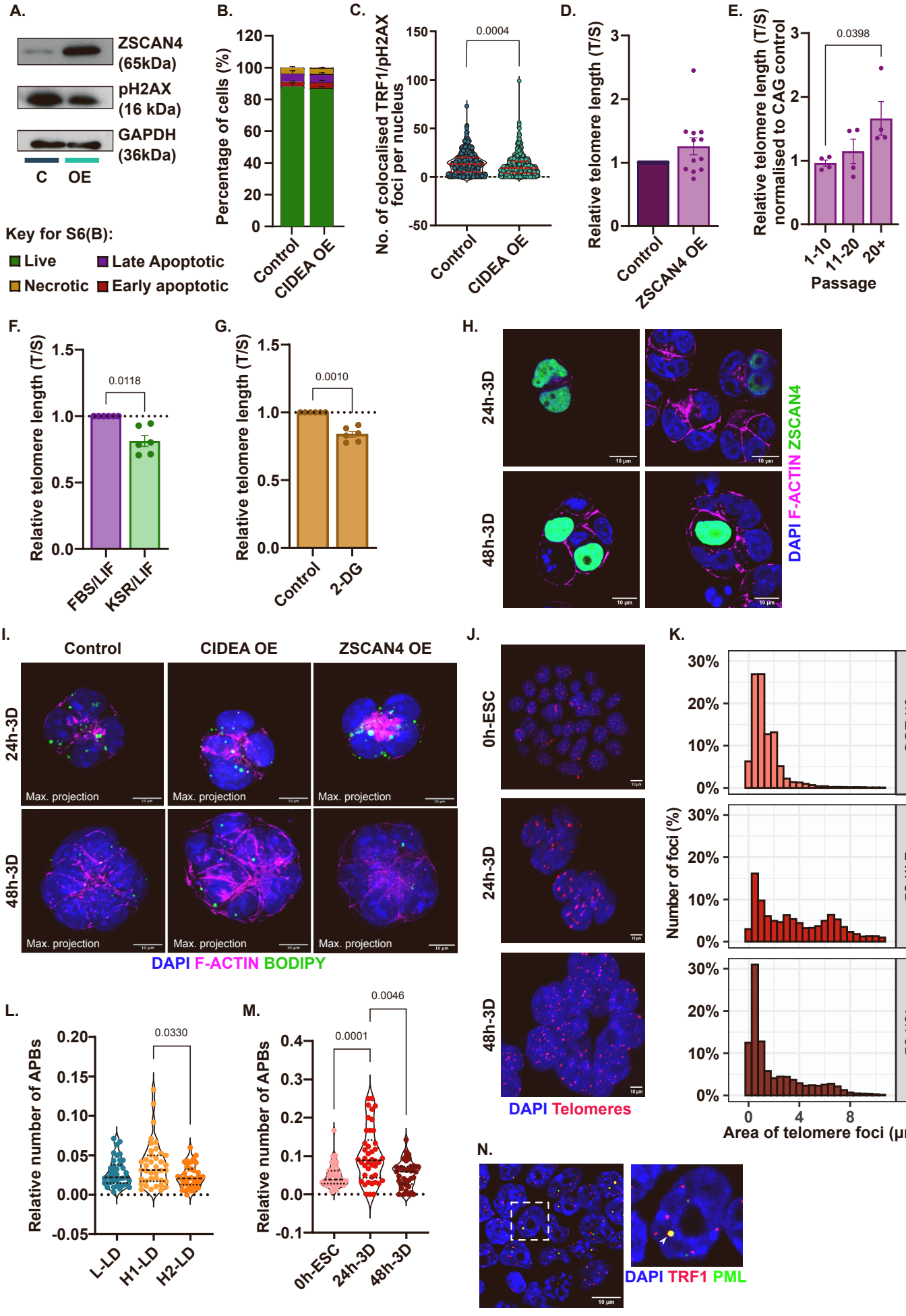
A.
ZSCAN4 (65kDa)
pH2AX (16 kDa)
GAPDH (36kDa)
C
OE
B.
Percentage of cells (%)
Control
CIDEA OE
Key for S6(B):
Live
Late Apoptotic
Necrotic
Early apoptotic
C.
No. of colocalised TRF1/pH2AX foci per nucleus
0.0004
Control
CIDEA OE
D.
Relative telomere length (T/S)
Control
ZSCAN4 OE
E.
Relative telomere length (T/S) normalised to CAG control
0.0398
1-10
11-20
20+
Passage
F.
Relative telomere length (T/S)
0.0118
FBS/LIF
KSR/LIF
G.
Relative telomere length (T/S)
0.0010
Control
2-DG
H.
24h-3D
48h-3D
DAPI F-ACTIN ZSCAN4
I.
Control
CIDEA OE
ZSCAN4 OE
24h-3D
48h-3D
Max. projection
DAPI F-ACTIN BODIPY
J.
0h-ESC
24h-3D
48h-3D
DAPI Telomeres
K.
Number of foci (%)
0h-ESC
24h-3D
48h-3D
Area of telomere foci (μm²)
L.
Relative number of APBs
0.0330
L-LD
H1-LD
H2-LD
M.
Relative number of APBs
0.0046
0.0001
0h-ESC
24h-3D
48h-3D
N.
DAPI TRF1 PML

Figure S6: Telomere homeostasis in ESC-based models prior to and upon differentiation, related to Figure 6.

(A) Representative western blots of ZSCAN4 and pH2AX (Ser139) with GAPDH loading control in control (C) and CIDEA OE (OE) ESCs (n=3).
(B) Measurement of apoptosis indices in control and CIDEA OE ESCs using flow cytometry-based measurements of Annexin-V and propidium iodine (n=3).
(C) Number of co-localized TRF1 and pH2AX-Ser139 foci per nucleus in control and CIDEA OE ESCs. Red lines indicate median ± quartiles; unpaired t-test with Welch's correction (n=3).
(D) Relative telomere lengths as measured by telomere qPCR, shown as a ratio of telomere to single-copy gene (T/S) in control and ZSCAN4OE ESCs. Error bars, mean ± SEM; paired two-tailed t-test with Welch's correction (n=12).
(E) Relative telomere lengths as measured by telomere quantitative PCR (qPCR), shown as a ratio of telomere to single-copy gene (T/S) in ZSCAN4OE ESCs, segregated by passage number (data also represented in (D)). Error bars, mean ± SEM; one-way ANOVA with Fisher's post-hoc (n=4).
(F,G) Relative telomere lengths as measured by telomere qPCR in ESCs grown in (F) FBS/LIF (control) or KSR/LIF conditions for 48 hours, and in (G) FBS/LIF (control) or 2-DG (10 mM in FBS/LIF) for 48 hours. Error bars, mean ± SEM; paired two-tailed t-test with Welch's correction (n=6).
(H) Representative images of R1-ESC-derived 3D spheroids at different timepoints of differentiation (24 and 48 hours), stained for ZSCAN4 (green), F-ACTIN (Phalloidin, pink) and nuclei (DAPI, blue). Scale bars, 10 μm.
(I) Representative images of control, CIDEA OE, and ZSCAN4 OE ESC-derived 3D spheroids at different timepoints of differentiation (24 and 48 hours), stained for LDs (BODIPY, green), F-ACTIN (Phalloidin, pink) and nuclei (DAPI, blue). Scale bars, 10 μm.
(J) Representative images of Telo-FISH using the TelC-Cy3 probe (red) and DAPI (blue) in undifferentiated ESCs (0 hour) and ESC-derived 3D spheroids post induction of differentiation (24 and 48 hours). Scale bars, 10 μm.
(K) Frequency distributions of the area (μm^2) of telomeric foci at each timepoint (n=90 colonies/spheroids across 3 independent experiments).
(L,M) Quantification of number of ALT-associated PML bodies (APBs) per nucleus, normalized to total PML in (L) L-LD (8), H1-LD (4) and H2-LD (11) clones, and in (M) ESC-derived 3D spheroids at different timepoints of differentiation. Lines indicate median ± quartiles; ANOVA with Dunnett's post-hoc test (n>40 colonies/spheroids across 3-4 independent experiments).
(N) Representative image of APBs as visualized by co-localization of PML (green) to telomeres (TRF1; red) within DAPI-stained nuclei (blue). Scale bar, 10 μm. Inset shows arrow to highlight co-localization between TRF1 and PML.

Table S5: List of accession numbers for transcriptomic datasets, related to Figure 1K, Figure 4I-N, Figure 6G, Figure S1J, Figure S3D-I, Figure S4M, Figure S5A,B.

Figure	Label	Series accession	Sample accession	Cell type	Backgr-ound	Culture conditio-ns	PMID	Notes
Figure 1K	ESC-1	GSE56138	GSM1355138	ESC	R1	2i/LIF	24905168	
	ESC-1	GSE56138	GSM1355139	ESC	R1	2i/LIF	24905168	
	EpiLC-1	GSE56138	GSM1355140	EpiLC	R1	N2B27/ KSR/FGF	24905168	
	EpiLC-1	GSE56138	GSM1355141	EpiLC	R1	N2B27/ KSR/FGF/Activin A	24905168	
	ESC-2	GSE56138	GSM1355142	ESC	E14	2i/LIF	24905168	
	EpiLC-2	GSE56138	GSM1355143	EpiLC	E14	N2B27/ KSR/ FGF	24905168	
	ESC	GSE57409	GSM1382094	ESC	ESF122	KSR/LIF	24905169	
	ESC	GSE57409	GSM1382095	ESC	ESF122	KSR/LIF	24905169	
	ESC	GSE57409	GSM1382096	ESC	ESF175 /1	KSR/LIF	24905169	
	ESC	GSE57409	GSM1382097	ESC	ESF175 /1	KSR/LIF	24905169	
	EpiSC	GSE57409	GSM1382098	EpiSC	EpiSC5	MEF/ KSR/ FGF	24905169	
	EpiSC	GSE57409	GSM1382099	EpiSC	EpiSC7	MEF/ KSR/ FGF	24905169	
	EpiSC	GSE57409	GSM1382100	EpiSC	EpiSC7	MEF/ KSR/ FGF	24905169	
	EpiSC	GSE57409	GSM1382101	EpiSC	EpiSC9	MEF/KSR/FGF	24905169	
	ESC-3	GSE165563	GSM5041408	ESC	R1	FBS/LIF	35790717	
	3D_24h-3	GSE165563	GSM5041409	3D differentiated ESC	R1	Matrigel/ FBS	35790717	
	3D_48h-3	GSE165563	GSM5041411	3D differentiated ESC	R1	Matrigel/ FBS	35790717	
	ESC-3	GSE165563	GSM5041412	ESC	R1	FBS/LIF	35790717	
	3D_24h-3	GSE165563	GSM5041413	3D differentiated ESC	R1	Matrigel/ FBS	35790717	
	3D_48h-3	GSE165563	GSM5041415	3D differentiated ESC	R1	Matrigel/ FBS	35790717	

	L-LD; Clone8	GSE270063	GSM8333908	ESC	E14	FBS/LIF	This paper	
	L-LD; Clone14	GSE270063	GSM8333903	ESC	E14	FBS/LIF	This paper	
	L-LD; Clone17	GSE270063	GSM8333904	ESC	E14	FBS/LIF	This paper	
	H1-LD; Clone1	GSE270063	GSM8333905	ESC	E14	FBS/LIF	This paper	
	H1-LD; Clone4	GSE270063	GSM8333906	ESC	E14	FBS/LIF	This paper	
	H1-LD; Clone6	GSE270063	GSM8333907	ESC	E14	FBS/LIF	This paper	
	H1-LD; Clone13	GSE270063	GSM8333902	ESC	E14	FBS/LIF	This paper	
	H2-LD; Clone10	GSE270063	GSM8333900	ESC	E14	FBS/LIF	This paper	
	H2-LD; Clone11	GSE270063	GSM8333901	ESC	E14	FBS/LIF	This paper	
Figure 4I-N, S3D-I	-	GSE253432	-	ESC	E14	-	This paper	
Figure S4M	-	E-MTAB-5305	-	-	-	-	28174249	
Figure S5A,B	-	GSE45719	-	-	-	-	24408435	
Figure S1J, 6G	-	GSE165563	-	-	-	-	35790717	Also in Figure 1K

Table S6: List of antibodies and dilutions used, related to STAR Methods.

Target	Catalogue Number	Clone	Company	Host species	WB	IF
ACLY	4332	-	Cell Signaling Technologies	Rabbit	1:1000	-
DNMT1	ab87654	-	Abcam	Rabbit	1:10000	-
FASN	3180	C20G5	Cell Signaling Technologies	Rabbit	1:1000	-
GAPDH	5174S	-	Cell Signaling Technologies	Rabbit	1:5000	-
GFP	GFP-1020	-	Aves Lab	Chicken	-	1:200
OCT3/4	sc-5279	C-10	Santa Cruz	Mouse	-	1:100
p-ACLY(ser455)	4331	-	Cell Signaling Technologies	Rabbit	1:1000	-
p-H2AX(ser139)	9718	20E3	Cell Signaling Technologies	Rabbit	1:5000	1:200
PML	05-718	36.1-104	Millipore	Mouse	-	1:200
SREBP-1	sc13551	2A4	Santa Cruz	Mouse	1:200	-
TRF1	ab192629	-	Abcam	Rat	-	1:200
UHRF1	sc373750	M-8	Santa Cruz	Mouse	1:1000	-
VINCULIN	V9264	-	Sigma-Aldrich	Mouse	1:5000	-
ZSCAN4	AB4340	-	Millipore	Rabbit	1:1000	1:100
AF488 Anti-Chicken	A11039		Invitrogen		-	1:200
AF488 Anti-Rabbit	A21206		Invitrogen		-	1:200
AF488 Anti-Rat	A11006		Invitrogen		-	1:200
AF568 Anti-Mouse	A21422		Invitrogen		-	1:200
AF568 Anti-Rabbit	A11036		Invitrogen		-	1:200
AF633 Anti-Rabbit	A21071		Invitrogen		-	1:200
AF647 Anti-Rat	A21247		Invitrogen		-	1:200
Anti-Mouse IgG HRP-linked	7076		Cell Signaling Technologies		1:5000	-
Anti-Rabbit IgG HRP-linked	7074		Cell Signaling Technologies		1:5000	-

Table S7: List of primers used for RT-qPCR and telomeric analyses, related to STAR Methods.

	Target	**Forward (5'-3')**	**Reverse (5'-3')**
For RT-qPCR	*Cidea*	AAGCTTCAAGGCCGTGTTA	CTGTAGCTGTGCCCTGGTTA
	Dgat2	AGTGGCAATGCTATCATCATCGT	TCTTCTGGACCCATCGGCCCCAGGA
	Esrrb	GCACCTGGGCTCTAGTTGC	TACAGTCCTCGTAGCTCTTGC
	Fabp3	CTGGAAGCTAGTGGACAGCAA	TCCCAGCTGAAAGTTGATCTCT
	Fasn	TGCACCTCACAGGCATCAAT	GTCCCACTTGATGTGAGGGG
	Fgf5	TGTGTCTCAGGGGATTGTAGG	AGCTGTTTTCTTGGAATCTCTC
	Mixl1	GACAGACCATGTACCCAGAC	GCTTCAAACACCTAGCTTCAG
	Nanog	CTTACAAGGGTCTGCTACTGA	TCTGCTTCCTGGCAAGGACC
	Oct4/Pou5f1	CGTGGAGACTTTGCAGCCTG	GCTTGGAAACTGTTCTAGCTCCT
	Otx2	TATCTAAAGCAACCGCCTTACG	AAGTCCATACCCGAAGTGGTC
	Rpl19/L19	TGATCTGCTGACGGAGTTG	GGAAAAGAAGGTCTGGTTGGA
	Rps17/S17	ATGACTTCCACACCAACAAGC	GCCAACTGTAGGCTGAGTGAC
	Scd1	TCATGGTCCTGCTGCACTTG	GAGCGCTGGTCATGTAGTAGA
	Srebp1c	ATGCCATGGGCAAGTACACA	ATAGCATCTCCTGCGCACTC
	T/Brachyury	CCGGTGCTGAAGGTAAATGT	CCTCCATTGAGCTTGTTGGT
	Zscan4	AAATGCCTTATGTCTGTTCCCTATG	TGTGGTAATTCCTCAGGTGACGAT
	Target	**Forward (5'-3')**	**Reverse (5'-3')**
For Telo/ALT PCR	mTel	CGGTTTGTTTGGGTTTGGGTTTGGGTTTGGGTTTGGGTT	GGCTTGCCTTACCCTTACCCTTACCCTTACCCTTACCCTT
	36B4/*Rplp0*	ACTGGTCTAGGACCCGAGAAG	TCAATGGTGCCTCTGGAGATT